UNIVERSITÀ
DEGLI STUDI
DI PADOVA

Neuronal Population Encoding of Sensory Information in the Rat Barrel Cortex: Local Field Potential Recording and Characterization by an Innovative High-Resolution Brain-Chip Interface

A thesis submitted for the degree of

Doctor of Philosophy in Bioengineering

By:

Claudia Cecchetto

Department of Information Engineering

University of Padova

Supervisor:

Prof. Stefano Vassanelli

Department of Biomedical Sciences

University of Padova

January 2016 (XXVIII Cycle)

Acknowledgments

First of all, I want to thank my family, who always supports me and believes in me, regardless of what I do.

Thanks to Prof. Stefano Vassanelli, my supervisor, who continuously encourages me to improve myself and to trust in my abilities.

Thanks to all my colleagues (current and past) at the NeuroChip Laboratory for all the useful discussions, the advices (for work and not, as Emanuele knows), the help during the experiments (specially Roberto for all the histology procedures) and for making all my long days in the lab more funny. A special thank goes to Mufti, who help me a lot in many occasions, included the writing of this thesis.

Thanks to all my closest friends, who always cheer me up and are there for me when I need.

Abstract

Neuronal networks are at the base of information processing in the brain. They are series of interconnected neurons whose activation defines a recognizable linear pathway. The main goal of studying neural ensembles is to characterize the relationship between the stimulus and the individual or general neuronal responses and the relation amongst the electrical activities of neurons within the network, also understanding how topology and connectivity relates to their function. Many techniques have been developed to study these complex systems: single-cell approaches aim to investigate single neurons and their connections with a limited number of other nerve cells; on the opposite side, low-resolution large-scale approaches, such as functional MRI (Magnetic Resonance Imaging) or electroencephalography (EEG), record signal changes in the brain that are generated by large populations of cells. More recently, multisite recording techniques have been developed to overcome the limitations of previous approaches, allowing to record simultaneously from huge neuronal ensembles with high spatial resolution and in different brain regions, i.e. by using implantable semiconductor chips.

Local Field Potentials (LFPs), the part of electrophysiological signals that has frequencies below $\sim$500 Hz, capture key integrative synaptic processes that cannot be measured by analyzing the spiking activity of few neurons alone. Several studies have used LFPs to investigate cortical network mechanisms involved in sensory processing, motor planning and higher cognitive processes, like memory and perception. LFPs are also promising signals for steering neuroprosthetic devices and for monitoring neural activity even in human beings, since they are more easily and stably recorded in chronic settings than neuronal spikes.

In this work, LFP profiles recorded in the rat barrel cortex through high-resolution CMOS-based needle chips are presented and compared to those obtained by means of conventional Ag/AgCl electrodes inserted into glass micropipettes, which are widely used tools in electrophysiology.

The rat barrel cortex is a well-known example of topographic mapping where each of the whiskers on the snout of the animal is mapped onto a specific cortical area, called a barrel. The barrel cortex contains the somatosensory representation of the whiskers and forms an early stage of cortical processing for tactile information, along with the trigeminal ganglion and the thalamus. It is an area of great importance for understanding how the cerebral cortex works, since the cortical columns that form the basic building blocks of the neocortex can be actually seen within the barrel. Moreover, the barrel cortex has served as a test-bed system for several new methodologies, partly because of its unique and instantly identifiable form, and partly because the species that have barrels, i.e. rodents, are the most commonly used laboratory mammal. The barrel cortex, the whiskers that activate it and the intervening neural pathways have been increasingly the subject of focus by a growing number of research groups for quite some time. Nowadays, studies (such this one) are directed not only at understanding the barrel cortex itself but also at investigating issues in related fields using the barrel cortex as a base model.

In this study, LFP responses were evoked in the target barrel by repeatedly deflecting the corresponding whisker in a controlled fashion, by means of a specifically designed closed-loop piezoelectric bending system triggered by a custom LabView acquisition software. Evoked LFPs generated in the barrel cortex by many consecutive whiskers' stimulations show large variability in shapes and timings. Moreover, anesthetics can deeply affect the profile of evoked responses. This work presents preliminary results on the variability and the effect of commonly used anesthetics on these signals, by comparing the distributions of evoked responses recorded from rats anesthetized with

tiletamine-xylazine, which mainly blocks the excitatory NMDA receptors, and urethane, which conversely affects both the excitatory and inhibitory system, in a complex and balanced way yet preserving the synaptic plasticity. Representative signal shape characteristics (e.g., latencies and amplitude of events) extracted from evoked responses acquired from different cortical layers are analyzed and discussed. Statistical distributions of these parameters are estimated for all the different depths, in order to assess the variability of LFPs generated by individual mechanical stimulations of single whiskers along the entire cortical column. Preliminary results showed a great variability in cortical responses, which varied both in latency and amplitude across layers. We found significant difference in the latency of the first principal peak of the responses: under tiletamine-xylazine anesthetic, the responses or events of the evoked LFPs occurred later than the ones recorded while urethane was administered. Furthermore, the distributions of this parameter in all cortical layers were narrower in case of urethane. This behavior should be attributed to the different effects of these two anesthetics on specific synaptic receptors and thus on the encoding and processing of the sensory input information along the cortical pathway.

The role of the ongoing basal activity on the modulation of the evoked response was also investigated. To this aim, spontaneous activity was recorded in different cortical layers of the rat barrel cortex under the two types of anesthesia and analyzed in the statistical context of neuronal avalanches. A neuronal avalanche is a cascade of bursts of activity in neural networks, whose size distribution can be approximated by a power law. The event size distribution of neuronal avalanches in cortical networks has been reported to follow a power law of the type $P(s) \propto s^{-\alpha}$, with exponent α close to 1.5, which represent a reflection of long-range spatial correlations in spontaneous neuronal activity. Since negative LFP peaks (nLFPs) originates from the sum of synchronized Action Potentials (AP) from neurons within the vicinity of the recording electrode, we wondered if it were possible to model

single nLFPs recorded in the basal activity traces by means of only one electrode as the result of local neuronal avalanches, and thus we analyzed the size (i.e. the amplitude in μV) distribution of these peaks so as to identify a suitable power-law distribution that could describe also these single-electrode records.

Finally, the results of the first ever measurements of evoked LFPs within an entire column of the barrel cortex obtained by means of the latest generation of CMOS-based implantable needles, having 256 recording sites arranged into two different array topologies (i.e. 16 $\times$ 16 or 4 $\times$ 64, pitches in the x- and y-direction of 15 μm and 33 μm respectively), are presented and discussed. A propagation dynamics of the LFP can be already recognized in these first cortical profiles.

In the next future, the use of these semiconductor devices will help, among other things, to understand how degenerating syndromes like Parkinson or Alzheimer evolve, by coupling detected behaviors and symptoms of the disease to neuronal features. Implantable chips could then be used as 'electroceuticals', a newly coined term that describes one of the most promising branch of bioelectronic medicine: they could help in reverting the course of neurodegenerative diseases, by constituting the basis of neural prostheses that physically supports or even functionally trains impaired neuronal ensembles.

High-resolution extraction and identification of neural signals will also help to develop complex brain-machine interfaces, which can allow intelligent prostheses to be finely controlled by their wearers and to provide sophisticated feedbacks to those who have lost part of their body or brain functions.

Sommario

Le reti neuronali sono alla base della codifica dell'informazione cerebrale. L'obiettivo principale dello studio delle popolazioni neuronali è quello di caratterizzare la relazione tra uno stimolo e la risposta individuale o globale dei neuroni e di studiare il rapporto tra le varie attività elettriche dei neuroni appartenenti ad una particolare rete, comprendendo anche come la topologia e la connettività della rete neuronale influiscano sulla loro funzionalità. Fino ad oggi, molte tecniche sono state sviluppate per studiare questi sistemi complessi: studi a singola cellula mirano a studiare singoli neuroni e le loro connessioni con un numero limitato di altre cellule; sul lato opposto, approcci su larga scala e a bassa risoluzione, come la risonanza magnetica funzionale o l'elettroencefalogramma, registrano segnali elettrofisiologici generati nel cervello da vaste popolazioni di cellule. Più recentemente, sono state sviluppate tecniche di registrazione multisito che mirano ad abbattere le limitazioni dei precedenti approcci, rendendo possibile la misurazione ad alta risoluzione di segnali generati da grandi ensamble neuronali e da diverse regioni del cervello simultaneamente, ad esempio mediante l'uso di chip impiantabili a semiconduttore.

I potenziali di campo locali (LFP) catturano processi sinaptici chiave che non possono essere estratti dall'attività di spiking di qualche neurone isolato. Numerosi studi hanno utilizzato gli LFP per studiare i meccanismi corticali coinvolti nei processi sensoriali, motori e cognitivi, come la memoria e la percezione. Gli LFP rappresentano anche dei segnali interessanti nell'ambito delle applicazioni neuroprotesiche e per monitorare l'attività cerebrale negli esseri umani, dal momento che possono essere registrati più stabilmente e facilmente in impianti cronici rispetto agli spike neuronali.

In questo studio, sono riportati dei profili LFP registrati dalla barrel cortex di ratto tramite chip ad ago ad alta risoluzione basati su tecnologia CMOS e confrontati con quelli ottenuti tramite elettrodi convenzionali in Ag/AgCl inseriti in micropipette di vetro, strumenti comunemente usati in elettrofisiologia.

La barrel cortex di ratto è un esempio ben noto di mapping topografico, nel quale ogni baffo sul muso dell'animale è mappato in una specifica area corticale, chiamata barrel. La barrel cortex contiene la rappresentazione sensoriale dei baffi dell'animale e rappresenta uno dei primi stadi di elaborazione dell'informazione tattile, insieme al ganglio del trigemino e al talamo. Essa è un'area di primaria importanza per lo studio del funzionamento della corteccia cerebrale, visto che le colonne corticali che formano i blocchi di base della neocorteccia possono essere visualizzati facilmente all'interno della barrel cortex. La barrel cortex inoltre è utilizzata come sistema di test in numerose metodologie innovative, grazie alla sua struttura unica ed istantaneamente identificabile, e grazie anche al fatto che le specie dotate di barrel, i roditori, sono gli animali da laboratorio più comuni. La barrel cortex e le sue interconnessioni neuronali sono stati oggetto delle ricerche più disparate in questi ultimi decenni. Attualmente, alcuni studi (come questo) non mirano solamente a comprendere meglio la barrel cortex, ma anche ad analizzare problematiche in campi scientifici collegati, utilizzando la barrel cortex come modello base.

In questo lavoro, sono stati evocati segnali LFP nella barrel cortex tramite deflessioni ripetute dei baffi dell'animale, realizzate in modo controllato tramite un sistema di deflessione piezoelettrica a closed-loop innescato da un sistema di acquisizione LabView. Le risposte evocate generate nella barrel dalla stimolazione ripetuta dei baffi presentano elevata variabilità nella forma e nelle latenze temporali. Inoltre, il tipo di anestesia utilizzata può influenzare profondamente il profilo della risposta evocata. Questo studio riporta i risultati preliminari sulla variabilità della risposta neuronale e sull'effetto di due anestetici di uso comune su questi segnali, confrontando le distribuzioni delle

risposte evocate in ratti anestetizzati con tiletamina-xylazina (il quale agisce prevalentemente sui recettori eccitatori di tipo NMDA) e uretano (che agisce in modo più bilanciato e complesso su entrambi i sistemi eccitatori ed inibitori, preservando la plasticità sinaptica). Sono state analizzate e discusse alcune caratteristiche rappresentative del segnale evocato (ad esempio, le latenze temporali e l'ampiezza degli eventi), registrato a varie profondità corticali. Per tutte le prondità corticali acquisite, sono state stimate le distribuzioni statistiche di tali parametri, in modo da valutare la variabilità degli LFP evocati dalle stimolazioni meccaniche individuali delle vibrisse del ratto lungo l'intera colonna corticale. I primi risultati presentano una grande variabilità nelle risposte corticali, sia in latenza che in ampiezza. Inoltre, è stata riscontrata una differenza significativa nella latenza del primo picco principale delle risposte evocate: gli LFP evocati in animali anestetizzati con tiletamina-xylazina presentavano una latenza più lunga di quelli registrati in ratti anestetizzati con uretano. Inoltre, le distribuzioni dei parametri analizzati erano più strette e piccate in uretano, in corrispondenza di tutte le profondità corticali. Questo comportamento è sicuramente da attribuire al differente meccanismo d'azione dei due anestetici su specifici recettori sinaptici, e quindi nell'elaborazione e nella trasmissione dell'informazione sensoriale lungo tutto il percorso corticale.

E' stato inoltre discusso il ruolo della attività basale nella modulazione della risposta evocata. A questo proposito, è stata registrata l'attività spontanea in corrispondenza dei vari layer corticali ed analizzata nel contesto statistico delle "valanghe neuronali". Una valanga neuronale è una cascata di attività elettrica in una rete neuronale, la cui distribuzione statistica dei parametri principali (dimensione e vita media) può essere approssimata da una legge di potenza. La distribuzione delle dimensioni di una valanga in una rete neuronale segue una legge di potenza del tipo $P(s) \propto s^{-\alpha}$, con $\alpha \sim 1.5$. Tale esponente è un riflesso delle correlazioni spaziali a lungo raggio nell'attività neuronale spontanea. Dal momento che i picchi negativi (nLFPs) nelle tracce

elettrofisiologiche originano dalla somma di potenziali d'azione sincronizzati generati da neuroni posti nelle vicinanze dell'elettrodo di registrazione, ci siamo chiesti se fosse possibile modellizare i singoli nLFP registrati nell'attività basale tramite un singolo elettrodo come il risultato di valanghe neuronali locali. Pertanto, abbiamo analizzato la distribuzione della dimensione (cioè l'ampiezza in μV) di tali picchi, in modo da identificare una distribuzione power-law appropriata, che potesse descrivere anche le registrazioni a singolo elettrodo.

Infine, sono presentate e discusse le prime registrazioni in assoluto degli LFP evocati lungo un'intera colonna corticale ottenute tramite l'ultima generazione di chip impiantabili a tecnologia CMOS. Questi ultimi presentano una matrice di 256 siti di registrazione, organizzata secondo due possibili topologie, 16×16 o 4×64, e avente una distanza tra gli elettrodi pari a 15 μm o 33 μm rispettivamente. Una precisa dinamica di propagazione dei potenziali evocati può già essere riconosciuta in questi primissimi profili corticali.

Nel prossimo futuro, l'uso di questi dispositivi a semiconduttore potrà aiutare a comprendere il decorso di sindromi neurodegerative come il Parkinson o l'Alzheimer, associando sintomi e comportamenti tipo della malattia a specifiche caratteristiche neuronali. I chip impiantabili potranno anche essere utilizzati come 'electroceuticals', ossia potranno aiutare a rallentare (o addirittura a capovolgere) il decorso delle malattie neurogenerative, costituendo le basi di protesi neuronali in grado di sostenere fisicamente o allenare funzionalmente le popolazioni neuronali danneggiate.

L'identificazione e il rilevamento di segnali neuronali ad alta risoluzione aiuterà anche a sviluppare complesse interfacce cervello-macchina, che consentiranno il controllo di protesi intelligenti e che forniranno sofisticati meccanismi di feedback a chi ha perso l'uso di alcune parti del proprio corpo o determinate funzioni cerebrali.

Contents

List of Publications

International Journal Publications

C. Cecchetto, R. Oboe and S. Vassanelli, "A closed-loop whisker stimulator design for electrophysiological experiments in rat barrel cortex", *Journal of Neuroscience Methods [in preparation].*

M. Mahmud, **C. Cecchetto** and S. Vassanelli, "An Automated Method for Characterization of Evoked Single Local Field Potentials Recorded from Rat Barrel Cortex Under Mechanical Whisker Stimulation", *Cognitive Computation, 2016 [in press].*

M. Rubega, **C. Cecchetto**, S. Vassanelli, and G. Sparacino, "Algorithm and software to automatically identify latency and amplitude features of local field potentials recorded in electrophysiological investigation", *Source Code for Biology and Medicine [submitted].*

National Journal Publications

C. Cecchetto, M. Maschietto, P. Boccaccio, and S. Vassanelli, "Increased Potassium Membrane Conductance in Transfected CHO-K1 Cells After Exposure to Low-Frequency and Low-Intensity Magnetic Fields", *LNL Annual Report 2013*, vol. Applied, General & Interdisciplinary Physics, pp. 93-94, 2014.

C. Cecchetto, M. Maschietto, P. Boccaccio, and S. Vassanelli, "Effect of Low-Frequency and Low-Intensity Magnetic Fields on Potassium Membrane Conductance in CHO-K1 Cells Expressing Kv1.3 Channel", *LNL Annual Report 2012*, vol. Applied, General & Interdisciplinary Physics, pp. 162-163, 2013.

Conference Proceedings

C. Cecchetto, M. Mahmud, and S. Vassanelli, "Anesthesia Effect on Single Local Field Potentials Variability in Rat Barrel Cortex: Preliminary Results". in *Conf Proc IEEE Eng Med Biol Soc*, 2015, pp. 4721-4724.

C. Cecchetto, S. Schröder, S. Keil, M. Mahmud, E. Brose, Ö. Dogan, G. Bertotti, D. Wolanski, B. Tillack, J. Schneidewind, H. Gargouri, M. Arens, J. Bruns, B. Szyszka, R. Thewes, and S. Vassanelli, "Imaging Local Field Potentials in the Rat Barrel Cortex", in *Proc Intl Conf Intell Info BioMed Sci (ICIIBMS 2015)*, Okinawa, Japan, 2015, pp. 296-299.

G. Frigo, M. Rubega, G. Lezziero, R. Fontana, **C. Cecchetto**, S. Vassanelli, G. Sparacino, and M. Bertocco, "A software-based platform for multichannel electrophysiological data acquisition", in *Proc 2015 IEEE Intl Sympo Med Measurem App (MeMeA)*, 2015, pp. 353-358.

M. Rubega, **C. Cecchetto**, S. Vassanelli, and G. Sparacino, "Automated Analysis of Local Field Potentials Evoked by Mechanical Whisker Stimulation in Rat Barrel Cortex", in *Conf Proc IEEE Eng Med Biol Soc*, 2015, pp. 1520-1523.

S. Schröder, **C. Cecchetto**, S. Keil, M. Mahmud, E. Brose, Ö. Dogan, G. Bertotti, D. Wolanski, Bernd Tillack, J. Schneidewind, H. Gargouri, M. Arens, J. Bruns, B. Szyszka, S. Vassanelli, and Roland Thewes, "CMOS-Compatible Purely Capacitive Interfaces for High-Density In-Vivo Recording from Neural Tissue", in *Proc Biomed Circ Syst Conf (BioCAS2015)*, Atlanta, Georgia, USA. 2015, pp. 1-4

Other Publications (Posters)

C. Cecchetto, M. Maschietto, P. Boccaccio, S. Vassanelli, "Effect of Low-Frequency and Low-Intensity Magnetic Fields on Potassium Membrane Conductance in Transfected CHO-K1 Cells", Poster at *XV Congress of the Italian Society of Neuroscience (SINS)*, Rome, Italy, 3 Oct 2013.

C. Cecchetto, M. Maschietto, S. Girardi, S. Vassanelli, "Variability of LFP Responses in the Rat Barrel Cortex upon Single Whisker Stimulation", Poster at *9th FENS Forum of Neuroscience*, Milan, Italy, 5 Jul 2014.

Other Publications (available only in the arXiv online archive)

C. Cecchetto, M. Maschietto, P. Boccaccio, and S. Vassanelli, "Enhancement of Kv1.3 Potassium Conductance by Extremely Low Frequency Electromagnetic Field", arXiv:1508.06135 [physics, q-bio], Aug. 2015, http://arxiv.org/abs/1508.06135.

List of Figures

List of Tables

Introduction

The rat barrel cortex, a specific area of the primary somatosensory cortex, is a widely used model of information processing in the somatosensory area, thanks to its precise and easily recognizable organization. Neural circuits of the rat barrel cortex are processing input information from the rat's whiskers. This work aims to deeply investigate the evoked responses generated in the neuronal circuits of the barrel cortex through conventional (i.e. Ag/AgCl electrodes) and innovative (i.e. high-resolution implantable needle chips) recording tools. Evoked Local Field Potentials (LFPs) generated in the barrel cortex by repetitive deflections of rat whiskers show large variability in shapes and timings. The variability of these signals is carefully evaluated by the analysis of the main parameters that describe the shape of the response. Moreover, the spontaneous background activity of cortical networks is thoroughly analyzed in the statistical framework of the 'neuronal avalanches'.

The thesis is organized into eight chapters. Chapters 1, 2 and 3 contain background material as of literature review on the evoked response, the spontaneous activity and the organization of the whisker-barrel somatosensory system. Chapters 4 mainly describes methods for system setup and signal acquisition, Chapter 5 contains the main results of this work, Chapter 6 contains a summary and Chapter 7 an outlook on future work. Chapter 8 presents a possible biomedical application of the recording CMOS-based devices used in this study.

The detailed contents are listed in the following:

- In Chapter 1, the main characteristics of the evoked LFP response generated in the barrel cortex by whisker deflections are explained. The spatial and the temporal variability of these signals are discussed, along with the effects

of the anesthesia on their shape and timings.

- In Chapter 2, the background basal activity and the critical dynamics of cortical networks are discussed. The statistical framework of the 'neuronal avalanches' is explained.

- In Chapter 3, an overview of the vibrissa-barrel system is given. The main anatomical and physiological details of the barrel cortex, the follicle innervation, the trigeminal ganglion, the thalamus and the neuronal projections are described.

- In Chapter 4, the methods and techniques for signal acquisition and analysis are described. The whisker stimulation system is illustrated and the acquisition setup for conventional eletrodes is delineated. The CMOS-based implantable chips are presented in details, along with their fabrication process and their system setup for acquisition. The software for signal acquisition and data analysis is presented.

- In Chapter 5, the main findings of this study are presented and discussed: the fine control of the whisker displacement through the closed-loop stimulation system, the variability of the main parameters of the evoked response and the statistical analysis of the spontaneous activity. One of the first ever measurements of a cortical profile of the evoked response by means of high-resolution CMOS-based needle chips is reported and the position of the recording site is verified by histological analyses of the tissue.

- In Chapter 6, the contributions of this thesis are briefly summarized and an evaluation of the work is carried out.

- In Chapter 7, an outlook on possible extensions and future objectives of the presented work is provided.

- In Chapter 8, a possible application of the implantable CMOS needle chip in the biomedical field as 'electroceuticals' is presented and discussed.

In the Appendix, a previous work on the effects of electromagnetic fields on the conductance of potassium channels expressed in CHO-K1 cells is presented.

Chapter 1

Evoked LFPs Variability

1.1 Spatial Variability

Local Field Potentials (LFPs) are electrical potentials that can be recorded from the cortical tissue and that summate excitatory and inhibitory postsynaptic potentials of many cells in the neighborhood of the electrode's tip (Kandel [2012]). Local Field Potentials in the cortex are dominated by the electrical activity of pyramidal cells, whose apical dendrites generate large dipoles extending through almost all the cortical depth (Barth & Di [1991]; Barth *et al.* [1989]; Di *et al.* [1990]; Kandel [2012]). When the activity of nearby neurons is synchronized by a sensory stimulus, it produces a distinct and characteristic sequence of waves: the evoked potential. In the case of the barrel cortex sensory system, the evoked maximal peak-to-peak amplitude can be obtained in a particular barrel by stimulating the corresponding whisker. The LFPs evoked by stimulating the other whiskers, surrounding the principal one, have smaller amplitudes. These potentials can be attributed to passive electric field flow from the neighboring columns or activation of neurons in the central column by the lateral routes from the nearby whiskers.

In order to understand the consecutive activation steps of cortical processing one should first separate the components forming up each evoked response. The evoked LFP consists of three main waves: the response onset, (about 5 ms latency after stimulation, see also Feature 1 and ROL in Figure 4.13), the response principal peak (about 10 ms after stimulus, Feature 2 and RPL in Figure 4.13) and the response positive rebound (18-40 ms after stimulus, Feature 3 in Figure

4.13). The time course of the response negative peak corresponds to the shortest latencies distribution of single unit responses of pyramidal cells located in the central column (Armstrong-James *et al.* [1992]; Jones & Diamond [1995]; Shimegi *et al.* [1999]). In layer IV, the average latency for EPSPs (excitatory postsynaptic potentials) following whisker stimulation is about 6.9 ms (Wilent & Contreras [2004]) and for action potentials 7.2 ms (Armstrong-James *et al.* [1992]). In layer Vb, the average latency for action potentials is 8.4 ms, while excitation is produced by whisker deflection in layer II and III at an average of 3.5-4 ms and 2 ms after excitation in layer IV cells, respectively (Armstrong-James *et al.* [1992]).

As we already mentioned, the negative peak amplitude drops rapidly when the stimulated whisker is located far away from the principal one: this suggests that this short latency wave is mainly associated to the activity evoked in the central column by the principal whisker and is not transmitted along the whole barrel field. Conversely, the positive rebound of the response shows an opposite behavior (Kublik [2004]): its maximal amplitude is smaller than that of the negative principal peak and its extent on the cortical surface is much wider. This wave may probably result from a simultaneous activation of many columns in a large portion of the barrel field, transmitted by long distance intra-cortical connections within supragranular layers or by multi-whisker thalamic input. Moreover, the positive rebound is more pronounced in non-anesthetized rats (Kublik [2004]), thus it might represent surrounding activity transmitted by cortico-cortical connections engaged in higher order neuronal functions.

During all types of neuronal activity, currents flow through cellular membranes. From the point of view of the extracellular space these membrane currents can be seen as sinks (inward currents) and sources (outward currents). Sinks and sources are the link between field potentials and neuronal activities: they are the local generators of field potentials in the tissue and are generated by the activation of neuronal ensembles. The distribution of local ionic currents that flow through neuronal membranes during neuronal activity can be computed from high-resolution recordings of LFPs generated by neuronal networks. To this end, the Current Source Density (CSD) analysis has proved to be a powerful method when applied to high-resolution records, giving direct access to physiological information that can be used to dissect activity patterns within the network. Sinks and sources, like

electrical charges, are spatially localized phenomena: therefore, the CSD method leads to a far higher spatial resolution in studying neural activity. Furthermore, this method helps to unveil important physiological information often concealed in the raw data. In this way, current source density (CSD) analysis attributed two main sources of cortical evoked potentials to two different groups of pyramidal cells, in supragranular (II-III) and infragranular (V-VI) cortical layers (Barth *et al.* [1989]; Di *et al.* [1990]; Mitzdorf [1985]; Wróbel [1997]).

1.1.1 Studying LFPs with multisite probes

In order to map the evoked responses generated throughout all the cortical layers, multisite recording techniques have been developed recently to overcome the limitations of previous one-site approaches (i.e., conventional Ag/AgCl electrodes) and allowing to record simultaneously from large neuronal populations with high spatial resolution in different brain regions (i.e., by using implantable EOSFET needle chips).

In our study, implantable probes, thanks to a multiplexed array of 256 capacitive microelectrodes, enable to record two-dimensional LFP profiles with unprecedented spatial resolution (down to 15 μm) and to image LFPs within the rat barrel cortex from different depths simultaneously. Moreover, chip dimensions are specifically designed to fit the cortical barrel size: the width of the implantable needle (300 μm) is very near to the typical mean diameter of a barrel. Therefore, using these implantable sensors the propagation of LFPs along the 16 $\times$ 16 or 4 $\times$ 64 recording array can be exploited at different cortical depths. From this unprecedented resolution, unprecedented results stem in the recording and characterization of cortical LFPs, along with the newly approachable analysis of sensory information flows in the LFP domain inside a single barrel.

1.2 Temporal Variability

Whisking is one of the dominant contributors of sensory information in rodents. Through whisking rats can localize objects, detect textures and differentiate shapes very precisely. The whisker-somatosensory system in rats is able to respond to

single touching and stimulations of the vibrissae by the external environment. Therefore, single evoked potentials generated by singular deflections of the rat whiskers have great physiological relevance in barrel cortex studies. Averaging evoked signals on many repeated trials can only give a first rough estimate of the LFPs generated in the whisker somatosensory pathway in response to whisker stimulations. Moreover, studying only averaged signals is uncommon in neurophysiological investigations, since it may hide characteristic features and specificity of the neuronal response contained only in single evoked LFPs.

Generally speaking, the response to sensory stimulation depends on several factors, including both synaptic excitability of the individual cell under study and the state of the circuit (e.g., excitation, inhibition and disfacilitation) to which it belongs. When a number of sources contribute to an evoked response, each of the resulting subcomponents can be influenced by the background activity in a different way.

The time series of single trial evoked potentials typically have a random appearance, and their trial-to-trial variability (often as large as the response itself, both in anesthetized, awake and behaving animals) is commonly explained by a model in which random ongoing background activity is linearly combined with a stereotyped and stationary evoked response (Arieli *et al.* [1996]; Kisley & Gerstein [1999]; Truccolo *et al.* [2002]). Ongoing activity must play an important role in cortical function and cannot be ignored in exploration of cognitive processes.

The intensity and the shape of the evoked response depend on the state of local cortical networks at the time of the whisker stimulation. This neuronal state is constantly modulated by the ongoing activity (Arieli *et al.* [1996]; Musiał*et al.* [1998]), thus consecutive applications of an identical stimulus can evoke very different responses in the cortex from trial to trial (Kublik [2004]). In the absence of desynchronizing inputs, the membrane potential of cortical neurons fluctuates spontaneously between two sub-threshold values, a depolarized up state and a hyperpolarized down state (Sachdev *et al.* [2004]). These are naturally occurring state changes observed during slow wave sleep, in the anesthetized as well as in the awake rat and therefore represent an opportunity for investigating the ability of ongoing activity within cortical circuits to modulate the cortical response to sensory stimulation. Such modulation is usually quantified in terms of changes in the

level of synchrony of neuronal activity (Truccolo *et al.* [2002]) or stimulus-related changes in functional connectivity.

The traditional method for dealing with such huge variability is averaging signals over many trials (Aunon *et al.* [1981]; Dawson [1951]; Gerstein [1960]). However, such a manipulation requires the non-trivial assumption of linear superposition between uncorrelated ongoing background activity and a highly stereotyped, repeatable evoked response phase-locked to the external stimulus (Dawson [1954]). The evoked response component is treated as being time invariant and any change over trials in its amplitude, latency onset, or waveform is considered negligible. The usual method of measuring this component is to repeatedly present the same sensory stimulus and then average the post-stimulus potentials across a set of trials (ensemble average). Averaging is presumed to decrease the size of the noise component, while leaving the signal component unchanged and thus enhancing the signal-to-noise ratio. This approach tacitly assumes that variability reflects "noise", which is a problem for cortical processing and it could be overcome by the brain by proper averaging over populations of neurons. Numerous articles deal with the question of what the source of variability in the brain is (Arieli *et al.* [1996]; Kisley & Gerstein [1999]). This issue must be resolved in order to determine whether the neural code for information processing in the brain requires the averaged activity of many neurons.

Nevertheless, non-stationarity of the brain state can lead to non-stationarity of the so-called "repeatable" response (see Coenen [1995] for review), thus violating the assumptions necessary for averaging (Coppola *et al.* [1978]; Möcks *et al.* [1987]). In this case, an alternative model, referred to as the variable signal plus ongoing noise activity (VSPN) model, asserts that the stimulus-triggered response has a stereotyped waveform, but with variable amplitude and latency onset across trials. According to the VSPN model, after subtracting out the average response, the single trial residual time series contain two components: a stimulus phase-locked component generated by the trial-to-trial amplitude and latency variability and an ongoing noise component.

Event related modulation of statistical measures is commonly interpreted as due to fast changes in functional connectivity or other intrinsic neural parameters and opens the path for discovering temporal effects of neural dynamics generated

by the underlying physiology. For example, slow changes of global brain state involving arousal and attention could lead to fluctuations in the excitability level of cortical and subcortical neuronal populations, causing variability in the magnitude and in the timing of the evoked response (Brody [1998]; Mangun & Hillyard [1991]), but without significantly affecting the shape of the response. Trial-to-trial variability could also be related to the dependence of the amplitude of single trial evoked responses on the level of pre-stimulus ongoing activity (Başar *et al.* [1976, 1998]; Brandt & Jansen [1991]).

Since the aim of this study is to analyze single evoked responses by trial to trial, we had to make sure that the whiskers of the animal were stimulated always in the same manner. Therefore, in order to deflect precisely the rat whiskers in a repeatable and controlled fashion, we designed a new stimulation protocol by means of a closed-loop control system based on the strain gauges placed onto the piezoelectric bender. Single displacements of the whisker were also monitored through a high-speed camera system and then analyzed offline through a free software for video tracking (see Materials and Methods, chapter 4, section 4.4).

If successive whisker stimulations are too close in time, the somatosensory system may encounter "saturation" phenomena, also related to the transmission dynamics of the sensory information at the level of follicular receptors. Consequently, the number of spikes evoked by each cycle of whisker deflection could be reduced as stimulation frequency increases (Alloway [2008]). Many studies indicate that repetitive whisker stimulation reduces the effectiveness of each stimulus for evoking responses in barrel cortex (Ahissar *et al.* [2001]; Castro-Alamancos [2004]; Garabedian *et al.* [2003]; Higley & Contreras [2006]; Khatri *et al.* [2004]). As a result, the responsiveness of the sensory system to a frequent stimulus can change over time. In order to evaluate the independence of single trials from each other, we simultaneously recorded the evoked LFPs from the barrel cortex and the trigeminal ganglion, being the later the first stage of processing of whisker information in the somatosensory pathway. In this way, we could investigate if phenomena related to adaptation, habituation or reinforcement are present during our stimulation protocol.

Once recorded, single evoked LFPs were analyzed and the variability of the signals was assessed by extracting some important parameters of the evoked re-

sponse by designing and then using a custom MATLAB program, as explained in the Materials and Methods section (see chapter 4, section 4.10.3).

1.3 Anesthesia Effect on Variability

In this study, two different type of anesthesia was used and compared, urethane and tiletamine-xylazine. Urethane is a widely used anesthetic for animal studies, because of its minimal effects on cardiovascular and respiratory systems and preservation of spinal reflexes. Despite its usefulness and diffusion in animal research, there are no exhaustive reports concerning its molecular targets: in fact, it has a wide spectrum of action on ion channels that is distinct from other anesthetics. The only compound with a spectrum of action similar to urethane is ethanol.

Urethane affects both inhibitory and excitatory systems and the magnitude of these changes is less than the one seen with anesthetics that are more selective for one system (e.g., ketamine and NMDA receptor, propofol and $GABA_A$ receptor). At concentrations close to half (50%) of his effective concentration, urethane has modest effects on many neuronal channels (GABA, Glycine, AMPA, NMDA and nACh), suggesting the lack of a single predominant target for its action (Hara & Harris [2002]). These results not only give insight into the molecular mechanism of urethane but also caution that his effects on multiple neurotransmitter systems may complicate neurophysiologic recordings from animals treated with this particular compound. Even in this study, detecting and recording evoked responses from urethane-anesthetized animals was not as straightforward as in rats anesthetized with tiletamine-xylazine: the typical one-negative-peak response generated in layer IV of the barrel cortex by the stimulation of the whiskers was not always so clear in all the urethane-anesthetized animals. Moreover, the trial-to-trial shape variability of the evoked signals was much more marked under this kind of anesthesia, leading also to major issues on the subsequent analysis and extraction of information from these responses (see chapter 5, section 5.2.2 for details).

It is assumed that urethane-anesthetized animals present similar physiologic and pharmacologic traits to those observed in naturally sleeping unanesthetized

animals. Conversely, ketamine (a dissociative anesthetic chemically related to tiletamine, used in this study) has a more specific action, since it dramatically inhibits the channel function of N-methyl-d-aspartate (NMDA) receptors at a clinical concentration, without substantial alteration of the function of GABA or other receptors. NMDA receptors mediate nociceptive neurotransmission in the CNS and both NMDA and AMPA (α-amino-3-hydroxy-5-methyl-4-isoxazolepropionic acid) receptors are important for memory. Therefore, synaptic plasticity is likely to be somewhat altered in animals anesthetized with this compound, whereas is expected to be preserved in urethane-anesthetized animals. Ketamine is able to induce spike-waves in cats (Black *et al.* [1980]) and it is often used to study neural activity during spike-waves (Steriade *et al.* [1998]). Furthermore, it has been shown that ketamine can regulate the frequency of high-voltage spindle rhythmicity in rats (Buzsáki [1991]).

The variability of the evoked response, along with the shape and the frequency content of the ongoing background activity, is likely to be closely related to the type and the depth of anesthesia (high, medium or light). Trial-to-trial variability is reported to be highest under medium levels of ketamine-xylazine anesthesia, during which ongoing cortical activity exhibits rhythmic population bursting activity (Kisley & Gerstein [1999]). Under ketamine-xylazine anesthesia, average evoked responses are expected to differ slightly between the three different depths of anesthesia, while the single trial variability may change quite dramatically (Kisley & Gerstein [1999]). The same study (performed on the modulation of auditory-evoked signals in the rat cortex) showed from many example single trials that the evoked response is more consistent under deep and light anesthesia, when compared with the medium one. Under this medium level of anesthesia, the peak amplitude of the evoked response varied widely and the overall time course of the response (the shape) changed significantly from one trial to the other. This extreme variability observed under moderate levels of anesthesia could be a primarily reflection of oscillating excitability in both thalamic and cortical neurons, possibly generated by large-scale changes occurring in thalamocortical circuits during typical rhythms associated with sleep and anesthesia (see McCormick & Bal [1997]; Steriade [1997]). Moreover, the ongoing activity was found to modulate both amplitude and shape (including latency) of evoked LFPs and unit activity in a way

that cannot be explained by a mere linear superposition of a stereotyped evoked response and background activity. This breakdown of the linear model is likely due to rapid transitions between different levels of thalamocortical excitability, although the resting brain state is relatively fixed.

Principal Component Analysis (PCA) represent a valid method for quantifying the shape of an entire single trial waveform and the observed variability in evoked responses (Kisley & Gerstein [1999]; Kublik *et al.* [2001]; Musiał*et al.* [1998]). This type of analysis has seen increasing application in neuroscience, including sorting of extracellularly recorded action potential waveforms (Abeles & Goldstein [1977]), analysis of evoked potentials (Chapman & McCrary [1995]), synaptic potentials (Astrelin *et al.* [1998]), evoked extracellular field potentials (Musiał*et al.* [1998]), and current source density (CSD) waveforms (Di *et al.* [1990]). This type of analysis allows classification of single trial evoked field potential responses into groups of similarly shaped waveforms, revealing the subcomponents of the evoked signals while reducing single trial variability. However, in this study we decide to perform a preliminary analysis of the trial-to-trial variability by computing the statistical distributions of some relevant signal parameters, both in the temporal and in the voltage domain, and to assess the effects of the anesthesia on the evoked responses by comparing the two distributions obtained under urethane and tiletamine-xylazine anesthesia. This represent a much more direct method of evaluation of the evoked responses and do not require very complex routines to analyze the data.

Chapter 2

Spontaneous Background Activity

2.1 Correlation Between Ongoing and Evoked Activity

Knowing the envelope and the main principles that drive the spontaneous background activity is crucial when studying evoked cortical responses. In fact, the ongoing basal activity of cortical neuronal networks may contribute to modulate both amplitude and shape (including latency) of evoked LFPs, in a way that cannot be predicted by a mere linear superposition of background activity and a stereotyped evoked response (Kisley & Gerstein [1999]).

As it emerges in Yu *et al.* [2013], the ongoing resting activity in cortical networks organizes close to an effective thermodynamic critical point, suggesting the possibility that a critical state may in effect be described by methodology from thermodynamic equilibrium. Careful analysis of the statistical properties of neural dynamics under no external inputs has identified complex patterns of activity previously ignored as 'background noise dynamics' (Chialvo [2010]). The fact is that brain activity is always essentially arrhythmic and under healthy conditions, no brain temporal scale dominates over the others, resulting in power spectral densities decaying as '$1/f$ noise'.

In order to study the interaction between the ongoing background activity

and the evoked response, it is important to understand if the system is poised at criticality in his normally 'resting' state (and which type of criticality, if super- or sub-criticality), when we alter the system with an external stimulus. This represents the first step that has to be accomplished in order to predict the behavior of a neuronal network in response to an external force. Based on modeling (Tomen *et al.* [2014]), it has been suggested that cortical networks, by operating at the sub-critical to critical transition region, could dramatically enhance stimulus representation.

2.2 Critical Network Dynamics in the Brain

The human brain is a large collection of a hundred specialized modules with different functions. At the smallest grain, the cerebral cortex consists of about 10^{10} neurons that form a highly interconnected network. Each neuronal cell continuously receives thousands of excitatory inputs from other neurons. One of the simplest things we do not know yet about the brain is how the cortex, being a mainly excitatory network, prevents the expected explosive propagation of activity but still transmits information across areas. If the average number of neurons activated by one neuron is too high (i.e., supercritical) this would result in a massive activation of the entire network, while if it is too low (i.e., subcritical), the propagation would die out. The critical regime is the one in which these opposing processes are balanced (Chialvo [2004]).

Why neuronal networks should exhibit a critical behavior? An easy answer could be that brains has to be critical because the world in which they must live (and survive) is to some degree critical as well (Chialvo [2010]). As the largest number of metastable states exists at a point near the transition, the brain can then be accessing the largest repertoire of behaviors in a flexible way. Thus, 'critical' brains are needed to navigate a complex, critical world, where surprising events still have a finite chance of occurring.

2.3 UP and DOWN States and Self-Organized Criticality

During sleep, under anesthesia and in vitro, cortical neurons in sensory, motor, association and executive areas fluctuate between two different states, which are characterized by distinct membrane potentials and spike rates (Millman *et al.* [2010]), named up and down states. Another phenomenon observed in preparations that can exhibit up and down states too – anesthetized rats, brain slices and cultures devoid of sensory inputs, as well as awake monkey cortex – is self-organized criticality (SOC). SOC is characterized by avalanches of activity with size distribution that obeys a power law with a critical exponent of about -3/2 and a branching parameter (i.e., the ratio between the number of descendants and ancestors of a process at a given time step) near unity. Self-organized criticality characterizes the spread of earthquakes, forest fires and avalanches of idealized grains falling down from a sandpile (Bak *et al.* [1987]). Analogously, neuronal activity propagates in 'neuronal avalanches'. Recent work has demonstrated SOC in conservative neuronal network models but critical behavior breaks down when biologically realistic 'leaky' neurons are introduced (Millman *et al.* [2010]). Non-conservative leaky integrate-and-fire neurons with short-term synaptic depression typically display two stable activity levels, corresponding to up and down states, and these networks switch spontaneously between these two states, with up states regarded as critical and down states subcritical. Whereas down states are quiescent, up states have high synaptic and spiking activity, resembling that of REM sleep and wakefulness. Up and down state behavior is also a network-level phenomenon: a high fraction of neurons in large cortical areas alternate between states at the same time. Therefore, distinct avalanche behaviors depend also on differences in synaptic activity and neuronal responsiveness between up and down states.

2.4 Statistical Analysis: "Neuronal Avalanches"

Beggs and Plenz (Beggs & Plenz [2003]) studied the spontaneous neuronal activity of cultured and acute slices of rat cortex using 64-channel multielectrode arrays. They documented that spontaneous activity in the cortex typically shows intermittent burst of activity. These scale-free activation patterns, called *neuronal avalanches*, provide evidence for criticality in the brain. After computing the statistics of several days' worth of continuous cortical activity with a few millions of events, Beggs and Plenz showed that the avalanche size distributions, expressed as total number of electrodes activated per frame, demonstrates the existence of a power law, with exponent $\alpha \propto -1.5$.

Neuronal avalanches are a previously unknown but robust form of synchronous activity in the cortex, first measured in organotypic somatosensory cortex cultures from rat, grown on microelectrode arrays (MEA). A neuronal avalanche is a cascade of bursts of activity in neuronal networks whose size distribution can be approximated by a power law, as in critical sandpile models (Bak *et al.* [1987]). The size distribution of neuronal avalanches in cortical networks has been reported to follow a power law distribution $e^{-\alpha}$ with an exponent α close to 1.5, regardless of the animal species, which is a reflection of long-range spatial correlations in spontaneous neuronal activity (Klaus *et al.* [2011]). Avalanches reflect fast propagation of local synchrony, display a rich spatiotemporal diversity and recur over several hours under various experimental conditions. The statistical organization of pattern sizes is invariant to the choice of the spatial scale, demonstrating that the functional linking of various cortical sites into avalanches occurs on all spatial scales with a fractal organization (Plenz & Thiagarajan [2007]). The driving mechanisms behind avalanche activity are non-local, with all scales contributing to system behavior (Massobrio *et al.* [2015]).

Neuronal avalanches are defined as spatio-temporal clusters of negative LFPs peaks (nLFPs) on the MEA (Beggs & Plenz [2003]). So in order to easily identify avalanches from many electrodes records (as in neurons cultured on MEA), a binning of the time scale has to be accomplished, and then raster plots has to be constructed starting from the electrophysiological raw traces. This kind of plots reports only the time points where nLFPs are detected (by imposing a particular

threshold in the voltage domain and checking which nLFPs crosses it). A neuronal avalanche consists of a consecutive series of time bins of width ε that contain at least one nLFP on any of the electrodes. Each avalanche is preceded and ended by at least one time bin with no activity. Without loss of generality, usually analyses are done with bin ε individually estimated for each culture from the average inter nLFPs interval on the array, normally ranging between 3 and 6 ms for all cultures (Lombardi *et al.* [2014]). The avalanche size is defined as the sum of absolute nLFP amplitudes (μV) on active electrodes (i.e. the electrodes where the amplitude of detected nLFPs crosses the imposed threshold) or simply as the total number of active electrodes. Size distributions are obtained using logarithmic binning for sizes expressed in μV. Avalanche duration (or lifetime) is given by the number n of consecutive non-empty bins times the bin amplitude. A quiet time is defined as the time interval between the end of an avalanche and the start of the following one. A waiting time is the time interval between the start of an avalanche and the start of the following one. Obviously, the following equality holds: waiting time = lifetime + quiet time.

Neuronal avalanches are seen in cultures and acute cortical slices with thousands of avalanches of different duration per hour and their distributions follow power-laws, with coefficients equal to (Beggs & Plenz [2003]):

- $\alpha \sim$1.5 for sizes
- $\alpha \sim$2 for lifetimes

Beggs and Plenz also computed an average branching activation ratio close to unity. This branching ratio (calculated as the ratio between the current and future number of activated electrodes) is thought to optimize information transmission in feed-forward networks models. Further analyses (Lombardi *et al.* [2012]) demonstrated that avalanche size and inter-avalanche quiet times are correlated, and a characteristic periodicity in avalanche occurrence, typical of θ and β or γ oscillations, could also be pointed out. This observation is in line with previous pharmacological results that associate nested oscillations and neuronal avalanches in cortex (Gireesh & Plenz [2008]). These aspects demonstrating criticality should be quantitatively accounted for by future theories of cortical dynamics.

For what regards our particular study, since negative LFP peaks (nLFPs) originates from the sum of synchronized Action Potentials (AP) generated by neurons placed near the tip of the recording electrode, we wondered if it were possible to model single nLFPs in the spontaneous ongoing activity of anesthetized rats sampled by only one electrode as the result of local neuronal avalanches. Therefore, we analyzed the size (i.e., the amplitude of these nLFPs in μV) distribution of these peaks in order to identify a suitable power-law distribution that could describe also single-electrode records. This kind of analysis is of particular interest, since neuronal avalanches have never been studied in barrel cortex during *in-vivo* experiments before.

Chapter 3

Vibrissa–Barrel System

3.1 Overview

The vibrissa-barrel system in rodents (Armstrong-James & Fox [1987]; Jones & Diamond [1995]; Simons [1978]; Welker [1971]; Woolsey & Van der Loos [1970]) offers excellent conditions for studying the mechanisms of sensory information processing, because of its unique structural-functional organization that facilitates the analysis of the neural mechanisms that mediate development, plasticity, and sensory coding (Alloway [2008]). Regarding this study, the barrel cortex, being a well-known neuronal network and one of the most widely studied functional unit in the mammalian brain where it constitutes an early stage of cortical processing for tactile information, represents the ideal system for testing the validity of high-resolution electrical imaging methods by means of implantable CMOS chips. Moreover, the barrel cortex represents an optimal test-bed system to analyze both the evoked response generated by the whisker stimulation and the ongoing basal activity spontaneously generated in these cortical circuits.

The rat somatosensory cortex contains an isomorphic map of the mystacial whiskers, i.e. each vibrissa is specifically mapped onto neuronal populations, or barrels, that can be found in layer IV (the main input layer of the somatosensory pathway) and that are separated from each other by narrower zones called septa (Land & Simons [1985]; Woolsey & Van der Loos [1970]). Moreover, single whiskers are represented by relatively well-defined groups of neurons at each step of the sensory pathway. In the principal trigeminal nucleus of the brain-

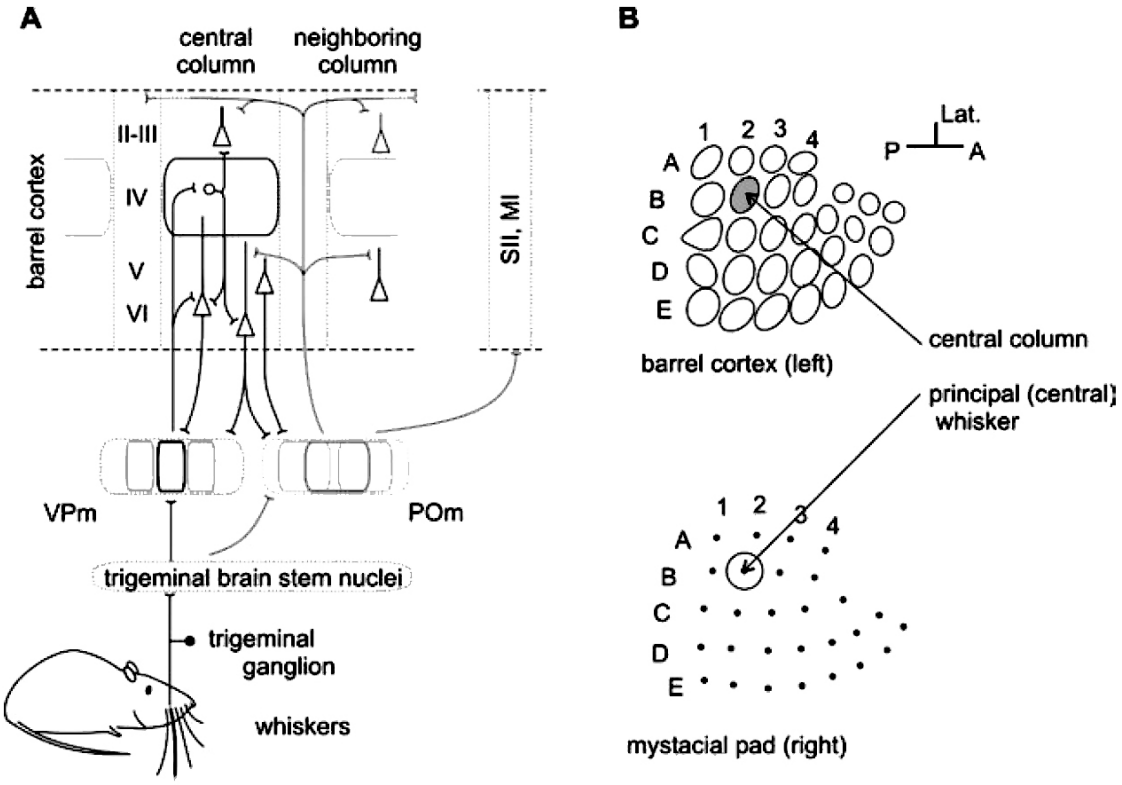

Figure 3.1: A simplified schema of the rat vibrissa-barrel system from Kublik [2004]. (A) A sensory signal from a single vibrissa is transmitted through the lemniscal pathway with a relatively precise somatotopic mapping, going through separate "barreloids" in the ventral posteromedial nucleus (VPm) of the thalamus to individual "barrels" in layer IV of the primary sensory cortex. In the paralemniscal pathway, less precise somatotopic organization can be found: cells in the medial posterior nucleus of the thalamus (POm) receive information from multiple whiskers and send their axons to layers I and Va within a large portion of the barrel field and additionally to other cortical regions (S2, M1). Pyramidal cells in layers II-III are called supragranular and in layers V-VI infragranular. Axons from infragranular cells send cortico-thalamic fibers from layer VI to VPm, and from layer V and VI to the POm. (B) Lower panel: whiskers are organized on the mystacial pad in 5 rows, labeled from A to E. Consecutive whiskers are numbered from back to front on the snout. Upper panel: a scheme of the tangential section of the barrel cortex at the level of layer IV, showing a spatial organization of the barrel columns identical to that of the whiskers on the snout. A whisker and its corresponding column, located in the same position within the pattern (e.g., B2), are called principal whisker and principal column.

stem (PrV), these ensambles are called "barrelettes" (Jacquin & Rhodes [1983]; Killackey & Fleming [1985]; Ma [1991]; Ma & Woolsey [1984]); in the ventral posteromedial (VPm) nucleus of the thalamus, "barreloids" (Chmielowska *et al.* [1989]; Jones & Diamond [1995]; Land *et al.* [1995]) and finally, in layer IV of the primary somatosensory cortex, they are called "barrels".

The barrel-column, which forms the cortical processing unit of a single vibrissa, is composed of a vertical array of cells running orthogonally to the six-layered structure of the cortex, below and above the corresponding neurons of the single barrel in layer IV. Each column (called "barrel" because of its characteristic curved shape that resembles a barrel stave) measures about 300 μm in width and runs through the entire depth of the cortex, about 2 mm long in rats. The larger barrels are about 500 μm in width and about 300 μm along the axis of the row, with about 70 μm septa (Alloway [2008]). Each barrel-column is composed of an archetypical circuit that is repeated in each column, with each large barrel containing approximately 2000 neurons: of these, about 75% are excitatory and 25% are inhibitory (Pasternak & Woolsey [1975]). Such columns form within the sensory cortex a similar spatial pattern as the whiskers on the mystacial pad. Because of its simple grid-like organization, each barrel can be identified by its arc position (1-7, caudal to rostral) within a specific row (A-E, dorsal to ventral). This distinctive barrel-shaped pattern can be easily seen from a horizontal section of the tissue taken through layer IV (see also chapter 4, section 4.11 for histological techniques). Each barrel is selectively activated by the corresponding whisker on the contralateral whisker pad (Simons [1978]; Welker [1971, 1976]), in a way that the topological position of the barrel within the barrel field is identical to the topological position of its corresponding whisker.

The area of cortex devoted to the whiskers reflects the high innervation levels of the whisker follicles (see section 3.3). In absolute terms, the barrel field in the rat comprises from 4.7 to 6.4 mm^2, varying from animal to animal (Welker & Woolsey [1974]; Woolsey & Van der Loos [1970]).

Layer IV is the only one within the cortical layers that sends strong functional excitatory connections to all other layers within the column (Staiger *et al.* [2000]). Layer V is the only one within the column that receives functional excitatory input from all other cortical layers within the column (Staiger *et al.* [2000]). It has also

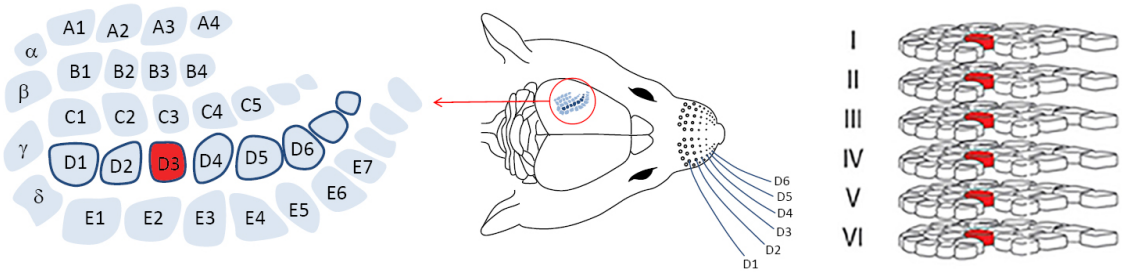

Figure 3.2: The barrel field organization and the barrel-whisker somatotopy.

been shown that within the whisker pad there is a "receptive field gradient" such that the larger, more caudal whiskers are represented by more cells than the rostral ones at each level in the brain: brain stem trigeminal nuclei, VPM thalamus and layer IV of the somatosensory cortex.

The similarity between columns in the barrel cortex and columns elsewhere in the brain (e.g., in the retina for the visual system) suggests that a great deal about the cortex in general can be learnt by investigating the columns in the barrel cortex in particular. This do not only include understanding connections within the column itself, but also understanding the connections between different columns and with other subcortical structures.

3.2 Afferent and Efferent Projections

In the barrel cortex, the most common cortical neuronal type is the pyramidal cell, which has an extensive vertical dendritic tree that can reach the cortical surface. Pyramidal cell bodies can be found in all cortical layers except layer I (thus called the molecular layer). Their axons usually give off recurrent collaterals that turn back and synapse on the superficial portions of the dendritic trees. Pyramidal cells are the only projection neurons of the cortex and they are excitatory neurons that release glutamate at their terminals. Other cortical cell types are local circuit neurons (interneurons) which have been classified based on their shape, their neurotransmitters and their specific pattern of projection. Neuronal cells tend to be sparse within the centers of the barrels and denser in the barrel wall.

The cells in the wall of the barrel tend to project their dendrites in toward the center of the barrel (Simons & Woolsey [1984]), again sparing the surrounding septal area between the barrels, where they pick up synaptic contacts from the thalamocortical afferents. Afferents from the specific nuclei of the thalamus terminate primarily in cortical layer IV, whereas non-specific afferents are distributed also in layers I-IV.

Recent work has demonstrated that the barrel cortex contains a rich and diverse neuronal organization in which local circuits are characterized by a high degree of connectional specificity, so as neurons within the barrel cortex have local connections and interactions that vary systematically with their laminar and columnar locations (Schubert *et al.* [2006]; Shepherd & Svoboda [2005]; Shepherd *et al.* [2005]).

A pathway comprising just three synapses connects the primary afferents carrying information from the whisker follicle receptors to the final link into layer IV of the cortex, producing the characteristic barrel pattern. Afferent signals coming from the follicular innervation travel past the cell bodies of the trigeminal ganglion (TG) and continue along the central branch to form synapses in the trigeminal nuclei (TN) of the brainstem. The trigeminal nuclei convey afferent vibrissal information to the thalamus via three main parallel pathways that then continue to the barrel field of the somatosensory cortex, some of them forming sensorimotor loops below the cortical level (Diamond *et al.* [2008]). These pathways are called lemniscal, paralemniscal and extralemniscal.

Neurons in the principal sensory trigeminal (PrV) nucleus are clustered into 'barrelettes'. The axons of these second-order neurons travel, via the lemniscal pathway, to the 'barreloids' of the dorsomedial section of the ventral posterior medial nucleus (VPMdm) of the thalamus. Both barrelettes and barreloids are sets of modules arranged as a topographic projection of the whiskers; neurons in a given module respond principally to the corresponding whisker, thus defining a single-whisker receptive field for the trigeminal sensory neurons. The axons of VPMdm neurons project to the primary somatosensory cortex (S1), where they terminate in the barrels of layer IV.

Neurons in the caudal part of the interpolaris division of the spinal trigeminal (SpVi) nucleus of the TN are also clustered into whisker-related barrelettes.

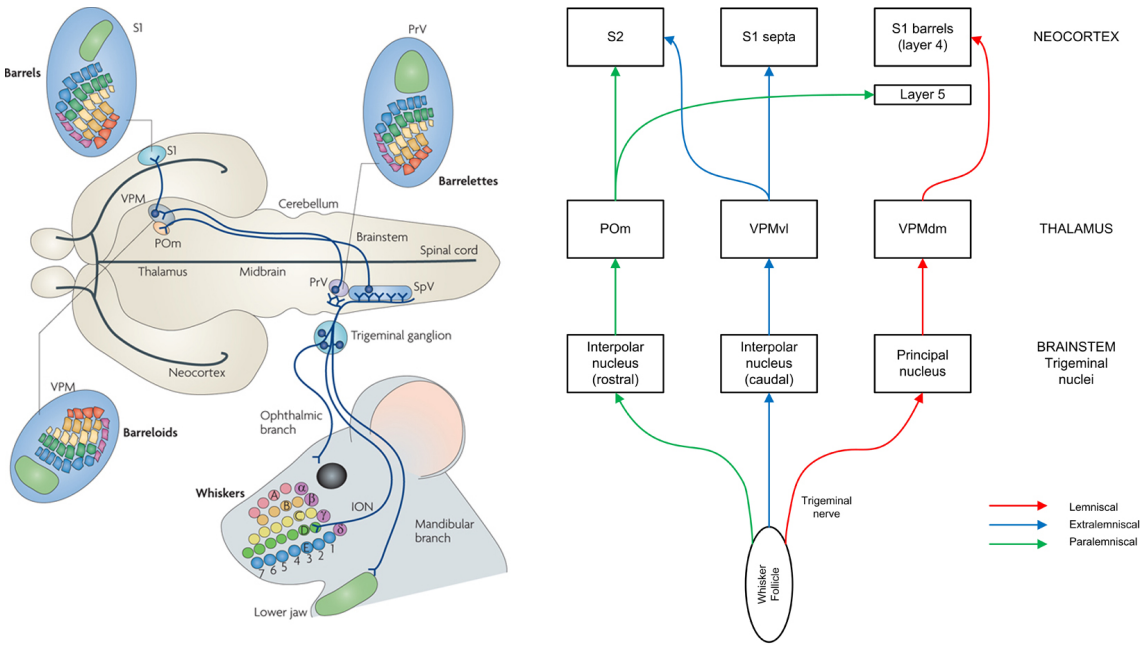

Figure 3.3: (Left) Connections in the barrel somatosensory system, from Erzurumlu *et al.* [2010]. (Right) The three different pathways to the barrel cortex (image by Peter Haslehurst, adapted from Diamond *et al.* [2008] and Fox [2008]).

Following the extralemniscal pathway, they project to the ventrolateral domain of the VPM (VPMvl), where neurons are clustered into the 'tails' of the VPMdm barreloids. The axons of VPMvl neurons project to the septa between the barrels of S1 and to the secondary somatosensory cortex (S2).

Conversely, neurons in the rostral part of the interpolar TN are not spatially clustered. They project to the medial sector of the posterior nucleus (POm) (and to a slender "tail" region in the ventrolateral part of VPM, see Chiaia *et al.* [1991]; Erzurumlu & Killackey [1980]; Peschanski [1984]; Pierret *et al.* [2000]; Rhoades *et al.* [1987]; Veinante *et al.* [2000]; Williams *et al.* [1994]). The axons of POm neurons project to target immediately ventral to the barrels, in layer Va of S1, S2 and to the primary motor cortex. Unlike the lemniscal pathway, the paralemniscal pathway is not spatially specific, integrating multiple-whisker information and defining a multi-whisker receptive field.

Thus, thalamo-cortical projections of the lemniscal and paralemniscal pathways terminate in separate parts of S1 barrel cortex: whereas the layer IV barrels receive dense inputs exclusively from the nucleus VPM (Chmielowska *et al.* [1989]; Killackey [1973]; Killackey & Leshin [1975]; Koralek *et al.* [1988]; Lu & Lin [1993]), the intervening septa receive dense inputs from POm and the slender tail region in VPM (Lu & Lin [1993]; Pierret *et al.* [2000]). The extragranular layers of the barrel cortex also receive segregated inputs from the lemniscal and paralemniscal pathways. VPM sends moderate projections to the adjoining parts of layers VI and Vb, as well as sparse projections to lower layer III (Lu & Lin [1993]). By comparison, less-dense secondary projections from POm terminate in layers I, II, III, and Va. Interestingly, paralemniscal information is transmitted to layers I and Va in both barrel and septal columns, but the projections to layer Va in the barrel columns are less dense than those to neighboring regions below the septa (Lu & Lin [1993]). Nonetheless, even though some paralemniscal information is sent to regions vertically aligned with the layer IV barrel compartments, VPM does not innervate layers I or Va, and the thalamo-cortical projections of the lemniscal and paralemniscal remain always segregated from each other.

Most descriptions of intracortical connectivity in the barrel cortex indicate that septal projections extend over relatively long horizontal distances. Conversely, analysis of individual pyramidal neurons in layer II/III of a barrel column indicate that the axons of these neurons rarely extend further than the neighboring barrel column (Feldmeyer *et al.* [2006]; Petersen *et al.* [2003]).

Subsequently, the barrel cortex projects to multiple cortical areas including primary motor (M1) cortex, the secondary somatosensory (S2) cortex, the parietal ventral region, and the contralateral barrel cortex (Fabri & Burton [1991]; Hoeflinger *et al.* [1995]; Welker *et al.* [1988]; White & DeAmicis [1977]). The barrel cortex is also linked to subcortical motor regions such as the neostriatum, pons, and superior colliculus (Alloway *et al.* [1999]; Brown *et al.* [1998]; Crandall *et al.* [1986]; Hoffer *et al.* [2005]; Mercier *et al.* [1990]; Mihailoff *et al.* [1985]; Welker *et al.* [1988]), as well as to the brainstem and thalamic nuclei in the lemniscal and paralemniscal pathways (Bourassa *et al.* [1995]; Chmielowska *et al.* [1989]; Hoogland *et al.* [1987]; Killackey & Sherman [2003]; Veinante *et al.* [2000]).

Septa-related projection systems terminate in brain regions that are associated

with the motor system; on the contrary, there are no specific projection system that originate exclusively from the barrel columns. Callosal projections from S1 barrel cortex originate exclusively from the septal circuits (Hayama & Ogawa [1997]; Olavarria *et al.* [1984]): this suggests that septal columns have a role in the bilateral coordination of the whiskers.

The VPm and the POm are strongly influenced by the level of cortical activity, both receiving strong cortico-thalamic input: VPm from layer VI and POm from layer V and VI (Diamond *et al.* [1992]; Kublik *et al.* [2003]; Temereanca & Simons [2004]; Yuan *et al.* [1985, 1986]). The reciprocal connections within cortico-thalamo-cortical systems were proposed to underlie gate/gain mechanisms at the early stage of sensory pathways and during contextual facilitation (Lindström & Wróbel [1990]; Wróbel *et al.* [1998]). In all sensory systems that have been examined, cortico-thalamic projections from layer Vb represent a feedforward pathway to higher order thalamo-cortical circuits (Guillery [1995]; Sherman & Guillery [2002]). Given that cortico-thalamic projections from layer Vb of the barrel cortex terminate exclusively in nucleus POm, the paralemniscal projections from POm to the septa must represent a higher order thalamo-cortical circuit (Killackey & Sherman [2003]).

The lemniscal pathway has a precise topographic organization that maintains the spatial relationships for neighboring whisker representations. Consistent with the columnar organization that is ubiquitous throughout neocortex (Mountcastle [1997]), extragranular neurons located directly above or below a barrel in layer IV are activated best by the same whisker that excites the neurons in the barrel (Simons [1978]; Welker [1971, 1976]). Because of this one-to-one correspondence, a large body of research on the barrel cortex has focused on the circuit mechanisms by which 'principal' and 'surrounding' whiskers influence the neurons in a barrel column (Armstrong-James & Fox [1987]; Brumberg *et al.* [1996]; Kwegyir-Afful *et al.* [2005]; Lavallée & Deschênes [2004]; Simons [1985]). Furthermore, the vast majority of VPM neurons in the same barreloid converge on the corresponding layer IV barrel (Arnold *et al.* [2001]; Land *et al.* [1995]; Lu & Lin [1993]). This excitatory input, along with strong activation of a local inhibitory network in each barrel (Kyriazi *et al.* [1996]; Miller *et al.* [2001]; Pinto *et al.* [2003]; Swadlow *et al.* [1998]), sharpens the receptive fields of barrel neurons so that they are dominated

by a single, principal whisker (Keller [1995]).

Compared with the lemniscal system, POm and its cortical targets do not encode spatial information very precisely. Moreover, the responses of septal neurons to single-whisker stimulation are much smaller than those evoked in the barrel neurons by a principal whisker (Armstrong-James & Fox [1987]; Brecht & Sakmann [2002]; Melzer *et al.* [2006]) and the precise time of whisker stimulation is not encoded, generating variable response latencies ranging from 11 to 25 ms. The timing of neuronal responses in the paralemniscal system is strongly influenced by a set of recurrent dynamic interactions that become evident during repeated whisker stimulation. Given that cortico-thalamic feedback alters POm responsiveness (Diamond *et al.* [1992]), shifts in POm response latency during repeated whisker stimulation reflect an interaction between ascending paralemniscal inputs and descending cortico-thalamic feedback. This view, known as the phase-locked loop hypothesis (Ahissar [1998]), suggests that neuronal oscillators in the barrel cortex determine the specific timing of the excitatory cortico-thalamic feedback to the POm.

Interlaminar connections that are vertically aligned with the barrels or the septa are likely to mediate parallel processing of somatosensory signals that represent the intracortical continuations of the subcortical lemniscal and paralemniscal systems respectively (Shepherd *et al.* [2005]). Whereas the barrel-related circuits process spatiotemporal information generated by whisker contact with external objects, the septa-related circuits encode the frequency and other kinetic features of active whisker movements. The projection patterns from the barrel cortex indicate that information processed by the septa-related circuits is used both separately and in combination with information coming from the barrel-related circuits, in order to mediate specific functions. According to this theory, outputs from the septal processing stream modulate the brain regions that regulate whisking behavior, whereas both processing streams cooperate with each other to identify external stimuli, encountered by passive or active whisker movements. When examined from a system-level perspective, the septa and their connected circuits encode the kinetics of whisker movements and send this information to brain regions that regulate whisking behavior (projections to M1 cortex and other regions that regulate motor activity). By contrast, the barrels and their con-

nected circuits process spatiotemporal information that encodes whisker contact with external objects. Regular-spiking barrel neurons, which are presumed excitatory, respond preferentially to specific directions of whisker deflection (Bruno & Simons [2002]; Bruno *et al.* [2003]; Simons & Carvell [1989]); these spatial properties could facilitate the identification of orientation, shape, distance and other spatial features that rats discriminate with their whiskers (Hayama & Ogawa [1997]; Krupa *et al.* [2001]; Shuler *et al.* [2002]). Nonetheless, the information processed by both circuits must be integrated to mediate object recognition and other related behavioral tasks, i.e., the information obtained by the septal circuits about whisker kinetics must be integrated with the spatiotemporal responses of the barrel-related circuits. This integration is possible at several sites in the barrel cortex and other somatosensory cortical areas. For example, interconnections are present where the barrel and septal compartments adjoin each other in layer IV (Kim & Ebner [1999]). In addition, septal neurons project to supragranular sites overlying the barrel compartments and, thereby, provide another substrate for integration (Shepherd *et al.* [2005]). Furthermore, the nucleus POm projects to layer Va in both the barrel and septal columns (Lu & Lin [1993]). Finally, both the septal and barrel circuits project to S2 cortex (Chakrabarti & Alloway [2006]).

3.3 Whisker Follicle Innervation

Whiskers are an important tactile sense organ for rodents in the same way as hands are an important sense organ for humans and other primates. In total, the muzzle on each side of the face contains approximately $165 \div 210$ whiskers (depending on the species and strain of the animal), which correspond to the same number of barrels in each hemisphere of the cortex. Whereas whiskers in the same arc have similar lengths, those in the same row have graded lengths along the anterior-posterior axis, which leads to different resonant properties of the hairs during whisking. This could help rodents in discriminating the spatial localization of external objects.

The sensory innervation of each whisker follicle is quite high, reflecting the importance of the information transmitted. In rats, each of the larger follicles

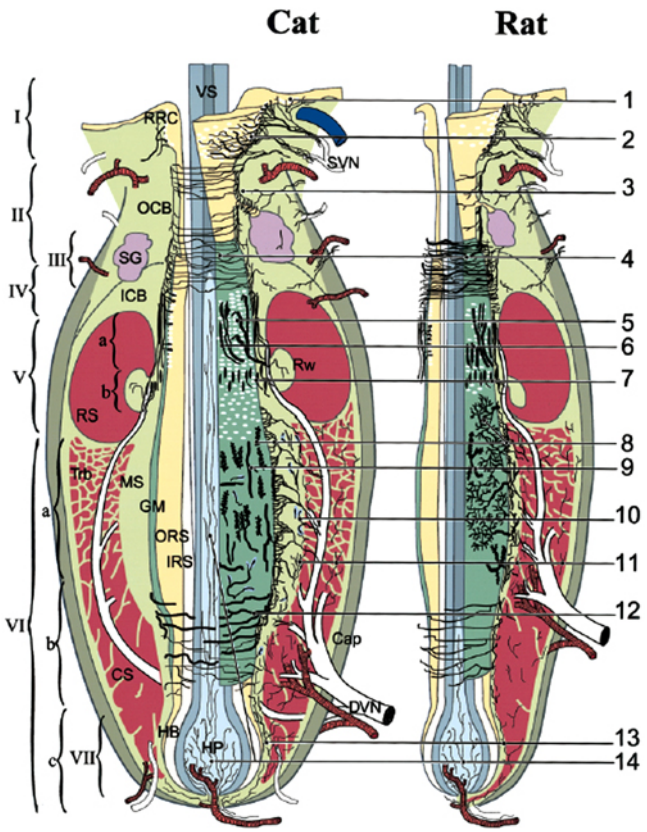

Figure 3.4: Schematic drawing of the structure and innervation of the vibrissa follicle-sinus complex (FSC) in the cat and the rat, from Ebara *et al.* [2002].

receives terminations from approximately 200 trigeminal ganglion cells and the smaller follicles closer to 50. Rat also "whisk" their whiskers, that is, they move their whiskers back and forth rhythmically to sample the space around them. This active tactile behavior is analogous to palpating a surface with the fingers, where the tips of the fingers are rhythmically brought into contact with and retracted from the surface being explored. At rest, rats whisk at a very typical frequency of 7 Hz (Woolsey *et al.* [1975]). Moreover, the frequency of whisker passive stimulation regulates the cortical extent of single-whisker responses, with higher frequency stimulation giving rise to more focused cortical activity (Moore [2004]). For example, a spreading response can be evoked by single-whisker deflections with long inter stimulus intervals of many seconds, whereas localized intrinsic signals are evoked by repetitive trains of 10 Hz stimuli each lasting only

few seconds.

The structure that anchors a whisker to the skin is called follicle: it gives tactile sensitivity and motion to the whisker, which is itself inert material. Deflection of a whisker is thought to open mechano-gated ion channels in nerve endings of sensory neurons innervating the hair follicle, by means of a molecular signaling pathway that is not already fully identified.

Vibrissal follicle-sinus complexes (FSCs) are fundamental and exceptionally well innervated tactile organs on the mystacial pads of most mammals (Andres [1966]; Dehnhardt *et al.* [1999]; Dörfl [1985]; Ebara *et al.* [1992]; Halata & Munger [1980]; Loo & Halata [1991]; Marotte *et al.* [1992]; Mosconi *et al.* [1993]; Rice *et al.* [1986]; Stephens *et al.* [1973]; Van Horn [1970]; Yohro [1977]). Each mammalian species that has whiskers have characteristic vibrissa-related physiology and perception, presumably designed for the different behavioral demands of each species. Specifically studying the rat whisker innervation may provide a means to develop better strategies for understanding peripheral sensory mechanisms and their contribution to the overall somatosensory perception and coding.

The Rat FSC is composed of a vibrissa and its follicle encased within a dermally derived blood sinus, enclosed by a dense collagenous capsule. The inner surface of the sinus is a mesenchymal sheath that lines the thick basement membrane of the follicle. The follicle is composed of an outer layer of cells, against the basement, and an inner core of cells, surrounding the vibrissa. Each FSC has several anatomical specializations at different levels along its longitudinal axis. The follicle becomes thicker from the upper level of the ring sinus to the middle level of the cavernous sinus. The follicle is soft at the lower level of the cavernous sinus and gradually becomes more rigid toward and through the level of the ring sinus. Correspondingly, the basement membrane thickens between the outer layer and the mesenchymal sheath and it is referred to as the glassy membrane. In the lower part of the ring sinus, the mesenchymal sheath has a doughnut-like ringwulst attached around its circumference.

Two sensory nerves innervate the follicle: these are known as the superficial vibrissa nerve (SVN) and the deep vibrissal nerve (DVN). In the rat, approximately five-sixths of the axons from a single follicle are derived from the DVN and one-sixth from the SVN. Each whisker follicle has its own unique DVN and

SVN, i.e. axons within these nerves do not branch to innervate more than one follicle (Zucker & Welker [1969]). Several small superficial vibrissal nerves SVNs penetrate at the level of the follicular outer layer and supply innervation from the rete ridge collar to the inner conical body, in an area located at the top of the follicle. A single, relatively large, deep vibrissal nerve DVN penetrates at about the middle level of the cavernous sinus and supplies innervation from the level of the ring sinus to the cavernous sinus, with a relatively minor contribution to the inner body.

The FSCs nerve fibers can be subdivided into four groups: large-, medium-, small- and fine-caliber fibers. The large-, the medium- and part of the small-caliber fibers are well myelinated, whereas nearly all the fine-caliber fibers showed a varicose appearance and are presumably unmyelinated. Numerous small- and fine-caliber fibers penetrate the base of the FSC and supply the bulb and papilla of the vibrissal follicle.

Each follicle is innervated by the peripheral branches of about 200 cells of the trigeminal ganglion, whose nerve endings convert mechanical energy into action potentials. Receptor endings in the vibrissae follicles can be classified into two broad types: slowly adapting (SA), e.g., Merkel's discs, and rapidly adapting (RA), e.g., lanceolate endings. In addition, a number of free nerve endings surround the follicle, including reticular endings.

Merkel endings are slowly adapting, low-threshold mechanoreceptors. Regular discharge properties categorized as slowly adapting type I and an irregular discharge property categorized as sinus type I were discriminated in the rat FSCs (Gibson & Welker [1983a,b]; Gottschaldt & Vahle-Hinz [1981]; Gottschaldt *et al.* [1973]). Merkel innervation is limited to the caudal half of the rete ridge collar: it could be thus hypothesized that this innervation as a group may be limited for detecting more caudal vibrissae deflections in rats.

Longitudinal lanceolate endings have a sparse and widespread distribution: this suggests that the lanceolate innervation may be a relative diffuse system in the rat. Rat FCSs have en passant, circumferentially oriented lanceolate endings, observed in the inner conical body (Andres [1966]; Mosconi *et al.* [1993]; Rice *et al.* [1986]). These endings appear to be present especially in species that rhythmically whisk their vibrissae (Rice *et al.* [1986]).

Reticular endings are branched in a plane parallel to the glassy membrane and the endings from different afferent fibers are highly interdigitated. The reticular endings and spiny endings are in slightly different planes because only the reticular endings are in intimate contact with the glassy membrane. Gottschaldt *et al.* [1973] hypothesized that reticular endings may function as slowly adapting, low-threshold sinus type II mechanoreceptors that have highly regular firing patterns. However, the wide range of morphologies would suggest that they may have a variety of response properties more like that described as a continuum by Gibson & Welker [1983a,b].

The unbranched club-like endings are located in the mesenchymal sheath precisely at the level where the ringwulst is attached. The highly specific location of these club-like endings strongly indicates that the ringwulst is involved in some specific aspect of sensory transduction. As was hypothesized previously (Rice *et al.* [1986]), the ringwulst and its associated innervation may be involved in detecting the acceleration of vibrissae deflections by harnessing its movement floating in the ring sinus, much like a balancing toy. With their simple morphology, these ringwulst endings would seem to be an optimal candidate for the slowly adapting, sinus type II fibers that have highly regular discharge properties (Gottschaldt *et al.* [1973]).

The infraorbital nerve, whose peripheral endings divide into fascicles each supplying one row of vibrissae, carries axons from the vibrissae follicle receptors to the trigeminal ganglion. Here, the nerve merges with the motor and mandibular branches of the fifth cranial nerve. The axons then exit the ganglion within the fifth nerve to innervate the brainstem nuclei.

3.4 Trigeminal Ganglion

The trigeminal ganglion is a sensory ganglion of the trigeminal nerve that lies in a cavity in the dura mater on the base of the skull, i.e. the fifth cranial nerve responsible for sensation in the face and certain motor functions such as biting or chewing. The name trigeminal comes from “tri-” or three, and “-geminus” or twin, and derives from the fact that each trigeminal nerve has three major branches: the ophthalmic (V1), the maxillary (V2) and the mandibular (V3) nerve.

The greatest possibility of encountering vibrissae-responsive cells in the trigeminal ganglion lies within an area of ∼2 mm wide in the antero-posterior axis, ∼1.25 mm in the medio-lateral axis and for <1.85 mm from dorsal to ventral through the ganglion. A somatotopic organization within the trigeminal ganglion that resemble that one in the vibrissae-responsive region is found: a trend can be seen for the dorsal to ventral organization and the medial to lateral separation of the cells associated with the ophthalmic or maxillary branches of the trigeminal nerve (Leiser & Moxon [2006]).

The first major organizational trend found in the trigeminal ganglion was that the somatotopic organization of cells within this structure along the medio-lateral and antero-posterior axes was consistent with the relative position of their axons within the trigeminal nerve (Leiser & Moxon [2006]). Cells with axons that are within the mandibular branch of the trigeminal nerve (V3-lower jaw) were situated more postero-laterally than the cells with axons that are within either the ophthalmic (V1-eye region) or maxillary (V2-nose, upper jaw, whiskers) branches. Therefore, cells innervating the more dorsal facial features (i.e., the eye, V1) were encountered more dorsally, whereas the cells innervating the ventral facial features (i.e., the lower lip, V3) were found more ventrally, and cells innervating the midline facial features (i.e., the nose, whiskers, and upper lip, V2) were found in between. This dorsal to ventral somatotopy observed throughout the trigeminal ganglion was consistent with the dorsal to ventral position of the trigeminal nerves innervating the ganglion.

The second major organizational trend was that, passing through the ganglion from the dorsal region to the ventral one, cells innervating the dorsal facial features (V1) are encountered first, followed by midline features (V2) and finally ventral facial features (V3). Moreover, a distinct medial-lateral separation can be found between cells whose axons lies in the mandibular branch and cells whose axons lies in the ophthalmic or maxillary branches. This separation is clear also in the anterior-posterior axis.

In the vibrissae-responsive region of the trigeminal ganglion, there is no significant difference in the locations of cells along any axis when they were grouped by whisker columns, but there are significant differences when cells were grouped by rows (Leiser & Moxon [2006]). Only a weak somatotopic organization for the

whisker columns may exist along the anteroposterior or dorso-ventral axis within the ganglion, while there is a significant difference in the ventral locations of the cells grouped by whisker rows. Cells responding to the most dorsal whiskers (rows A and B) were significantly more dorsal than cells responding to the most ventral whiskers (rows D and E). The dorsoventral somatotopy within the whisker pad is thus maintained within the vibrissae-responsive region of the trigeminal ganglion.

More cells respond to larger, caudal whiskers than the smaller rostral whiskers: there are significantly more cells with caudal whisker receptive fields (RFs) than cells with rostral whisker RFs. This is in agreement with the innervation, where there are no differences in the number of axons innervating each row, but there are more axons innervating the caudal whiskers than the rostral whiskers.

These observations (Leiser & Moxon [2006]) support developmental theories, suggesting that the arrangement of peripheral neurons may be a template for the design of central nuclei of the brainstem: the somatotopic position of cells in the trigeminal ganglion grouped by trigeminal nerve branch is inverted from that found in the principal trigeminal nucleus (PrV). There, cells with RFs that are innervated by the mandibular branch of the trigeminal nerve are situated dorsally, cells with RFs that are innervated by ophthalmic branch are situated ventrally, and, finally, cells with RF that are innervated by the maxillary branch are situated in between. Therefore, it seems that the trigeminal ganglion (that developed first) serves as a model for the organization of central structures, so as the ganglion and brainstem have similar (although inverted) somatotopy.

Neuronal units measured electrophysiologically are classified as Slowly Adapting (SA) if activity to a fast, high-amplitude deflection is sustained for some time (few dozens of ms) from the stimulus onset. Alternatively, in case the neuron is quiescent at this time, it was classified as Rapidly Adapting (RA). From studies on primates, it has been hypothesized that RA and SA type cells serve a distinctly different sensory function: RA cells generally code for object location by detecting low-frequency skin motion while SA cells generally discriminate the object, coding for object form and texture.

In rats, it has been shown through extracellular recordings of trigeminal ganglion cells that SA cells code for whisker position (amplitude) and RA cells code for whisker velocity or acceleration. SA neurons are also known to display occa-

sionally phasic responses to some directions of deflection. Moreover, a correlation between a particular receptive field (whisker column) and a particular physiological response type (RA or SA) is highly probable.

RA and SA cells are equally distributed across both rows and columns, with nearly 60% of the vibrissae-responsive neurons classified as SA, and the remaining 40% as RA (Leiser & Moxon [2006]). Therefore, it is unlikely that any computational differences associated with RA and SA cells can be exclusively associated with either caudal or rostral whiskers. This also suggests that each whisker is represented by a population of cells able to handle and transmit the information encoded by both RA and SA cells. The functional differences of vibrissae, if any, must then be context or behavior dependent.

It has been found (Stüttgen *et al.* [2006]) that a stimulus amplitude of about 3° divides detectability into two qualitatively different modes. Small stimuli (<3°) are detected only at high peak velocities (∼750°/s), whereas large stimuli (>3°) are detected at substantially lower peak velocities (∼125°/s). Therefore, velocity thresholds for detection of small amplitude stimuli are considerably higher than for detection of large-amplitude stimuli (Stüttgen *et al.* [2006]). This finding suggests the existence of two psychophysical channels mediating detection of whisker deflection: one channel exhibiting high amplitude and low velocity thresholds (W1), and the other exhibiting high velocity and low amplitude thresholds (W2). The correspondence of W1 to slowly adapting (SA) and W2 to rapidly adapting (RA) neuronal classes in the trigeminal ganglion has already been revealed in acute neurophysiological experiments (Shoykhet *et al.* [2000]).

Although amplitude of whisker deflection determines detectability at medium velocities, it seems insufficient for detection when peak velocity is low (e.g. <250°/s) and irrelevant when peak velocity is high (e.g. 1500°/s) (Stüttgen *et al.* [2006]). Moreover, it appeared that RA cells code for peak velocity but do not reflect peak acceleration. Therefore, it is likely that velocity rather than peak acceleration determines the spike counts of RA and SA that are related closest to the detectability of whisker deflection.

The evidence that these separable neuronal responses underpin the two different channels opens the possibility to address the question of coding of kinematic parameters by looking at the neurometric features of each class of primary affer-

ents. The closest match between psychometric and neurometric curves is achieved only if transient, rather than sustained portions, of SA responses are considered. This implies that those central instances of the somatosensory system that give rise to the animals' perception may not receive or use the tonic portion of SA response. On that way, it has also been found that SA encode dynamic kinematic parameters at a high temporal precision.

In many natural contexts, the availability of sensory stimuli is short and there is pressure to initiate behavioral decisions in a limited time span. Presumably, such constraints have helped to evolve strategies applied by numerous sensory systems to extract relevant temporal information from low numbers of spikes (Rieke [1999]; Stüttgen *et al.* [2006]).

3.5 Thalamus

Most of the various sensory pathways described below relay impulses from sense organs via three or four-neuron chains to particular regions of the cerebral cortex: these impulses are responsible for perception and localization of individual sensations coming from the whiskers of the rat.

The thalamus is a large collection of neuronal groups within the brains of vertebrates, situated between the cerebral cortex and the midbrain; it participates in sensory, motor, and limbic functions (regulation of consciousness, sleep and alertness). Virtually all information that reaches the cortex is being processed by the thalamus, leading to its being called the gateway to the cerebral cortex. The mechanism by which the cortex processes an afferent signal is inextricably linked with, and in fact determines, the saliency of neural codes embedded in the thalamic response.

The thalamus can be divided into nuclei that project diffusely to wide regions of the neocortex and nuclei that project to specific discrete portions of the neocortex and limbic system. Most of the cells of the thalamic nuclei are excitatory neurons that release glutamate. The thalamus also contains inhibitory neurons in the thalamic reticular nucleus: these neurons release GABA and their axons do not project to the cortex. Rather, they are thalamic interneurons that modulate the responses of other thalamic neurons to inputs coming from the cortex.

Receptive fields of neurons in thalamic barreloids and cortical barrels are such that both sets of neurons respond robustly to the same types of stimuli, allowing for a straightforward comparison of response properties. Neither amplitude nor velocity, however, affect thalamic response magnitude to the same extent as velocity does in the cortex. Because thalamic barreloid neurons provide the major source of afferent input to the cortical barrels, the neuronal code in the thalamus that best represents deflection velocity is likely to be the one to which the cortical circuit is more sensitive.

Thalamic neurons respond to their principal whisker with latencies ranging between 4 and 6 ms. In contrast, responses of the same thalamic cells to their surround receptive field components are far more variable, between 7 to 15 ms (Armstrong-James & Callahan [1991]). As the cortical cells are driven by the temporal summation of the thalamic input, the principal whisker response tends to be selected from the background of surround whisker responses. Therefore, it is a mechanism based on temporal selection.

The temporal contrast, more specifically the average firing rate within 2-7 ms from the onset of the thalamic activity, best predicts the cortical response (Pinto *et al.* [2000]): the barrel circuitry is more sensitive to the level of initial synchrony in the thalamic input than to the total input spike count. Therefore, the barrel circuitry transforms a temporally based thalamic code into a new one based on the response magnitude.

Chapter 4

Materials & Methods

4.1 Surgical Procedures

Wistar rats were maintained in the Animal Research Facility of the Department of Biomedical Sciences (University of Padova, Italy) under standard environmental conditions. The University of Padova Ethical Committee approved all animal procedures. For all the experiments, P30-P50 rats were anesthetized with a mixture of tiletamine (2 mg/100 g weight) and xylazine (1.4 g/100 g weight) or urethane (0.15 g/100 g weight). The anesthesia level was monitored throughout the experiment by testing eye and hind-limb reflexes, respiration and checking the absence of whiskers' spontaneous movements. In the case of the first type of anesthesia additional doses of tiletamine (0.5 mg/100 g weight) and xylazine (0.5 g/100 g weight) were provided every hour or whenever necessary. During the surgery and the recording section, animals were kept on a common stereotaxic frame, fixed by teeth and ear bars and observed with a stereomicroscope (Nikon SMZ800, Nikon Instruments Inc., Melville, NY, USA) and neon lamps. The body temperature was constantly monitored with a rectal probe and maintained at about 37 °C using a heating pad. The fur of the head of the rat was trimmed and then, to expose the cortical area of interest, anterior-posterior opening in the skin was made along the medial line of the head, starting from the imaginary eyeline and ending at the neck. While the skin was kept apart using halsted-mosquito hemostats forceps, the connective tissue between skin and skull was gently removed by means of a bone scraper. Thus, the skull over the right hemi-sphere was drilled to open a

window in correspondence of the somatosensory cortex, S1 (-1 to -4 AP, +4 to +8 LM) (Swanson [2003]). Meninges were then carefully cut by means of forceps at coordinates (-2.5 AP, +6 LM) to avoid the clogging of the micropipettes tip or the damage of the needle chip in the subsequent insertion. In the experiments where signals from the trigeminal ganglion were collected, a craniotomy was performed to expose the left cerebral hemisphere, which was then gently aspirated to visualize the trigeminal ganglion at the base of the skull. The dura overlying the ganglion was then teased away (Stüttgen *et al.* [2006]).

Small pieces of cotton were rolled, wet and put between the skull and the skin in order to shape a small pool of Krebs solution over the head of the animal, where the reference ground electrode was immersed.

4.2 Solutions

During all the experiments, a physiological solution was used, called Krebs solution. This solution mimics fluids that are normally found in the brain and it was composed by 120 mM of NaCl, 1.99 mM of KCl, 25.56 mM of $NaHCO_3$, 136.09 mM of KH_2PO_4, 2 mM of $CaCl_2$, 1.2 mM of $MgSO_4$ and 11 mM of glucose. Before applying it to the brain, the solution was warmed at 37 °C. The conductivity of the Krebs solution was (14.33 ± 0.01) mS/cm.

4.3 Implantation Procedures

Micropipettes and chips were moved, positioned and inserted in depth in the tissue by means of a Patchstar micromanipulator (Scientifica Ltd, East Sussex, UK) equipped with custom holders. The position of the recording device in the cortical depth was first monitored through the microscope and then, after the impalement, through a dedicated software (Scientifica Linlab Control).

4.4 Vibrissa Stimulation Protocol

At the end of the surgery, contralateral whiskers were trimmed at about 10 mm from the mystacial pad. Single whiskers were deflected repeatedly by rapidly

displacing a 25G hypodermic needle (BD Plastipak, Madrid, Spain) attached by means of a drop of superglue to a multilayer piezoelectric bender with integrated strain gauges (P-871.122, Physik Instrumente, Karlsruhe, Germany). The bender was driven by a power amplifier (E-650.00, Physik Instrumente, Karlsruhe, Germany) connected to a waveform generator (Agilent 33250A 80 MHz, Agilent Technologies Inc., Colorado, USA) through a closed-loop control system (designed and implemented by Prof. Roberto Oboe and his team at the Department of Management and Engineering, University of Padova, Vicenza, Italy) able to monitor the actual movement of the piezoelectric bender by reading its strain gauges values. The bender was driven by providing square stimuli at 1 kHz, triggered by a custom LabView program (www.ni.com/labview/). At every cortical depth, single sweeps were recorded in response to these mechanical stimulations with a temporal delay of 2 seconds between subsequent deflections, in order to avoid any phenomenon related to adaptation.

The effective displacement of the whisker upon stimulation was monitored through a high-speed camera system (FASTCAM Mini UX100, 1280 $\times$ 1024 pixels sensor, 800K fps maximum frame rate, Photron USA Inc., San Diego, CA, USA). The acquired videos were analyzed through a free tool for offline tracking built on the Open Source Physics (OSP) Java Framework (Tracker, https://www.cabrillo.edu/~dbrown/tracker/).

4.5 Micropipettes and Ag/AgCl Electrodes

Micropipettes were pulled from borosilicate glass capillaries GB150T-10 (Science Products, sizes 1.050 $\times$ 1.50 $\times$ 100 mm) through a Flaming/Brown Micropipette Puller (P-97, Sutter Instrument, California, USA). Capillaries were heated and stretched by the puller in a predictable and repeatable way, leading to the formation of two micropipettes with a very narrow tip (diameter of about 1 μm). During the experiments, pipettes were filled with Krebs solution, where the Ag/AgCl electrodes were immersed, and fixed into holders. The resistance of recording pipettes was about 1 MΩ. All the Ag electrodes were chlorinated using a 1 M KCl solution, where electrodes were immersed while a squared pulse between 0 V and 1 V (100 s duration) was applied using a standard function generator (Agilent 33250A).

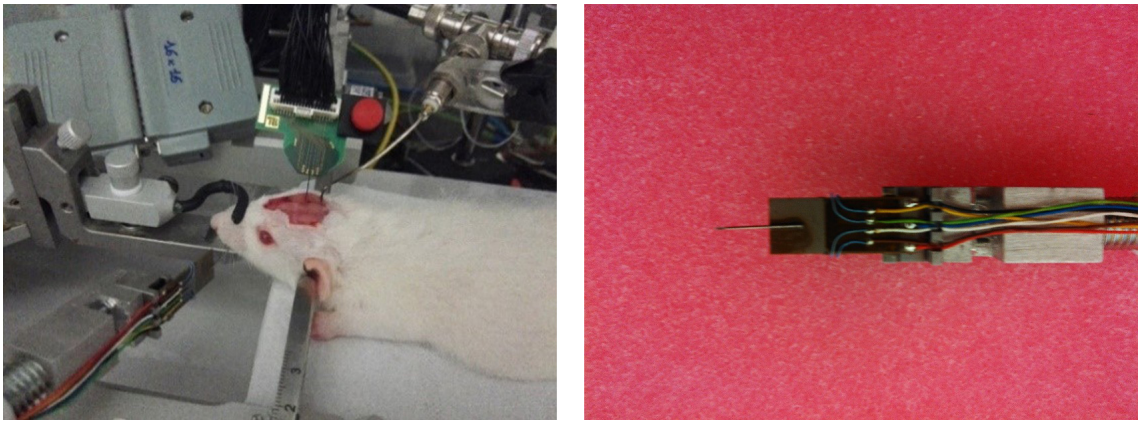

Figure 4.1: (Left) A photo of a typical experiment with the implantable needle chip. (Right) The piezoelectric bender with the hypodermic needle attached for whisker stimulation.

4.6 Grounding

The bath over the brain of the animal was grounded by the use of a massive Ag/AgCl electrode (diameter of about 1 mm) connected to the main ground of the system, in a way that a differential signal can be obtained and the electrical modulation of the bath could be minimized.

4.7 Measurement Setup (Micropipettes)

Signals collected by the recording micropipette electrode were acquired with reference to an Ag/AgCl ground electrode. Both electrodes were connected to an extracellular preamplifier (SEC-EXT headstage, npi Electronic GmbH, Tamm, Germany) having 10x gain and high-pass filter with corner frequency of 1 Hz. The preamplified waveforms were then 10x amplified and low-pass filtered with cutoff frequency of 33 kHz using a SEC-10L amplifier (npi Electronic) operating in bridge mode. Amplified raw signals were high-pass filtered at 1 Hz and low-pass filtered at 3 kHz and digitalized at 50 kHz through a multifunction DAQ system (PCI-6071E I/O card, 12-bit resolution, [-0.5 ÷ 0.5 V] input range and stream-to-disk rate up to 1.25 MS/s, National Instruments Co, Texas, USA) combined

with a BNC-2090 terminal block (National Instruments Co, Texas, USA). They were then visualized, monitored and recorded by a custom LabView program.

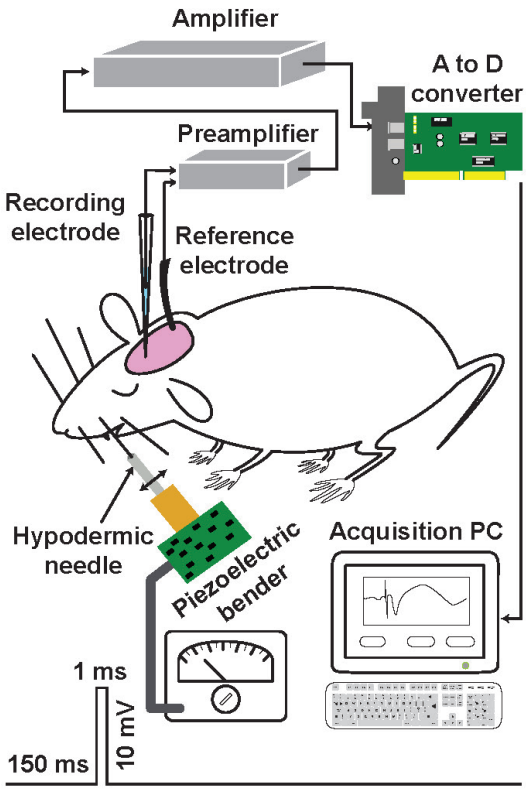

Figure 4.2: Simplified scheme of the stimulation and recording setup.

When recording evoked responses, signals were acquired in sweeps of 500 ms length, with a 2 s intersweep interval between subsequent traces. The trigger that drives the whisker deflection was set at 150 ms from the start of the acquisition. In order to study variability, 500 evoked responses were sampled at each cortical depth.

When recording spontaneous activity, signals were acquired in sweeps of 10 s length, with a 500 ms intersweep interval. At each cortical depth, 50 sweeps were sampled. Obviously, in this case no external stimulus was applied.

4.8 Implantable Multi-electrode Array Needle Chips

The operation principle of these implantable devices was an extended CMOS-based EOSFET (Electrolyte Oxide Semiconductor Field Effect Transistor). The recording sites were arranged in rows and column along the tip of the needle of the chip, in order to obtain spatial resolution. The maximum number of recording sites was set to 256, which can be organized into square (16 $\times$ 16) as well as in rectangular shaped arrays (4 $\times$ 64). The recording electrodes were chosen to be 7.4 μm in diameter size and octagonal in shape. The latter represented a tradeoff between the biological demand, as round shapes fulfill the best coverage ratio (i.e., the portion of the neuronal membrane attached to the recording electrode), and the technological limitations, since round structures cause problems during fabrication. The needle thickness was chosen to be 150 μm, as a compromise between maximum needle robustness and minor tissue damage during insertion. Accordingly to the dimensions of the recording array, the needle is chosen to be 300 μm in width and 10 mm long for all needle chips. The pitch (i.e. the distance between adjacent recording sites) was determined only by the required spatial resolution of the experiments. The selected x- and y-pitch was 15 μm for the 16 $\times$ 16 square arrays and 33 μm for the 4 $\times$ 64 rectangular arrays.

For simultaneous recording from all the recording sites at least 256 interconnects were required, plus some voltage supply interconnects. To reduce the amount of contact pads needed, thus minimizing the huge contact area, a multiplexing approach was used.

Due to the *in-vivo* application of these devices, biostability and biocompatibility of the chip materials were required. A thin layer of TiO_2 (30 nm-thick) was deposited over the silicon surface in a way that the needle chip did not impair the neural tissue and viceversa.

4.8.1 Needle Chip Fabrication

Needle chips were designed and built in collaboration with Prof. Roland Thewes and his fellows at the Electrical Engineering and Computer Science Department

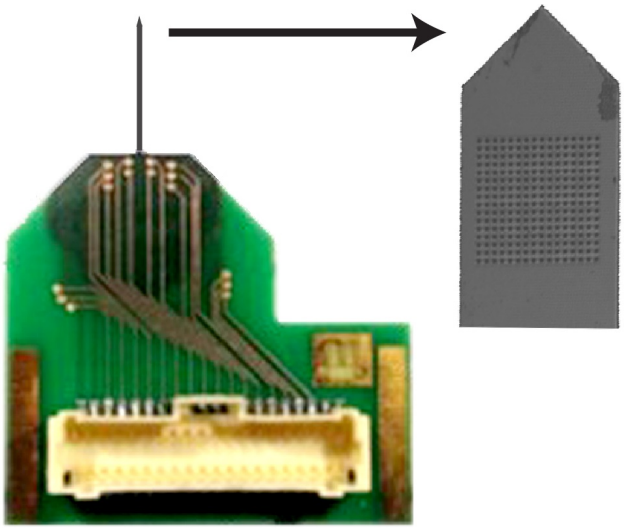

Figure 4.3: (Left) An assembled needle-PCB. (Right) Photomicrograph of the tip of a 16 × 16 needle chip.

of the Technische Universität (TU) in Berlin.

Needle chips are made on the basis of a 180 nm standard CMOS process with six metal layers. After the last intermetal dielectric (IMD) deposition step of the CMOS process covering metal 6, recording electrodes are processed by IHP GmbH, Frankfurt/Oder: a top via hole is etched, filled with W, and a top Ti/TiN electrode with approximately 50 nm thickness is deposited and patterned. The individual needle-shaped sensors were separated through a dicing process, performed in collaboration with another group of the TU-Berlin using an inductive coupled plasma rapid ion etching (ICP-RIE) process. This step enables the etching of SiO_2 and Si through a plasma-assisted process. A homogeneous 30 nm thick layer of TiO_2 is then deposited on all chip surfaces (Ti/TiN electrodes, SiO_2 IMD dielectric, bulk Si) by a 3D ALD deposition process using a SENTECH ALD machine (SENTECH Instruments GmbH, Berlin, Germany).

After processing of the sensor dielectric, each needle chip is assembled to a small PCB. The needle PCB serves as carrier for the needle, enables mechanical handling (e.g., fixing the needle to a custom holder) and represent the electrical interface between the chip and the control unit. The switching unit and dedicated amplification was realized off-chip.

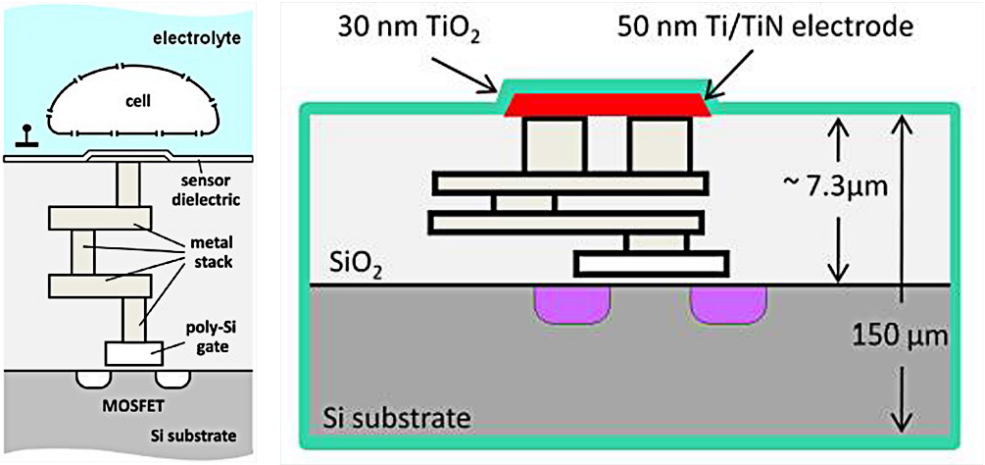

Figure 4.4: (Left) Schematic of needle chip after ALD. (Right) Extension of the EOSFET principle to provide a purely capacitive CMOS compatible neural recording approach. Figures adapted and modified from Eversmann *et al.* [2011]; Schröder *et al.* [2015].

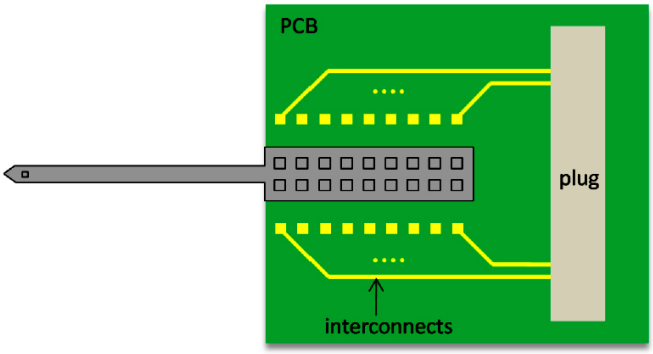

Figure 4.5: Schematic of the needle PCB, assembled with needle chip and plug.

4.9 Measurement Setup (Chip)

A number of external components were required to operate the extended CMOS-based sensor needle: a standard PC, a dedicated National Instruments (NI) measurement and automation hardware, a low-noise power supply and a customized control unit. A simplified block diagram, which illustrates the individual components and the interaction between them, is shown in Figure 4.6.

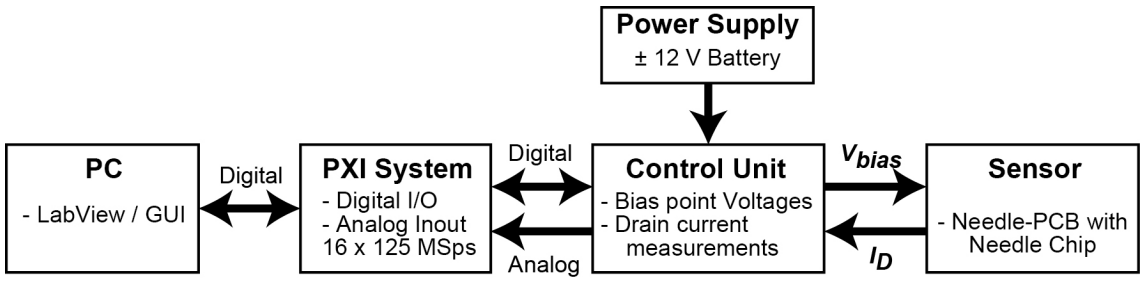

Figure 4.6: General block diagram of the measurement setup for chips, consisting of PC, PXI system, control unit, power supply and the sensor.

The components of control unit and power supply were placed and mechanically fixed in a metal case. Using high-permeability metal (mu-metal or nickel-iron alloy) as case material, the case shielded the internal components from electromagnetic radiation generated by the external environment. Furthermore, the case of the control unit was subdivided by metal walls and equipped with a central ground. Thus, individual PCBs were separated and protected against crosstalk coming from neighboring circuitry, in particular against fast switching digital circuitry.

4.9.1 Control Unit

The electronic circuits for multiplexing, signal processing and bias voltage setting were realized off-chip in the so-called control unit, a customized interface between the assembled needle chip and the NI measurement and automation hardware, supplied by the power supply unit.

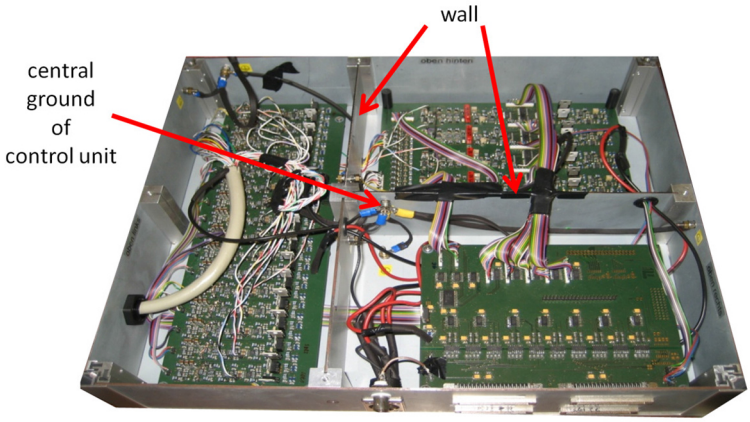

Figure 4.7: The control unit and power supply case.

4.9.2 NI Measurement and Automation Hardware (PXI System)

The interface between the PC and the control unit was a NI PXI-system (National Instruments Co, Texas, USA). This system consisted of a chassis (NI PXIe-1073) which was equipped with the multifunction data acquisition (DAQ) hardware (NI PXIe-6358). The NI PXIe-6358 unit itself provided 16 simultaneously operated differential analog inputs with up to 1.25 MS/s per channel and 16-bit resolution (connected to the 16-channel readout-PCB), four analog outputs (stimulation-PCB), and 48 digital I/O sufficient to operate the control unit. For these needle chips, a multiplexing approach with particular readout technique was chosen. The recording sites were arranged electrically in rows and columns, with each site connected to one particular column and one row. Any combination of column-row existed only once. By connecting this array to a switching unit, each recording site could be selected. Using this approach, the number of interconnects was reduced to 16 row and 16 column interconnects, plus some voltage supplies interconnects. During the switching operation, each recording transistor could achieve two different states: the on-state (recording) and the off-state. By means of an individual switchable voltage on each column, recording sites could be set in on- or off-state column wise. The entire array could be read out by systematically switching one column to the next and so on after a certain time (called column access time,

fixed to 100 μs for all the recordings shown). After the last column of the array was set back to the off-state, one cycle was finished and a new cycle started again from the beginning. Conversely, the recording row-wise was done continuously and contains the measured voltages from the corresponding columns. Finally, from the known column access times it was possible to assign each measured data to the individual recording site and then reconstruct the original signal.

4.10 Software

4.10.1 Multisite Chip Acquisition Program

The PXI-system and the control unit were operated by means of a LabView software. In addition, the LabView program served as graphical user interface (GUI) and enables the selection of measurement parameters. The acquired data were saved on the hard disk as TDMS-files (Technical Data Management Stream, a NI supported file format). Assuming to perform an acquisition from 16 channels, with 1.25 MS/s and 16-Bit resolution, a volume of data equal to 40 Mbyte/s was generated and must be stored simultaneously. Therefore, memory speed of the PC represented a crucial parameter.

All software sided settings of relevant measurement parameters like bias point voltages, array configuration, measurement timing (trigger, column access time, recording time), etc. are freely selectable at the GUI. Important parameters are additionally checked by security queries and automatic scans of setting by means of the acquisition software.

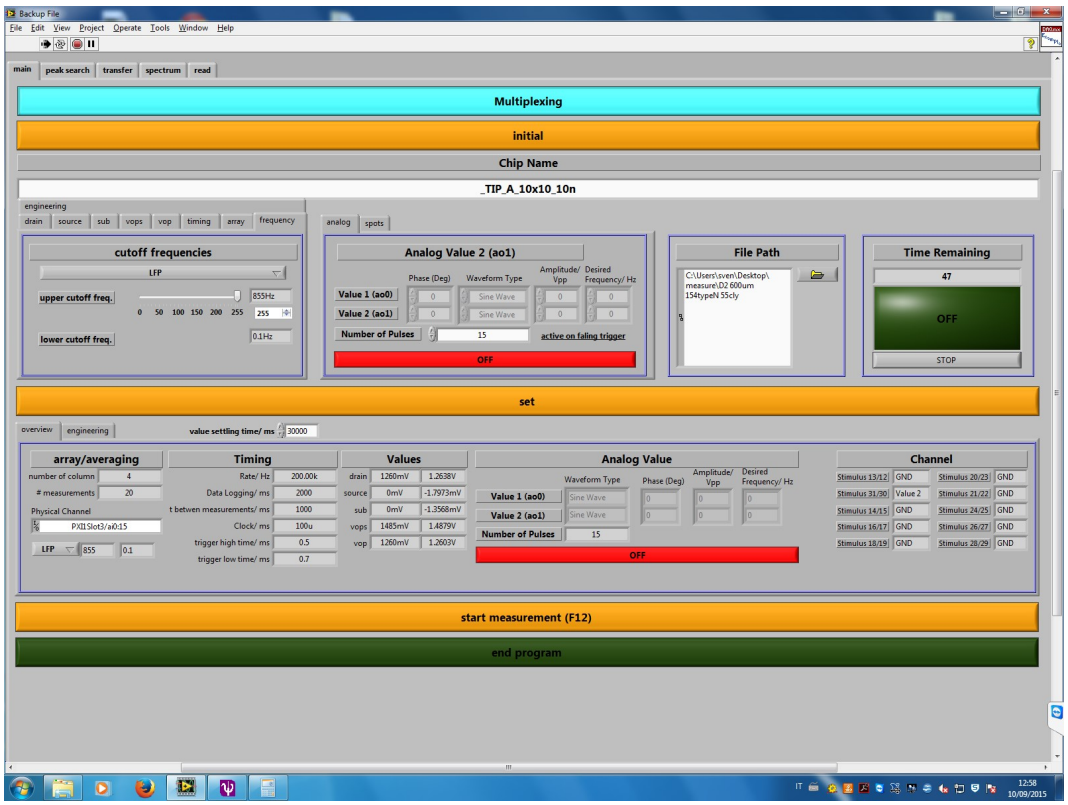

Figure 4.8: A screenshot of the acquisition software.

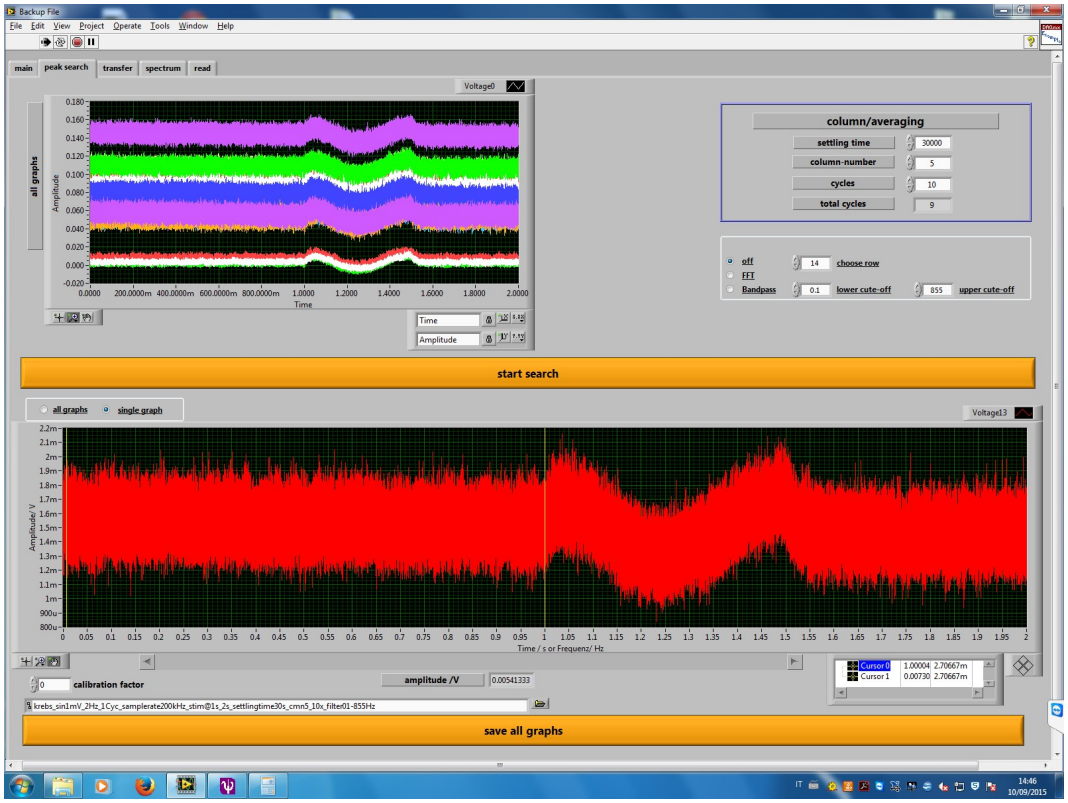

Figure 4.9: Another screenshot of the acquisition software, showing a sinusoidal calibration signal of 1 mV.

4.10.2 Signal Processing of Multisite Acquisitions

Raw signals from different recording sites, saved as multiplexed tdms-files, were demultiplexed by a custom-made MATLAB (R2015a, Mathworks Inc., Natick, USA) software, and rearranged data were spatially smoothed with a two-pass three-point hamming filter (Mahmud *et al.* [2011]):

Pass 1: $j'(z) = 0.23 \cdot j(z-1) + 0.54 \cdot j(z) + 0.23 \cdot j(z+1)$

Pass 2: $j''(z) = 0.23 \cdot j'(z-1) + 0.54 \cdot j'(z) + 0.23 \cdot j'(z+1)$

where j is the raw signal, j' is the first pass smoothed signal and j'' is the final smoothed signal.

The smoothed signals were then visualized in 2D and 3D plots using custom scripts written in MATLAB (R2015a).

4.10.3 Evoked Response Analysis

The algorithms for the analysis were implemented in MATLAB (R2015b, Mathworks Inc., Natick, USA) under Windows 8.1 environment (Microsoft Inc., Redmond, USA) in collaboration with Dr. Mufti Mahmud (Neurochip Lab, Department of Biomedical Sciences, University of Padova) and Dr. Maria Rubega (Prof. Sparacino Group, Department of Information Engineering, University of Padova, see Rubega *et al.* [2015]).

The software was designed with a multi-layered software engineering approach. In this type of client-server architecture user interface, functional process logic ("business logic"), and data storage & access are built as distinct modules to promote software modularity allowing any of the layers to be upgraded or replaced independently with changing requirements (Eckerson [1995]; Mahmud *et al.* [2012a]).

In this application, three layers were designed, as following:

- User interface layer (top layer): this contained user interfaces which, upon receiving user commands, communicated with the middle layer for their execution.
- Application layer (middle layer): the detailed processing and analysis algorithms were implemented in this layer. It was made capable of data exchange and communication with the other two layers.
- Data layer (bottom layer): data security, performance and databases (i.e., storages) were kept as a separate layer in order to improve the software scalability.

The first step of signal elaboration was the removal of stimulation artifacts. The artifact removal algorithm was divided into two main subfunctions (Mahmud *et al.* [2012b]): Artifact Detection (AD), and Artifact Removal (AR). The AD subfunction scanned each signal for occurrence of artifacts and if found, marked the probable end of the detected artifacts. The AR subfunction calculated the artifacts' exact starting and ending points, removed the artifacts and interpolated the artifact region. Once the artifact was removed, the clean signal was stored for further processing and analysis (Figure 4.10).

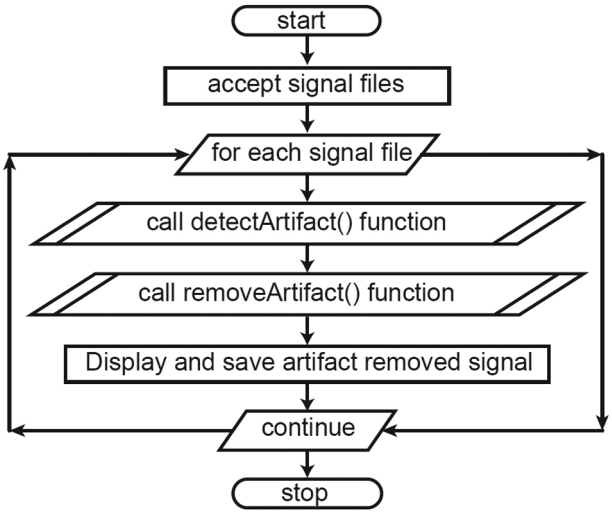

Figure 4.10: Flowchart of the artifact removal method.

The Artifact Detection (AD) subfunction provided with the number of artifacts present in a single trial LFP signal and marked the probable end of the artifacts' which was then sent to the next module for removal. To detect an artifact each data point of the signal starting from the stimulus-onset was checked for threshold crossing and its direction with respect to the previous data-point (up or down). When the signal for a pair of threshold crossing data points with same directions was detected, the second point in the pair was considered as a probable end of an artifact. The pseudocode is listed in Algorithm 1 (Figure 4.11).

Once the information on the number of artifacts and their probable endpoints were determined, the Artifact Removal module was implemented to determine the exact start and end of those artifacts. The probable endpoint received from the AD subfunction was taken as reference to compute the exact area covered by the artifacts. The signal was then scanned backwards from the reference point and the local minima was computed. Starting from the detected local minima, the starting point of the artifact was taken as the one whose derivative approached zero. For the exact end of the artifact, it was sufficient to detect the nearest point in value to the starting point. Briefly, to calculate the end point: from the reference point the signal was scanned forward, the difference in derivative between the starting point and current point was calculated, and the process continued until this difference

Algorithm 1 Artifact Detection (AD) algorithm

```
1:  procedure detectArtifacts(SIGNAL AS data)
2:      Calculate nDP:=length(data);
3:      Calculate thr:=σ(data);
4:      Initialize flagUp:=0, flagDown:=1;
5:      Initialize n:=0, timestamp:=[], dataStamp:=[];
6:      for cDP = 1 to nDP do
7:          if data(cDP) ≥ thr and flagUp then
8:              flagUp:=1, flagDown:=0;
9:          else if data(cDP) ≤ thr and flagDown then
10:             flagUp:=0, flagDown:=1, n:=n+1;
11:             timeStamp(n):=time(cDP);
12:             dataStamp(n):=data(cDP);
13:         end if
14:         if flagUp then
15:             n:=n+1;
16:         end if
17:     end for
18: return n, timeStamp, dataStamp;
19: end procedure
```

Figure 4.11: The Artifact Detection algorithm.

crosses a predefined error value (defined as 10% of the signal standard deviation). Once the starting and ending points were detected, interpolation between them was performed, and the artifact area was replaced with the interpolated points Mahmud *et al.* [2012c]. The pseudocode is listed in Algorithm 2 (Figure 4.12).

Evoked responses from the barrel cortex follow a specific laminar morphology, which has been reported earlier (Ahrens & Kleinfeld [2004]; Kublik [2004]). Usually in upper cortical layers (I, II) the response rarely have a small positive peak (SP) followed by the main negative peak, i.e., the response peak (RP) and then a positive rebound (PR). In the mid-layers (III, IV, and V) the SP disappears and the signals start with the RP followed by the PR. In deep cortical layers (VI), the main RP becomes smaller and usually gets divided into two smaller negative peaks followed by the PR. These features of the signals can be exploited to automatically detect the evoked responses in the recorded signals. Thus, the evoked responses are identified through three important features that they exhibit: the start of the response (response-onset or Feature 1), the Response Peak (RP) (Feature 2), and the Positive Rebound (PR) (Feature 3) (Figure 4.13).

Figure 4.13 shows an annotated example of a single trial LFP response recorded from layer IV (720 μm) where the features are highlighted (adapted from Cecchetto *et al.* [2015]).

Algorithm 2 Artifact Removal (AR) algorithm

procedure *removeArtifacts*(SIGNAL AS *data*, TIME AS *t*, *n*, *dataStamp*)
  Initialize *artifactOnset*:=*stimulusOnset*;
  Initialize *artRemovedSignal*:=*data*;
  for $i = 1$ to n **do**
    refPoint:=*dataStamp*(*i*);
    localMinima:=*min*(from *refPoint* to *artifactOnset*);
    startingPoint:= the first point where the signal derivative approaches zero, starting from *localMinima* and going backwards;
    startingTime(*i*):=*t*(*startingPoint*);
    endingPoint:=from *refPoint* going forward until the derivative difference between the current point and *startingPoint* approaches zero;
    endingTime(*i*):=*t*(*endingPoint*);
    artifactPart:=*data*(*startingPoint* : *endingPoint*);
    artRemovedSignal:=*data*(1 : *startingPoint*) + *interpolation*(*artifactPart*(1 : *end*)) + *data*(*endingPoint* : *end*);
    data:=*artRemovedSignal*;
  end for
  Save and display *artRemovedSignal*;
return *artRemovedSignal*, *startingTime*, *endingTime*;
end procedure

Figure 4.12: The Artifact Removal algorithm.

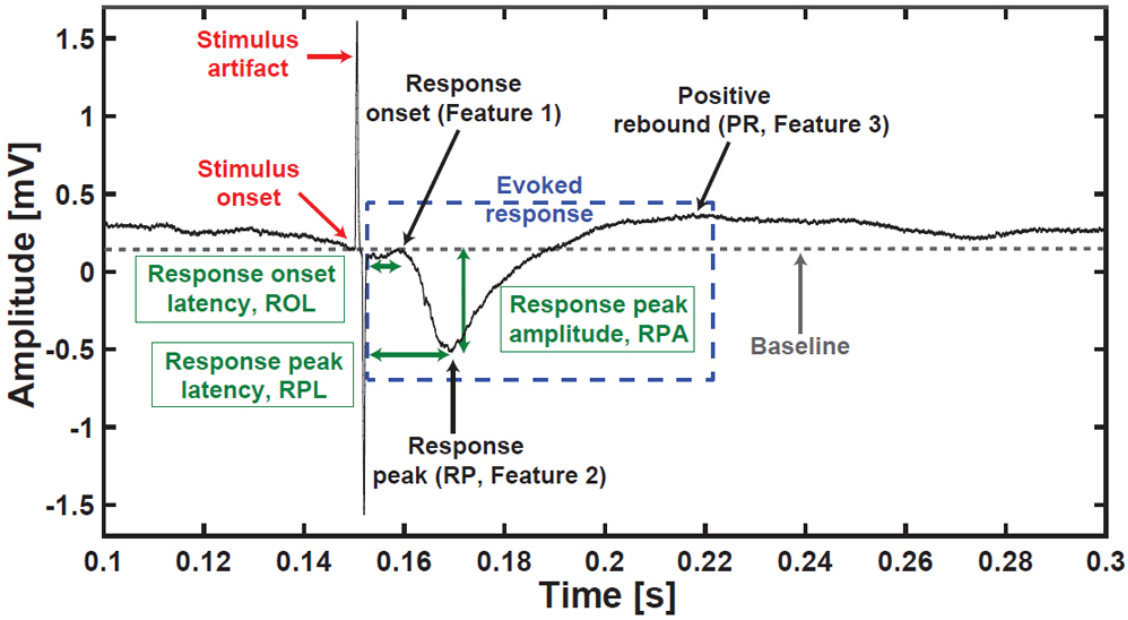

Figure 4.13: Representative single trial LFP with relevant features and parameters. The grey straight line indicates the baseline.

It should be noted that in cases where the SP was detected, the response onset or Feature 1 was considered as the maxima of SP. In the remaining text, the terms Feature 1 and response-onset are used interchangeably. It has been reported earlier (Mahmud *et al.* [2011]) that three vital parameters are sufficient to characterize the evoked responses: response onset latency (ROL), response peak latency (RPL), and response peak amplitude (RPA). However, to be able to compute these parameters precisely, accurate detection of the features that define the evoked response is needed.

A custom algorithm was developed for the detection of those features in evoked responses (see 4.14 for Algorithm 3, Mahmud *et al.* [2016]).

Algorithm 3 Feature Detection algorithm

```
1: procedure detectFeatures(SIGNAL AS data, TIME AS t)
2:     Initialize cutoffFreq:=250 Hz;
3:     filteredSignal:=butterworthLowpassFilter(data,
   cutoffFreq);
4:     Initialize stimOnset,T_end;
5:     Translate data with stimOnset:=0;
6:     Calculate sigDeriv:=calculateSecondDerivative(data);
7:     respOnset:=data(corresponding point where sigDeriv changes
   sharply in first 50 ms);
8:     Translate data with respOnset:=0;
9:     Initialize tData:=data(first 50 ms from respOnset);
10:    Calculate sigDeriv:=calculateSecondDerivative(tData);
11:    if direction of data is upwards then
12:        featLoc:=findLocation(positive apex in tData);
13:        if data(featLoc) ≥ 10 μV then
14:            firstFeature:=data(featureLoc);
15:        else
16:            firstFeature:=null;
17:        end if
18:        featLoc:=findLocation(negative apex in tData);
19:        secondFeature:=data(featureLoc);
20:    else if direction of data is downwards then
21:        featLoc:=findLocation(negative apex in tData);
22:        if featLoc ≠ null then
23:            featLoc2:=findLocation(negative apex in
   data(featLoc:featLoc+ 5 ms))
24:            if featLoc2 ≠ null then
25:                firstFeature:=data(featLoc);
26:                secondFeature:=data(featLoc2);
27:            else
28:                firstFeature:=null;
29:                secondFeature:=data(featLoc);
30:            end if
31:        else
32:            featLoc:=null;
33:            featLoc2:=null;
34:            Display signal features not found.
35:        end if
36:    end if
37:    thirdFeature:=findLocation(positive apex in data(featLoc:
   featLoc+ 100 ms))
38:    Calculate respOnsetLatency:=t(respOnset)−t(stimOnset);
39:    Calculate respPeakLatency:=t(secondFeature)−t(respOnset);
40:    Calculate respPeakAmplitude:=data(secondFeature) −
   data(respOnset);
41:    Save and display data with detected features;
42: return firstFeature, secondFeature, thirdFeature,
   respOnsetLatency, respPeakLatency, respPeakAmplitude;
43: end procedure
```

Figure 4.14: Feature detection and parameter calculation algorithm.

Artifact removed single trial LFP signals were provided as inputs to the function and were scanned for occurrences of the above-mentioned features in those evoked responses. As shown in the Algorithm 3 box, each single trial LFP was low-pass filtered (250 Hz, Butterworth low-pass filter) and translated (on the y-axis) by setting the signal amplitude at the stimulus-onset to zero (Mahmud *et al.* [2010]). This translation helped to avoid the slow deviation of signal that might

obscure the real amplitude of the features. To detect even small changes in the signal shape, the second derivative of the signal was obtained. Large fluctuations in the derivative were used in detecting the features. Also, the features were time locked, meaning that a change in the signal derivative (either from up to down or vice versa) within a particular time window usually was indicative of a signal feature. The algorithm first identifies the response-onset as the starting point of the evoked response. The standard deviation of the signal's steady-state part (i.e., the part of the signal before stimulus-onset) was considered as threshold for the exact detection of the response-onset. A 10 ms-time window of the signal after the stimulus-onset was divided into small parts of 0.5 ms and derivatives of those parts were obtained. The response-onset was identified as the time instant of the signal when the small-parts-derivative was found to exceed a threshold value. After detection of the response-onset, the rest of the signal was divided into chunks and scanned for derivative change to find other features. Care was taken in case of the SP, which is rarely present in a signal and if so, may have either positive or negative direction. In case of positive direction, a threshold of 10 μV was set to make sure that it indeed was a feature and not just background spontaneous brain activity. If case of negative direction, then the maximum negative peak was found and from that peak the signal ranging $\pm$ 5 ms was scanned for occurrence of an another negative peak. If this second negative peak was found, the Feature 1 was set as the first occurring negative peak and the Feature 2 (RP) was set as the second negative peak, otherwise, the positive peak was absent and the Feature 2 (RP) was set as the maximum negative peak.

The Feature 3 (PR) occurred within the next 100 ms from Feature 2 (RP) and was identified as the local maxima in this window.

Once the features (Features 1, 2, 3) were detected the important parameters (ROL, RPL, and RPA) were estimated as follows:

ROL = Time(response-onset)$-$Time(stimulus-onset)

RPL = Time(Feature 2)$-$Time(response-onset)

RPA = Amplitude(Feature 2)$-$Amplitude(Feature 1)

where the functions 'Time()' and 'Amplitude()' denotes the instantaneous time and amplitude of the signal at a given point. The detected features and estimated parameters were saved in an ASCII coded text file for further processing and some

necessary figures are generated.

4.10.4 Spontaneous Activity Analysis

This analysis aim to detect all the negative peaks (nLFPs) that can be found in the spontaneous background activity, recorded at 50 kHz sampling rate in sweeps of 10 s duration, under the two different types of anesthesia and without driving any external stimulus to the animal. After detecting all the nLFPs, histograms and distributions of the four principal parameters considered in the "neuronal avalanches" statistical framework were calculated. These parameters describe the avalanches in the temporal domain (i.e., lifetimes, quiet times and waiting times) and in the amplitude domain (i.e., the sizes of the avalanches) (see chapter 2, section 2.4).

Each data set was analyzed as follows:

- **Step 1**: data were loaded;
- **Step 2**: signals were low-pass filtered at 50 Hz;
- **Step 3**: signals were down-sampled at $1/10^{\text{th}}$ of the original sampling rate;
- **Step 4**: a band-pass filter between 0.1 Hz and 50 Hz was applied to the data;
- **Step 5**: in order to remove the very slow trend present in electrophysiological traces, the envelope of the waveform was calculated by fitting the detected positive peaks with a spline polynomial and then this envelope was subtracted from the original trace;
- **Step 6**: once filtered and detrended, the second derivative of the signal was computed;
- **Step 7**: peak detection constraints were defined: i.e. peaks should be at least 10 ms in width and 100 μV in amplitude;
- **Step 8**: the threshold of detection of negative peaks was defined as the $1/4^{\text{th}}$ of the mean positive peaks of the second derivative which exceeds twice the standard deviation of the second derivative;

- **Step 9**: different activity levels were calculated by dividing the max amplitude of the signal by the amplitude constrain (i.e., 100 μV);
- **Step 10**: for all the defined levels:
  - peaks were checked for threshold crossing;
  - the start and the end point of peaks was checked (and plotted along with the detrended traces in the single sweep plots that are generated to allow the user's visual control);
  - detected peaks were checked for false events by comparing their sizes with the amplitude and width constraints;
  - four main parameters were extracted from checked events: (1) the event duration (i.e. the lifetime, as the difference between the start and the end point), (2) the quiet time (the difference between the end of the previous event and the start of the current one), (3) the Inter Event Interval (i.e. the waiting time, as the difference between the start of two successive events) and (4) the relative amplitude (as the difference between the amplitude at the start and the minimum of the peak);
- **Step 11**: Finally, histograms of the parameters were calculated using semilog(x) normalized coordinates and a fixed number of bins (equal to 20). Histograms were then plotted in semilog(x) and loglog graphs.

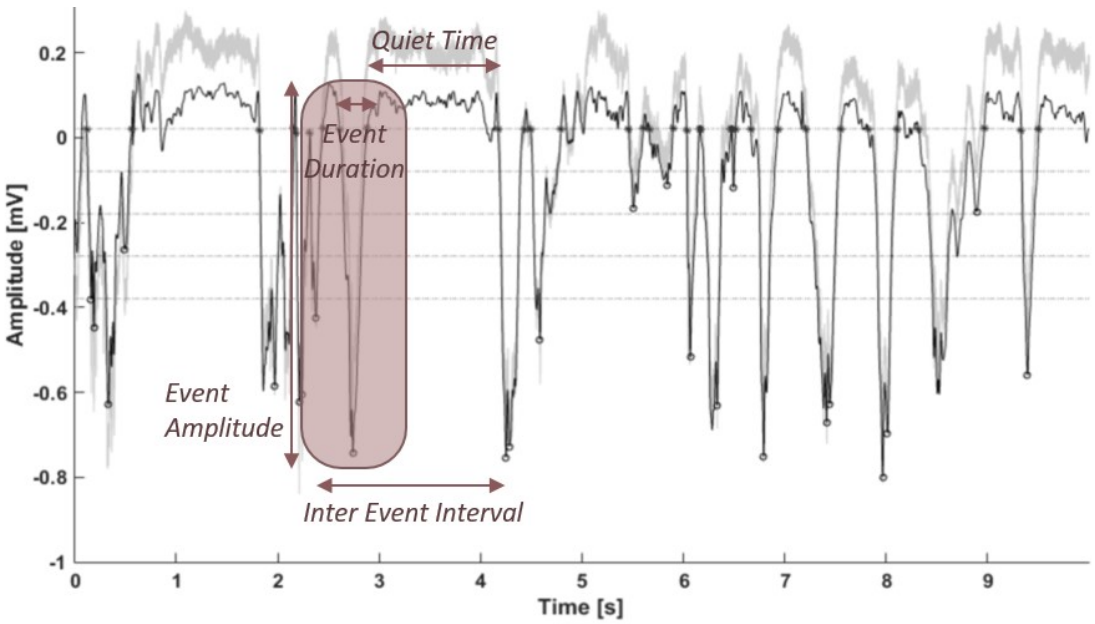

Figure 4.15: Representative spontaneous activity trace with relevant parameters.

4.11 Histological Analysis and Verification of Recording Sites

After the experiments performed using implantable chips, the coordinates of the insertion within the barrel field and damages or lesions produced in the tissue by the needle were checked through common histological essays. At the end of the recording sessions, brains were removed from the skull, cortices were isolated and immersed in fixative (Formalin solution, neutral buffered, 10%, Sigma-Aldrich Co, Missouri, USA) for at least 48 h. Sections through the somatosensory cortex were cut on a vibrating blade microtome (Leica VT1000 S, Leica Biosystems GmbH, Nussloch, Germany). Histological verification of the recording sites was performed on 50 μm thick flattened tangential (horizontal) sections of the right hemisphere. Needle chip tracks along the entire cortical depth were visualized in 50 μm thick coronal slices of the right hemisphere. Barrels within layer IV were visualized in both types of cortical sections via Cytochrome Oxidase staining according to Wong-Riley [1979], using Cytochrome C Type III (Sigma C-2506) or via Toluidine

Blue staining (0.02% solution in PBS). Slices were observed and images were acquired by bright-field microscopy through a confocal microscope (Nikon Eclipse 80i, Nikon Instruments Inc., Melville, NY, USA) equipped with an air immersion objective (Plan 4x, 0.10 NA, 18.5 mm WD, Olympus Italia SRL, Milan, Italy) and a digital camera (QICAM 12-bit Mono Fast 1394 Cooled, 12-bit, 1392 $\times$ 1040 pixels, QImaging, Surrey, BC, Canada).

Chapter 5

Results and Discussion

5.1 Piezoelectric Whisker Stimulation

One of the first results regards the repeatability and the accuracy of the whisker stimulation. From the videos recorded through a high-speed camera we could track the movement of the whisker after stimulation with the piezoelectric bender. We also tested the linearity of the device, by setting different voltage values to the waveform generator that drives it.

As we can see from the traces obtained analyzing four different videos (Figure 5.1), whisker deflections are very repeatable, and do not show large secondary oscillations after the main displacement. By analyzing the videos of the displacements generated by the deflection of the piezoelectric bender driven by different voltages, it was possible to obtain the average distance travelled by the whisker along its displacement axis in correspondence of the different voltages and to check the linearity of the stimulation system.

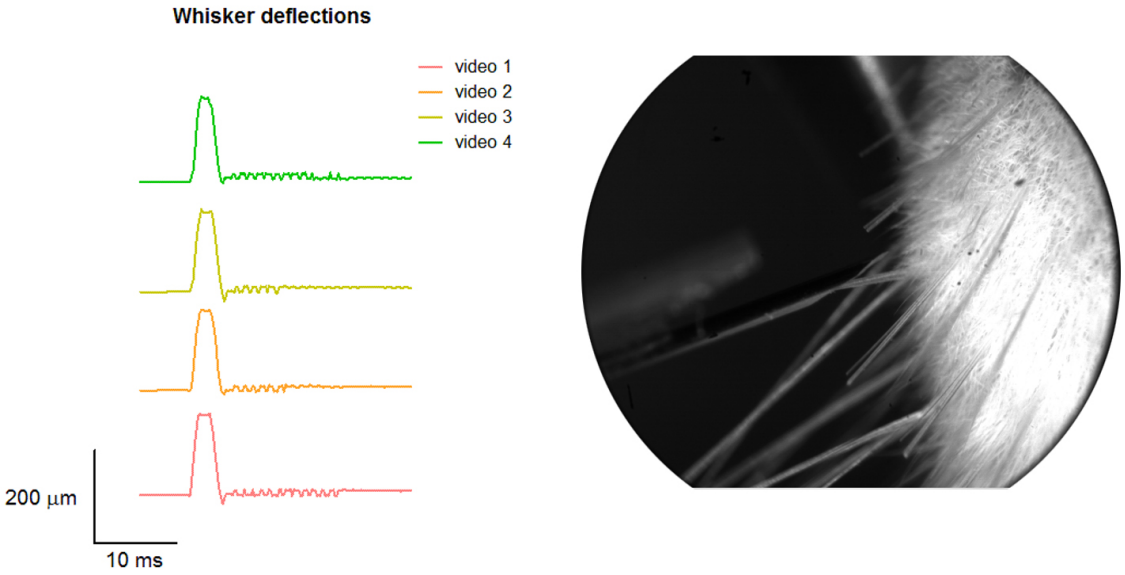

Figure 5.1: (Left) Four video-tracking of the whisker motion, after stimulating it repeatedly with the maximum applicable voltage to the piezoelectric bender (3 V). The average deflection of the whisker is about 200 μm. (Right) A frame of a video acquired by the high-speed camera during the deflection of the whisker.

piezo V	**Δx (μm)**	**$\Delta\theta$(°)**
0.1	2.5	0.1
0.25	13	0.5
0.5	28	1.0
1.0	60	2.2
2.0	120	4.4
3.0	178	7.3

Table 5.1: Average whisker deflection along its displacement axis and average angular whisker deflection (angles measured from the whisker pad) in correspondence of the different voltages applied to the piezoelectric bender.

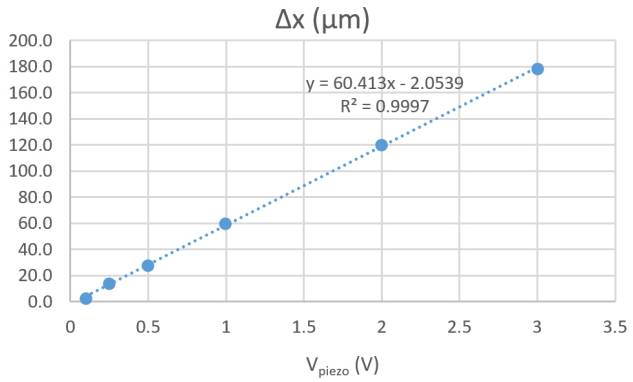

Figure 5.2: The amplitude of the whisker displacement is almost linearly dependent from the voltage applied to the piezoelectric device (in the 0÷3 V range).

The deflection system was almost linear, with a coefficient of determination of the linear regression very close to one (R^2 =0.9997).

5.2 Evoked Responses

5.2.1 Response Variability in Different Brain Regions

Evoked response variability was examined in correspondence of different cortical layers of the barrel cortex and in the trigeminal ganglion. Trial-to-trial variability depends strongly on the cortical depth: LFPs recorded from upper layers (i.e., layer II, 200 μm) showed less variability and were more repeatable than those recorded from lower layers (i.e., layer IV, 700 μm). This feature is likely to be associated with different streams of information along the cortical column and due to the particular connectivity of the barrel network.

Conversely, responses recorded from the trigeminal ganglion were nearly constant, showing repeatable shapes and no adaptation or saturation phenomena with this quite long inter-stimulus interval (2 s). Evoked LFPs recorded from the trigeminal ganglion had a mean latency of response onset equal to t_{onset} = (6.45 ± 0.06) ms, a latency of the first principal peak equal to t_{peak} = (22.5 ± 1.0) ms and a mean amplitude of ΔV = (129 ± 4) μV.

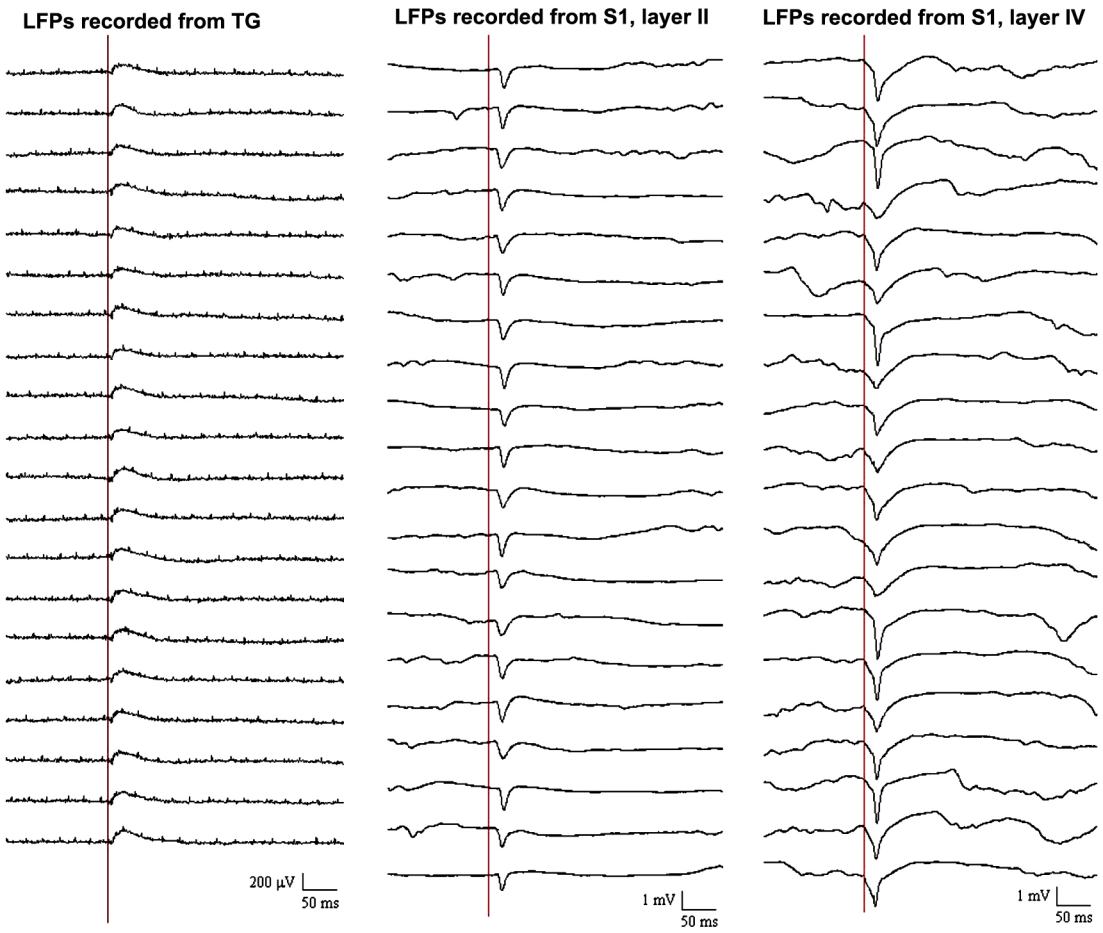

Figure 5.3: Representative LFPs recorded from three different locations of the brain: the Trigeminal Ganglion (left), the layer II (middle), and layer IV (right) of the primary somatosensory cortex. The vertical red line marks the onset of the whisker's stimulation. Signals were recorded under tiletamine-xylazine anesthesia.

5.2.2 LFPs Variability and Parameters Extraction

The effect of the anesthesia on the sensory information processing was assessed by comparing the main features of the evoked single LFPs recorded from different rats ($n = 9$) anesthetized with two different kind of anesthetics: tiletamine-xylazine and urethane.

Histograms were made from the extracted main parameters of the single LFPs

traces. To better illustrate the trends in each anesthetic, estimation of the histograms were calculated by fitting higher order polynomials to them. Data from different rats were binned together: 5 rats in the case of tiletamine-xylazine anesthetic and 4 rats in the case of urethane.

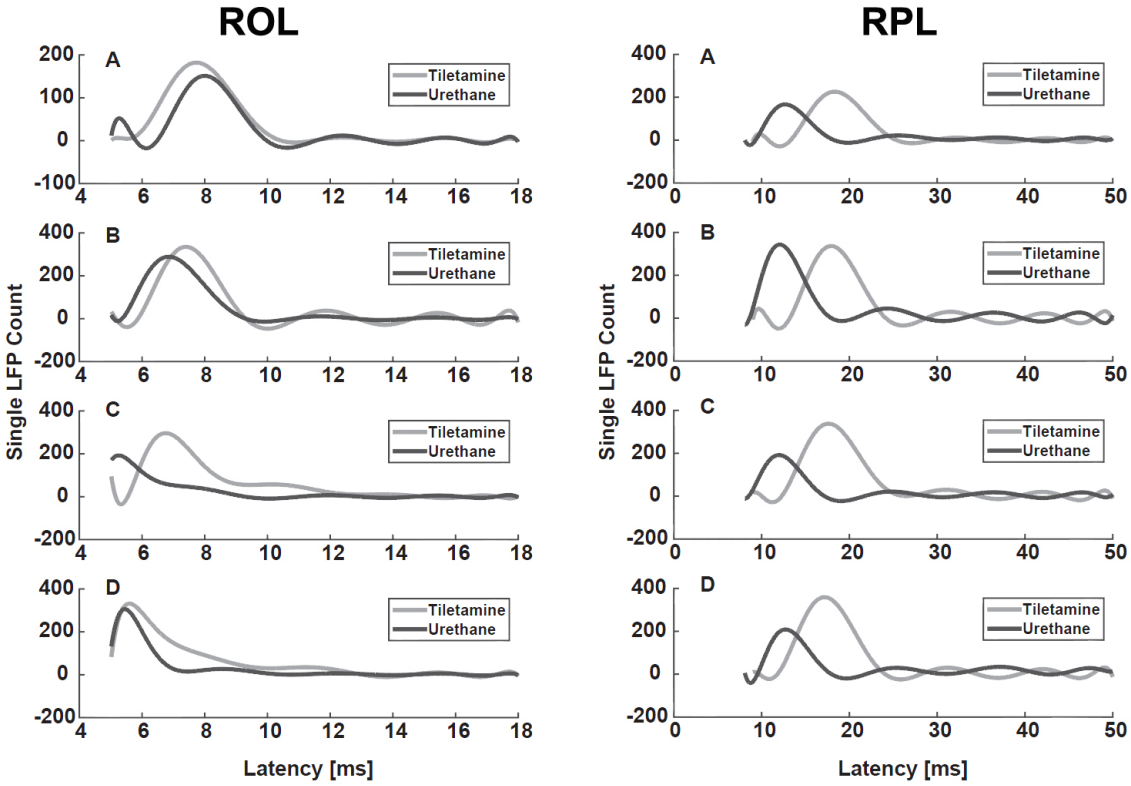

Figure 5.4: (Left) Histogram estimation (bin: 0.45 ms) for the Response Onset Latency (ROL). (Right) Histogram estimation (bin: 1.25 ms) for the Response Peak Latency (RPL). The histograms were calculated from signals recorded at different recording depths: A. 320 μm (layer II); B. 420 μm (layer III); C. 720 μm (layer IV); D. 920 μm (layer Va).

The detected principal events' amplitudes in the acquired signals were normalized according to the equation $\Delta V_{norm} = (\Delta V - \Delta V_{min})/(\Delta V_{max} - \Delta V_{min})$ where ΔV_{min} and ΔV_{max} are minimum and maximum amplitudes of the response peak identified from a single cortical depth for each rat.

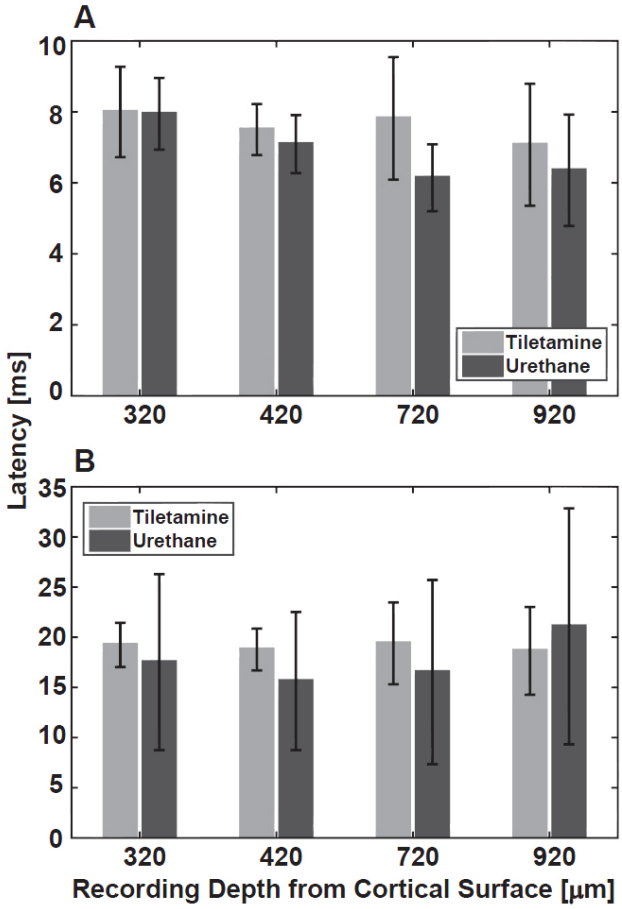

Figure 5.5: Comparison of the mean latencies for the ROL (A) and RPL (B) at different depths. The error bars indicate the standard deviations.

It can be seen that the responses recorded under tiletamine-xylazine more profoundly follow the typical evoked response's signature (99.06% of recorded single LFPs were detected) in comparison to the ones recorded under urethane-based anesthetic (93.69% of recorded single LFPs were detected). This was in line with the difficulties of detecting and recording evoked responses in urethane-anesthetized rats, already mentioned in chapter 1 section 1.3 (see Figure 5.7).

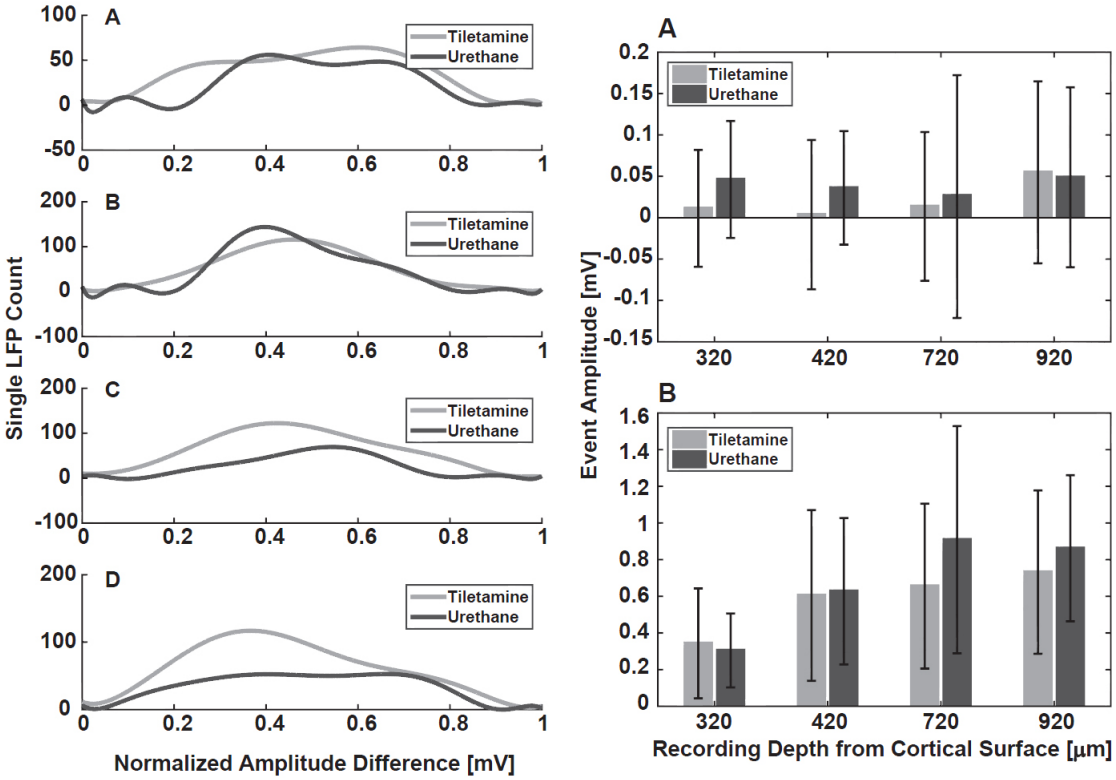

Figure 5.6: (Left) Histogram estimation (bin: 1.25 ms) for the Response Peak Amplitude (RPA) at different recording depths: A. 320 μm (layer II); B. 420 μm (layer III); C. 720 μm (layer IV); D. 920 μm (layer Va). (Right) Comparison of the mean amplitudes for the Response Onest Amplitude (ROA) (A) and RPA (B) at different depths. The error bars indicate the standard deviations.

Interestingly, the degree of variability of single evoked LFPs was not the same across all the cortical layers. Under tiletamine-xylazine, the evoked responses recorded from the superficial layers (i.e., layer II and layer III) showed less variability than those recorded from deeper layers (i.e., layer IV and layer Va). This was highlighted in the distributions of the onset and peak latencies (see Figure 5.4): in particular, the distribution of the onset latencies was much wider in the deeper layers than those in the superficial ones. Surprisingly, this trend was somewhat reversed in the evoked LFPs recorded under urethane: the distributions of the onset and peak latencies were slightly narrower in the deeper layers than

those in the superficial ones, with the broadest distribution found in layer III. This feature is likely to be associated with different streams of information along the cortical column modulated by the type and the level of anesthesia and due to the interlayer connectivity of the barrel network.

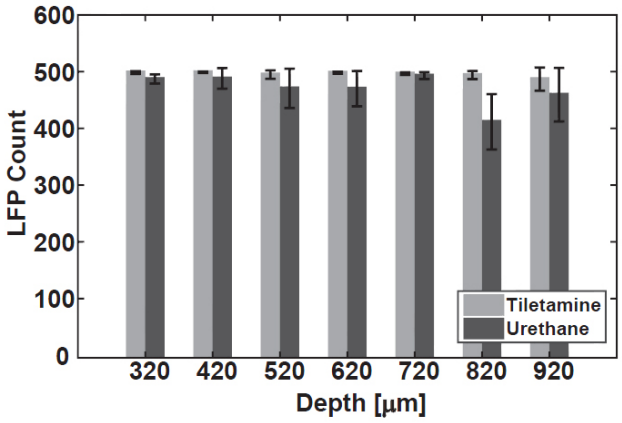

Figure 5.7: Feature detection accuracy in the single LFPs recorded under the two different anesthetics. Means and standard deviations are represented by bars and error bars, respectively. The means and standard deviations were obtained with at least three experiments (n=3) from each cortical depths.

From the comparison of the distributions obtained with the two different anesthetics, it seemed that the peak latency distributions were narrower in the case of urethane and that the peak of the evoked LFPs occurred earlier under urethane than the one recorded under tiletamine-xylazine anesthesia. This was confirmed by the direct comparison of the mean values of the onset (see Figure 5.5A) and the peak latency (see Figure 5.5B).

The distributions of the amplitude of the first principal peak were less informative, showing wide and flattened distributions (see Figure 5.6). However, comparing the mean values of the first principal peaks' amplitudes, we noticed that the evoked responses elicited by the whisker stimulation were larger in animals anesthetized with urethane. This behavior may be associated with the different effect of these two anesthetics on the synaptic plasticity, but this is yet to be confirmed.

5.2.3 Stimulus-Response Analysis

Thanks to the finely tuned piezoelectric whisker stimulation, it was possible to investigate how the evoked response varies as the amplitude of the whisker deflection changes. By varying the voltage applied to the piezoelectric device from 100 mV (about 2.5 μm of displacement) to 3 V (about 180 μm of displacement) it was possible to obtain a stimulus-response curve for whisker stimulation.

As expected, the amplitude of the evoked response increased as the amplitude of the whisker deflection increases. Interestingly, also the positive rebound (Feature 3) increased accordingly. Moreover, the response became more peaked as the amplitude of the deflection increases.

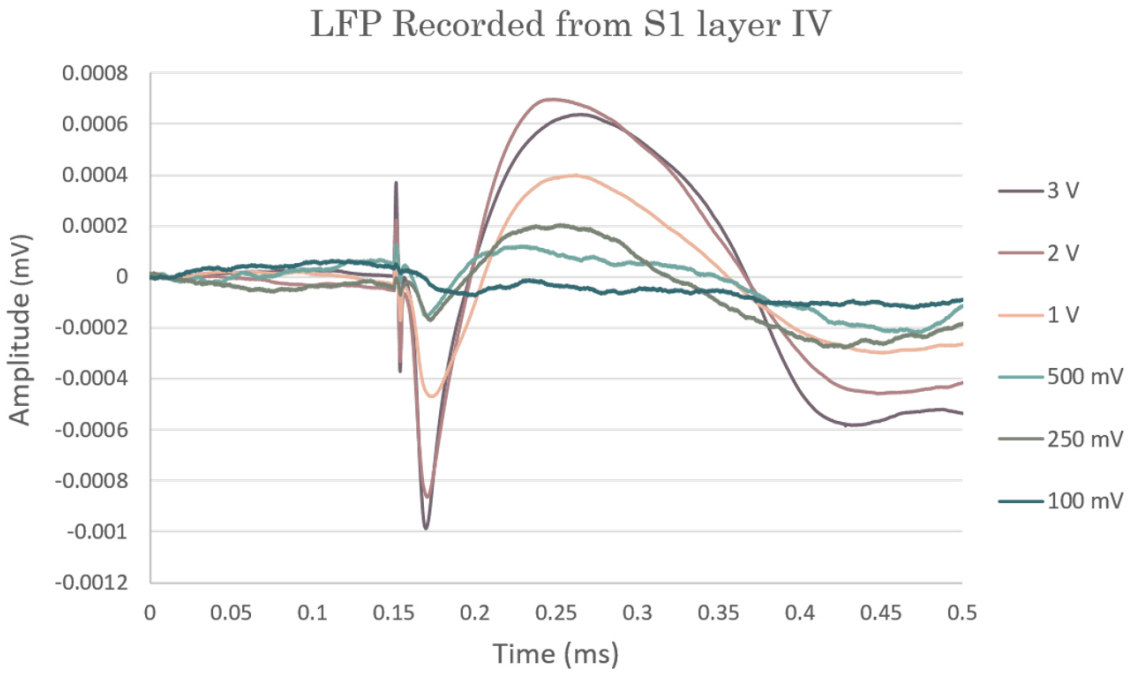

Figure 5.8: Evoked LFP responses in the barrel cortex recorded after deflecting the whisker with variable amplitude, obtained by applying different voltage values to the piezoelectric bender.

In physiology, this behavior of the stimulus-response curve was commonly explained by a law, the Stevens' power law (see Figure 5.10).

piezo V	Δx (μm)	Evoked LFP (mV)
0.1	2.5	0.101
0.25	13	0.147
0.5	28	0.201
1.0	60	0.430
2.0	120	0.798
3.0	178	0.983

Table 5.2: Average evoked response amplitude in the barrel cortex in correspondence of the different amplitudes of whisker deflection obtained by driving the piezoelectric bender with different voltage values.

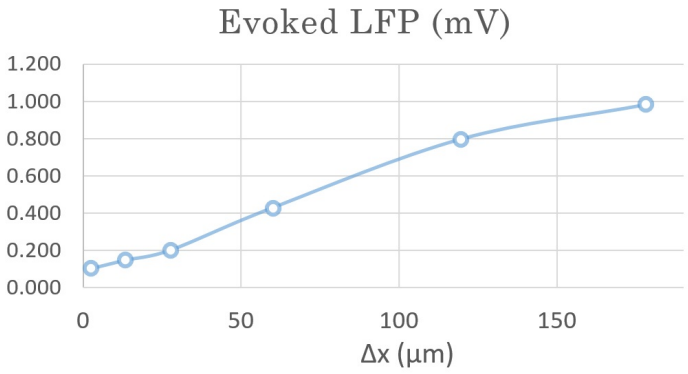

Figure 5.9: Stimulus-response curve for whisker stimulation. Varying the intensity of the stimulus (i.e., the amplitude of whisker deflection), the amplitude of the evoked response in the cortex varies accordingly.

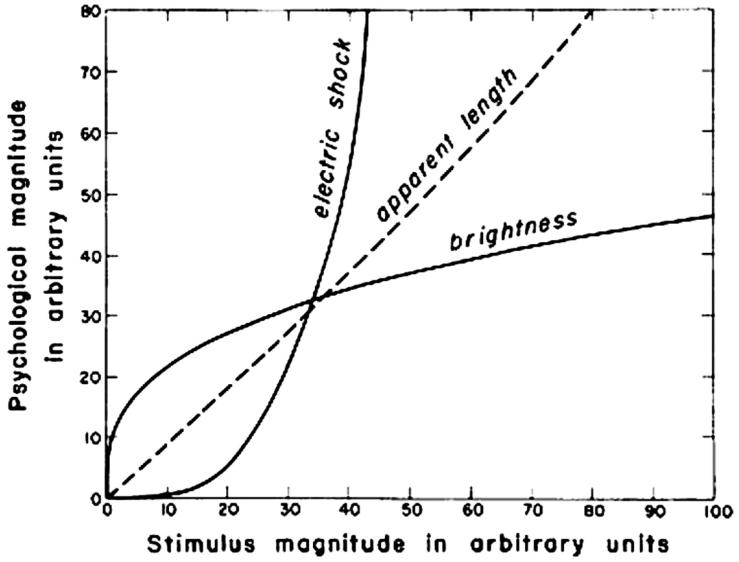

Figure 5.10: Stevens' power law. This law was proposed by Stevens in 1957 to describe the relationship between the magnitude of a physical stimulus and its perceived intensity or strength. The general form of the law is $S = kI^a$ where I is the magnitude of the physical stimulus, S is the subjective magnitude of the sensation evoked by the stimulus, a is an exponent that depends on the type of stimulation and k is a proportionality constant that depends on the units used.

It appeared that, approaching the 200-μm whisker displacement, the evoked response moves toward a saturation point (or at least a horizontal asymptote, as the stimulus-response curve for brightness in Figure 5.10).

5.3 Basal Activity and Neuronal Avalanches

Spontaneous background activity was recorded during both types of anesthesia used, tiletamine-xylazine and urethane. Under urethane anesthesia, spontaneous activity presented very periodic oscillations, alternating between intervals of sustained activity and intervals with no activity. Moreover, bursts of very fast activity mounted on the global envelope were detected occasionally. Under tiletamine-xylazine anesthesia, the spontaneous activity was more regular, showing a continuous pattern of negative peaks.

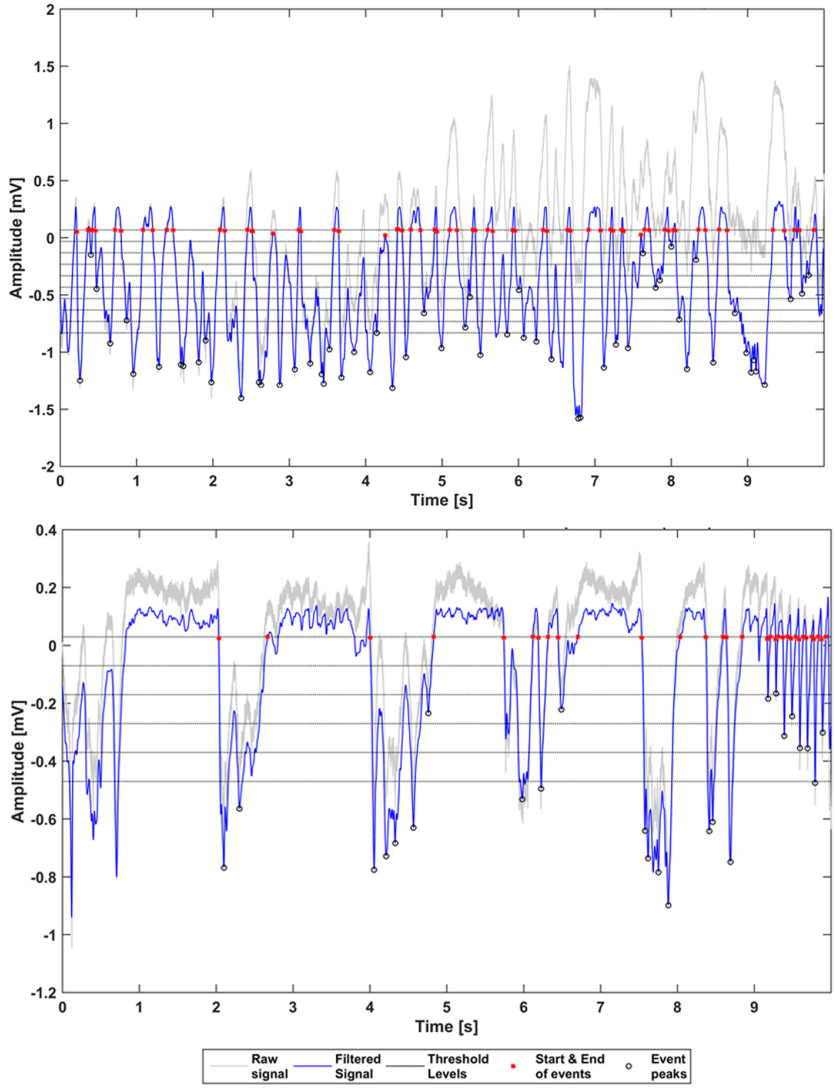

Figure 5.11: Spontaneous activity recorded in layer IV of the barrel cortex, under tiletamine-xylazine anesthesia (top) and urethane anesthesia (bottom).

We analyzed the distributions of the principal features of the nLFPs (waiting times, quiet times, lifetimes and amplitudes) detected on the spontaneous activity under the two different types of anesthesia used. One example of these distributions is reported for both types of anesthesia.

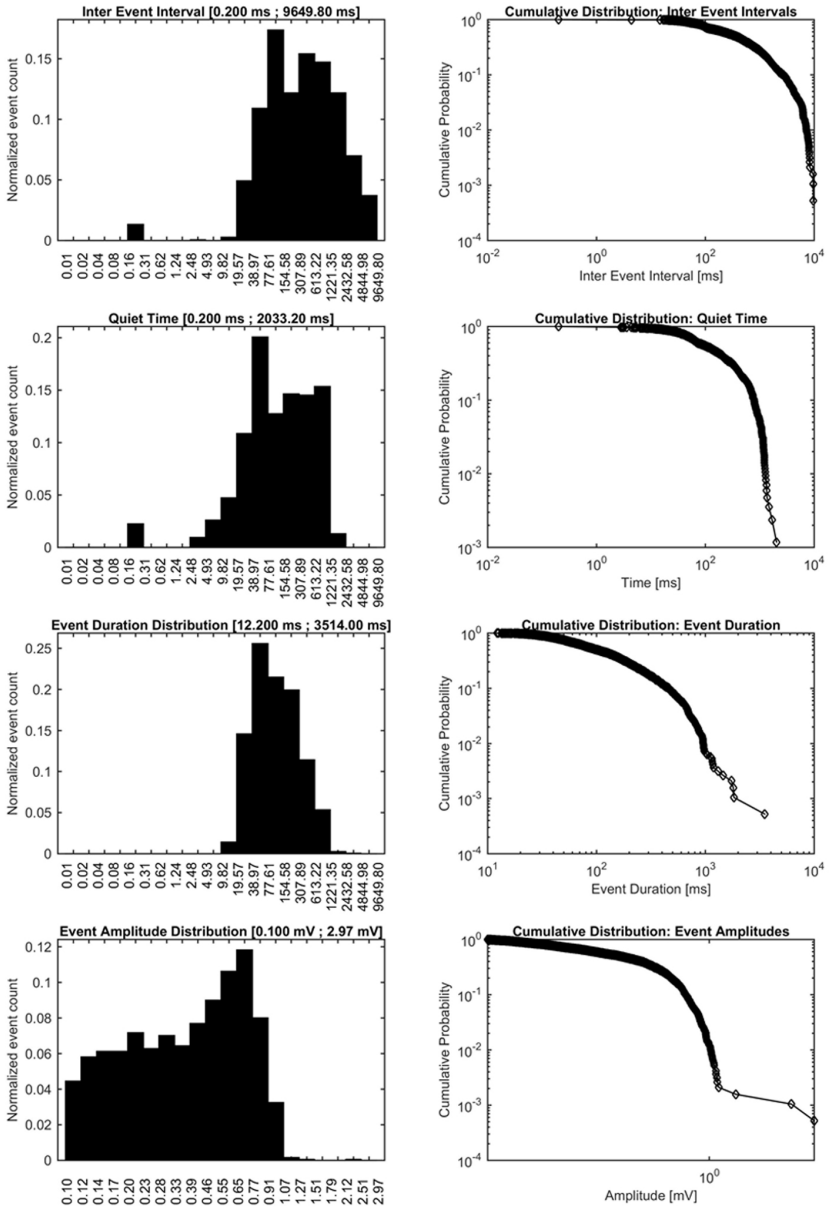

Figure 5.12: Semilog(x) & loglog distributions of waiting times, quiet times, lifetimes and amplitudes of nLFPs in spontaneous activities recorded in layer IV of the barrel cortex under tiletamine-xylazine.

From these very first distributions obtained from the basal activity no clear power laws could be detected. This could be a problem due to the analysis of neuronal avalanches from only one-electrode records. In some loglog graphs a

double-trended linear distribution could be found, probably due to the activity of two different neuronal populations, each one with its characteristic timescale and spatial distribution.

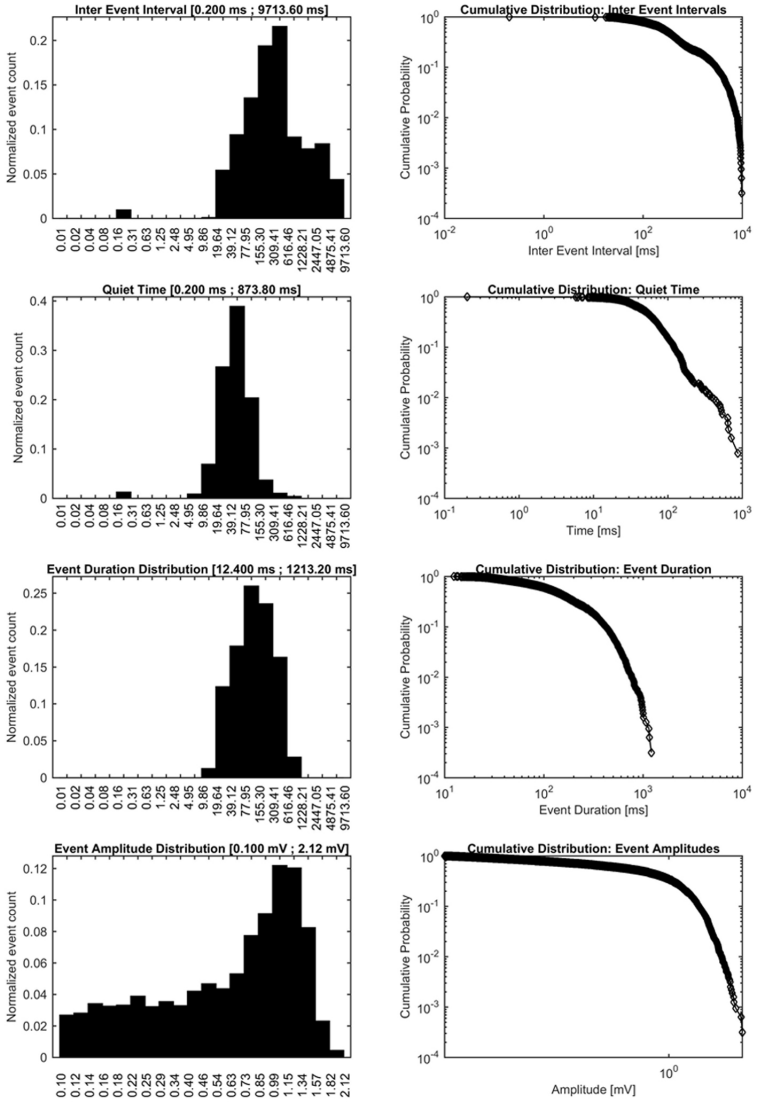

Figure 5.13: Semilog(x) & loglog distributions of waiting times, quiet times, lifetimes and amplitudes of nLFPs in spontaneous activities recorded in layer IV of the barrel cortex under urethane anesthesia.

More information about neuronal avalanches in *in-vivo* experiments will be gained from multisite recordings of spontaneous activity.

5.4 First Depth Profiles with CMOS Needle Chips

We report here the very first results of recording evoked responses in barrel cortex through high-resolution CMOS implantable needle chips (Figure 5.14).

The LFP profile shows a clear propagation of the neuronal signal: in upper cortical layers (I and II) the signals have a small positive peak, a main negative peak, a positive peak and a slow negative valley that gradually tends to reach the baseline at the end. In the middle layers (III, IV and V) they have a main negative peak, a slow positive peak, and a slow negative valley. Going deeper in the cortex (layer VI), the main negative peak becomes smaller and gets divided into two smaller negative peaks, followed by a slow positive peak and a slow negative valley.

From these very first cortical LFP profiles we spotted a characteristic propagation flow of information for the evoked LFPs recorded by the 16 $\times$ 16 multisite array at different cortical depths, with direction of the flow depending on the cortical layer. This signal propagation is clearly visible in Figure 5.15, starting from the right-bottom corner of the recording area and moving towards the left-bottom corner.

This is a particular feature of sensory transmission in the cortex, which has never been studied before at this very high spatial resolution. This propagation will be further characterized by analyzing how its direction and its extent vary with the amplitude, the direction and the timing of the stimulus applied to the whisker.

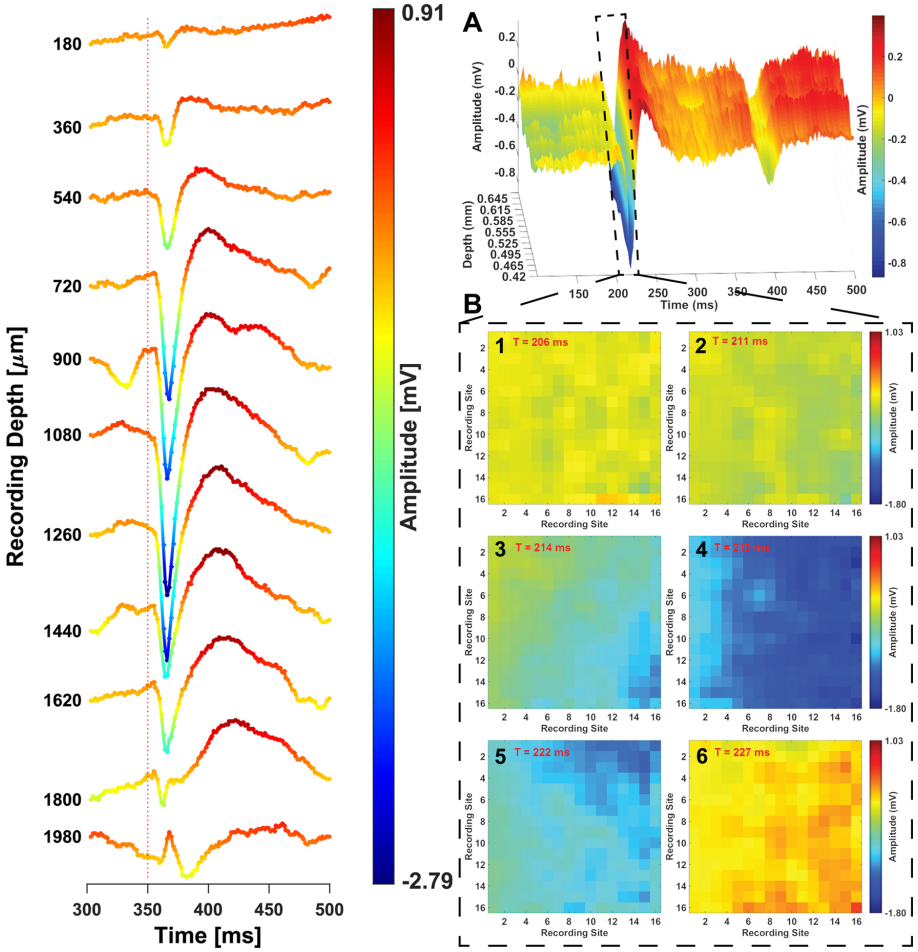

Figure 5.14: (Left) Averaged depth profile recorded with a 16 × 16 array inserted at different cortical depths. Plotted signals were obtained by averaging all the columns of the first row of the array (the nearest one to the tip of the needle) and all the trials (20 traces). (Right) a). Columnar LFP profile within the rat barrel cortex. Pseudo color plot of LFP evoked by whisker stimulation as recorded in layer IV of a single barrel (zero at 720 μm) in the rat somatosensory cortex at 15-μm resolution by a column of recording sites. The needle chip was inserted orthogonally to the cortical surface to penetrate at the interior of a single barrel. The corresponding whisker is stimulated at 200 ms. The typical biphasic LFP response follows stimulation and ends at about 350 ms, with a subsequent spontaneous LFP peak appearing at around 400 ms. Color code: warm and cold colors indicate positive and negative potentials, respectively. b) LFP whole frame recording. Representative frames recorded by the entire 16 × 16 array during the first part of the LFP shown in a).

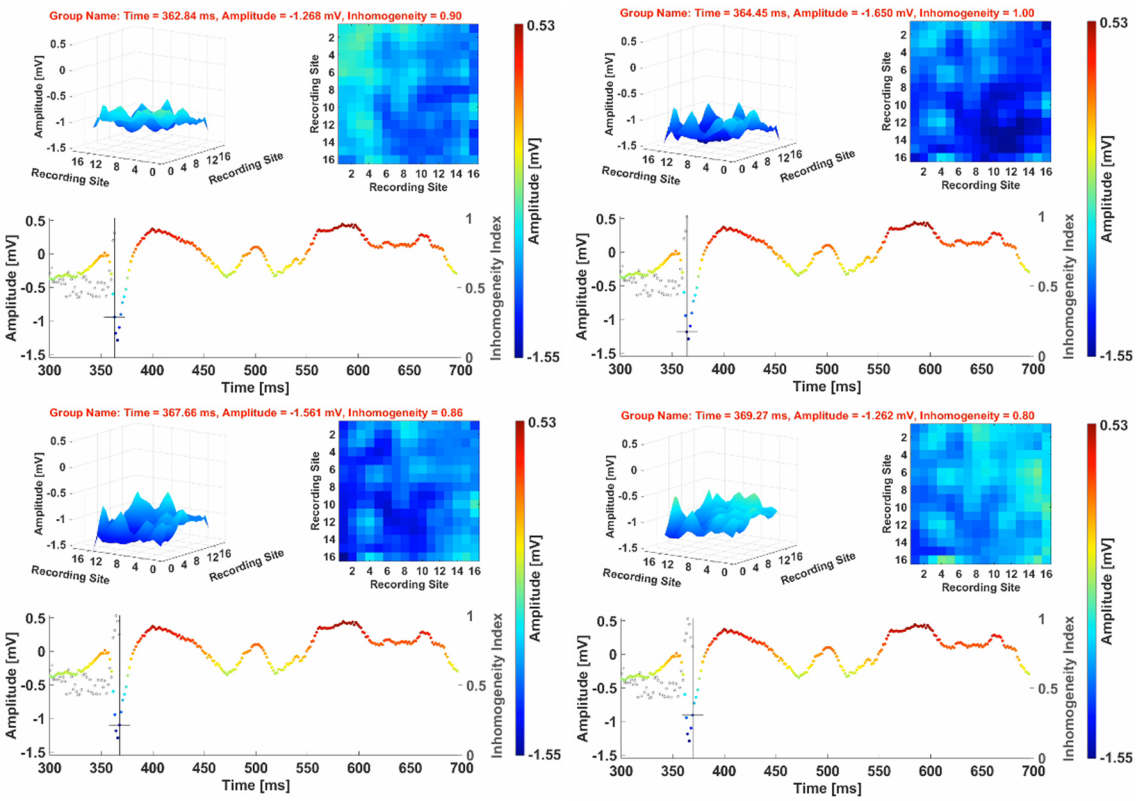

Figure 5.15: Four different temporal frames of the evoked LFP response recorded in layer IV. The vertical gray line indicates the temporal coordinate of the showed frame. A propagation flow from the right-bottom corner to the left is clearly visible.

5.5 Histological Verification of Recording Sites

5.5.1 Tangential Sections

The position of the insertion of the chip in the barrel field was checked in flattened tangential sections of the cortex. The chip was always implanted inside the barrel field, in a barrel near the one that was stimulated by the whisker deflection. Large hematomas were sometimes present in the slices near the insertion point, due to bleeding of the tissue during and after the implantation procedure.

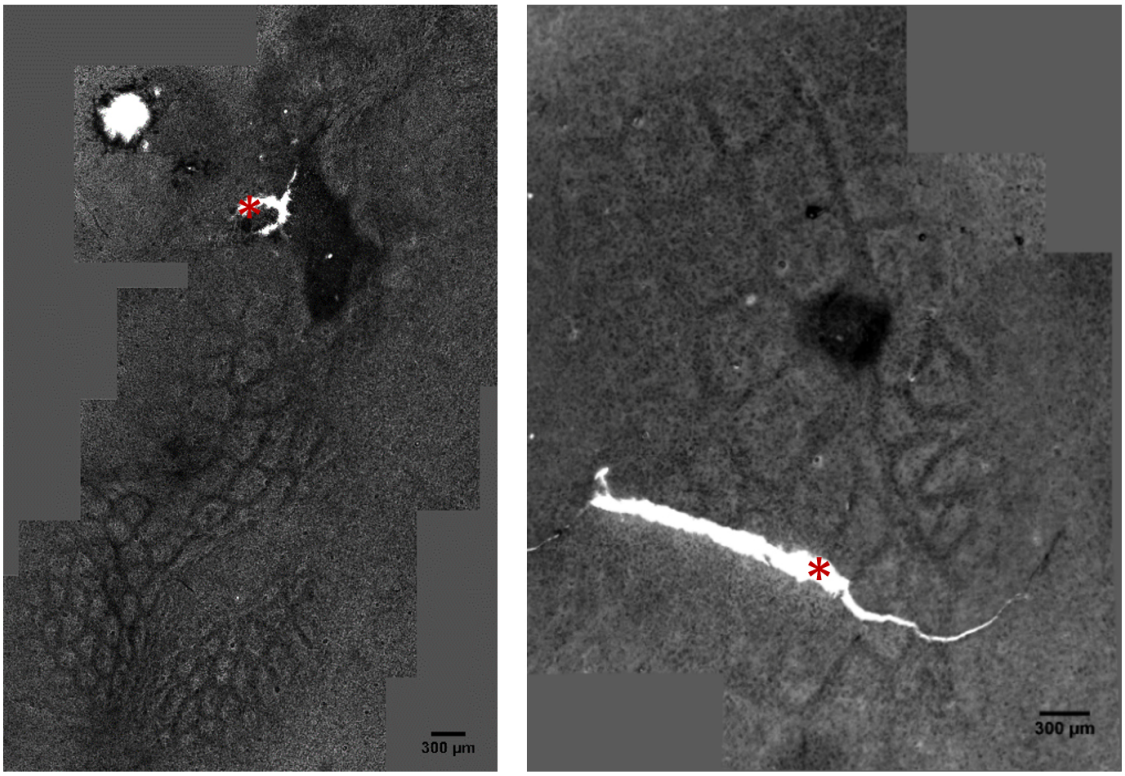

Figure 5.16: Tangential (horizontal) sections stained with Toluidine Blue in two different animals. The red asterisks indicate the position of the chip. In the right image, the trace of the chip became wider after the sectioning of the tissue.

5.5.2 Coronal Sections

The orthogonality of the insertion was verified in coronal sections of the cortex. As it can be seen from the images, the chip was implanted almost perpendicular to the surface, following the direction of development of a single barrel in depth. Barrels were fairly discernable in correspondence of layer IV.

Figure 5.17: Coronal sections stained with Cytochrome C in two different animals. The red boxes indicate the position of the recording chip.

Chapter 6

Conclusions

In this work, we managed to successfully record LFPs evoked in the barrel cortex by means of high-resolution CMOS implantable needle chips, also finding an interesting characteristic propagation flow of information for the evoked LFPs recorded by the 16 $\times$ 16 multisite array at different cortical depths. Moreover, we discussed the variability of the evoked response recorded during two different types of anesthesia by means of conventional electrodes: preliminary analyses of the main parameters extracted from the recorded LFPs revealed that the deflection of the whisker is encoded more reliably in the temporal domain of the signal rather than in its amplitude. Furthermore, the evoked responses seemed to be deeply influenced by the type of anesthetics used. Finally, we also analyzed the spontaneous background activity of cortical networks during two different types of anesthesia in the context of neuronal avalanches. From these preliminary analysis of single-electrode records of the basal activity, no clear power-law behaviors can be spotted. More information about neuronal avalanches in *in-vivo* experiments will be gained from the analysis of multisite recordings of spontaneous activity.

Chapter 7

Future Perspectives

One of the next objectives in this study will be the careful analysis of the propagation flow in the barrel cortex of the sensory information coming from the whiskers through the area of the recording array of the implantable chips at different cortical depths, even by making use of fluid dynamics methods. In this context, the analysis of the effect of different directions and magnitudes of whisker displacement on the principal parameters of the evoked response and on the size and direction of the cortical spreading of the response will be of great interest.

For what concerns the basal activity, high-resolution chips will also enable to record the spontaneous activity simultaneously from many cortical sites. Then, the analysis in the neuronal avalanches framework of the distributions of the parameters of 'bursts' identified in the electrophysiological traces recorded through multiple-electrode arrays will be straightforward, with the same methodology found in other publications.

Chapter 8

Biomedical Applications of Implantable Chips

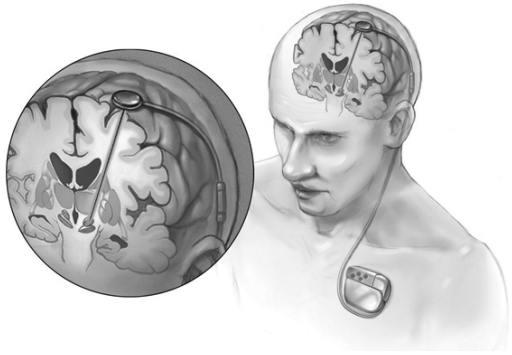

A future medical application of these implantable devices is of course hoped. A promising field in tremendous expansion is the one of 'electroceuticals' (for review, see Famm *et al.* [2013]). 'Electroceuticals' will be miniaturized devices that target individual nerve fibres or connect to specific brain circuits to treat an array of conditions. These treatments could modulate the neural impulses and the electrical signalling patterns and they are capable of controlling the body, repairing lost functions and helping in restoring health, also reverting the course of neurodegenerative diseases. Clinical neural implants such as cochlear implants to restore hearing, retinal implants to restore sight, spinal cord stimulators for pain relief or cardiac pacemakers and implantable defibrillators are conventional examples of electroceuticals. More recent varieties of electroceuticals include the electrical stimulation of the vagus nerve to modulate the immune system, in order to provide relief from rheumatoid arthritis and prevent epileptic seizures.

Electrical impulses - namely action potentials - are the language of the body's

nervous system. Virtually all organs and functions are regulated through circuits of neurons communicating through such impulses (Kandel [2012]), that can be recorded and monitored through multi-electrode devices.

The neural tissue is compact: unrelated circuits often run close together through brain regions and in peripheral nerves. At present, electrical devices activate or inhibit cells in an area of tissue indiscriminately, muddying clinical effects. For example, deep-brain stimulation for Parkinson's disease affects many cells other than those that control movement, leading to emotional and cognitive side effects. On the contrary, our devices, thanks to their small dimensions, will be able to track the neuronal activity very precisely in a tiny brain area, without causing major damages to the tissue during the insertion. In the near future, the use of these semiconductor devices will help, among other things, to understand how degenerating syndromes like Parkinson or Alzheimer evolve, by coupling detected behaviors and symptoms of the disease to neuronal features and to counteract the disease by constituting intelligent neuronal prostheses that can support and functionally train impaired neuronal networks.

Appendix A

Enhancement of $K_v1.3$ Potassium Conductance by Extremely Low Frequency Electromagnetic Field

In this additional study, we assessed the effect of electromagnetic fields on potassium $K_v1.3$ channels expressed in CHO-K1 cells. Being the potassium channel one of the most important channels for generating and modulating the neuronal signal, with this preliminary study we aimed to understand the possible behaviour of neurons exposed to the electromagnetic radiation.

A. 1 Abstract

Theoretical and experimental evidences support the hypothesis that extremely low-frequency electromagnetic fields can affect voltage-gated channels. Little is known, however, about their effect on potassium channels. $K_v1.3$, a member of the voltage-gated potassium channels family originally discovered in the brain, is a key player in important biological processes including antigen-dependent activation of T-cells during the immune response. We report that $K_v1.3$ expressed in CHO-K1 cells can be modulated in cell subpopulations by extremely low frequency and relatively low intensity electromagnetic fields. In particular, we observed that field exposure can cause an enhancement of $K_v1.3$ potassium conductance and that the effect lasts for several minutes after field removal. The results contribute to put immune and nervous system responses to extremely low-frequency electromagnetic

fields into a new perspective, with $K_v1.3$ playing a pivotal molecular role.

A. 2 Introduction

Electromagnetic fields in the 0.03 - 300 Hz frequency range are commonly known as extremely low-frequency electromagnetic fields (ELF-EMF) and are found in the public or domestic environment with intensities up to several hundreds of μT near appliances (World Health Organization (WHO) [2015]). Several studies provided evidence that exposure to ELF-EMF can cause biological effects, such as a modulation of cell proliferation and differentiation, but molecular actors behind such cellular responses remain to be identified (Funk et al. [2009]). In mammalian cells, voltage-gated ion channels (VGC) are among suitable candidates. In fact, theoretical models (Funk et al. [2009]) and experimental studies on calcium (Pall [2013]) and sodium channels (He et al. [2013]) support this hypothesis, with fields that may act on the channel directly or by interposition of cellular signalling pathways (Gartzke and Lange [2002]; Funk et al. [2009]; He et al. [2013]; Pall [2013]). Yet, effects on VGC of the potassium family, K_v, are mostly unexplored, except for the recent work of (Gavoçi et al. [2013]) reporting that an AC low-frequency (8 Hz) and low-intensity (100 μT) field was not altering Tetraethylammonium (TEA)-sensitive potassium currents in neuroblastoma cells. K_v channels are of paramount importance in cell physiology and represent one of the most diverse and ubiquitous families of membrane proteins. The K_v superfamily comprises 12 subfamilies (K_v1-K_v12), all formed by tetrameric membrane-spanning protein complexes that create a selective pore for potassium ions. Each subunit is formed by six transmembrane segments (S1-S6), with S1-S4 constituting a voltage sensor domain (VSD) and S5-S6 the pore-forming region (Coetzee et al. [1999]; Gutman et al. [2003]). $K_v1.3$ is a member of the Shaker (K_v1) delayed rectifier family and it was identified in the brain and in several regions throughout the body (Swanson et al. [1990]; Bielanska et al. [2009]; Bielanska et al. [2010]). In particular, although mainly expressed in the olfactory bulb and lymphocytes (Duque et al. [2013]), $K_v1.3$ is found in the hippocampus (Veh et al. [1995]), epithelia (Grunnet et al. [2003]), adipose tissue (Xu et al. [2004]), and both skeletal and smooth muscle (Villalonga et al. [2008]; Bielanska et al. [2012a]; Bielanska et al.

[2012b]). Intriguingly, in addition to the plasma membrane, the channel's presence in mitochondria has been recently demonstrated (Szabò and Zoratti [2014]; Szabò et al. [2010]). $K_v1.3$ has attracted much attention for playing diverse biological functions relevant to clinics. Above all, it is involved in antigen-dependent T-cells activation during the immune response together with the Ca^{2+}-activated IKCa1 K^+ channel, and is therefore considered a potentially elective therapeutic target for immunomodulation (Beeton et al. [2001]; George Chandy et al. [2004]; Gocke et al. [2012]; Hansen [2014]; Kahlfuß et al. [2014]; Panyi [2005]; Wang and Xiang [2013]; Wulff et al. [2003]). Furthermore, it is assumed to contribute to class-switching of memory B cells (Wulff et al. [2004]). Along with such immune system-specific functions, $K_v1.3$ has been also proposed to contribute to modulation of sensitivity to insulin (Upadhyay et al. [2013]) and to the regulation of crucial cellular processes such as apoptosis (Gulbins et al. [2010]; Szabò et al. [2010]) and proliferation (Bielanska et al. [2009]). In the present work, we investigated the effect of ELF-EMF on $K_v1.3$ expressed in CHO-K1 cells. We focused on whole-cell conductance, which was found to be enhanced in cell subpopulations by relatively low-intensity fields in the order of hundreds of μT.

A. 3 Materials and methods

A. 3.1 Cell culture and $K_v1.3$ channel transfection

CHO-K1 cells (ATCC, USA) were cultured in 35 mm Petri dishes (density: 2×10^3 cells/cm^2) and maintained in F-12 Nutrient Mixture - Ham - supplemented with 10% (v/v) heat-inactivated FBS, 10 μ/ml penicillin and 10 μg/ml streptomycin, in a humidified 5% CO_2 atmosphere and at constant temperature (37 °C). Cells were co-transfected with EGFP and $K_v1.3$ plasmids (2 μg each), kindly provided by Prof. P. Fromherz (Max-Planck Institute for Biochemistry, Martinsried, Germany) (Kupper [1998]). Plasmids were amplified and purified from bacterial strains (HiSpeed Plasmid Maxi Kit, QIAGEN, Italy) and transfected with Lipofectamine^{TM}2000 one to two days after plating. One to two days from transfection, fluorescent cells were pre-selected for electrophysiology (see below). If not otherwise indicated, reagents and culture media were purchased from Life

Technologies (Italy).

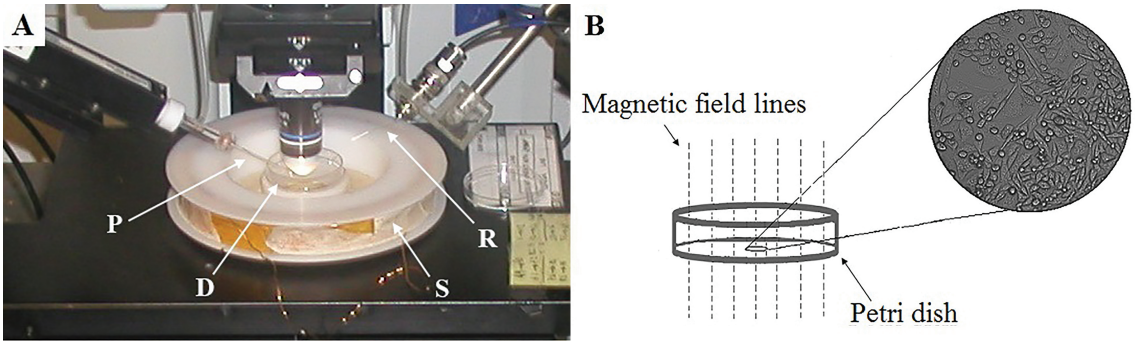

Figure A.1: Experimental setup for ELF-EMF exposure and simultaneous whole-cell patch-clamp. A. Photograph showing the main components of the setup: the solenoid (S) formed by a copper wire wound on a plastic spool is visible at the foreground with the Petri dish (D) at the centre; a patch-clamp pipette (P) is directed to a cell beneath the microscope objective; the Ag/AgCl reference electrode (R) is immersed in the recording solution close to the border of the Petri dish. B: Sketch of the Petri dish and field direction (dashed lines). Blow up: CHO-K1 cells cultured at the bottom of the dish as observed by bright-field microscopy (Olympus BX51WI microscope, water immersion 10x objective, 0.30 N.A., 6.5 mm W. D., from Olympus Italia SRL, Milan, Italy).

A. 3.2 Electrophysiology with ELF-EMF exposure

The electromagnetic field was generated by a 20 Hz sinusoidal current (provided by a function generator Agilent 33220A, Agilent Technologies Inc.) applied to a custom-made solenoid, formed by an enamelled copper wire wound on a plastic support. The cell culture in the Petri dish was placed at the centre of the solenoid and exposed to a magnetic field orthogonal to the plane of adhesion (Figure A.1). Two field intensities were employed:: ELF-EMF$_1$ = 268 μT and ELF-EMF$_2$ = 902 μT (r.m.s. values measured with a Gauss meter Model 907, Magnetic Instrumentations Inc., Indianapolis, IN, USA). While for ELF-EMF$_1$ the function generator was driving directly the solenoid, an amplifier was used to boost the signal to generate ELF-EMF$_2$. The value of 20 Hz was chosen basing on previous

observations (Medlam et al. [2008]; Medlam [2009]; Cecchetto et al. [2013]; Cecchetto et al. [2014]). Experiments were performed at room temperature, with the extracellular recording solution monitored by a digital thermometer (GTH 1150, Greisinger).

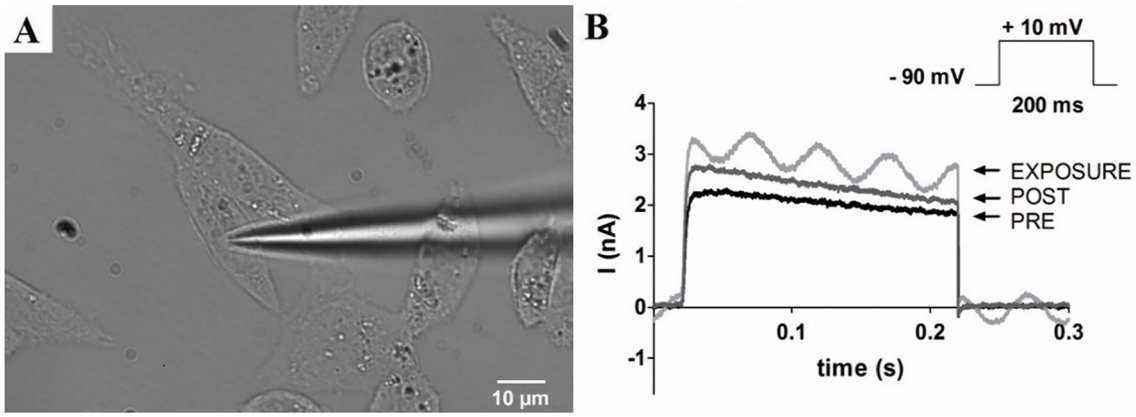

Figure A.2: Effect of ELF-EMF on $K_v1.3$ potassium current. A. Bright-field micrograph of a $K_v1.3$ expressing CHO-K1 cell during an experiment of exposure to the ELF-EMF_2 field. The cell was contacted by a patch-clamp pipette for recording potassium currents that are reported in B. B: Example of three whole-cell current traces recorded, respectively, at 1 min before exposure (PRE), under field exposure at 3 min from the start of field application (EXPOSURE) and 1 min after the field was removed (POST). A potassium current increase of about 50 percent can be clearly observed in the EXPOSURE trace, together with a 20 Hz AC modulation artefact. The increase persists until 1 min post-exposure, although to a reduced extent with respect to the exposure phase. Top-right: voltage-clamp protocol for $K_v1.3$ current activation.

$K_v1.3$ potassium currents were recorded 24-48 h after transfection by patch-clamp in whole-cell voltage-clamp configuration. Recordings were performed before, during and after field exposure using an Axopatch 200B amplifier (Molecular Devices, USA) connected to the PC through a BNC-2110 Shielded Connector Block (National Instruments Corp, Austin, TX, USA) along with a PCI-6259 PCI Card (National Instruments Corp, Austin, TX, USA). WinWCP (Strathclyde Electrophysiology Software, University of Strathclyde, Glasgow, UK) was

used for data acquisition and data analysis. Raw traces were low-pass filtered at 3.3 kHz and sampled at 10 kHz. Micropipettes were pulled from borosilicate glass capillaries (GB150T-10, Science Products GmbH, Hofheim, Germany) using a P-97 Flaming/Brown Micropipette Puller (Sutter Instruments Corp., Novato, CA, USA). The extracellular solution was made of (in mM) 135.0 NaCl, 5.4 KCl, 1.0 $MgCl_2$, 1.8 CaCl, 10.0 glucose, 5.0 HEPES (adjusted to pH 7.4 with 1N NaOH). The intracellular solution was made of (in mM) 140.0 KCl [2.0 $MgCl_2$, 5.0 EGTA, 5.0 HEPES (adjusted to pH 7.3 with 1N KOH). The resistance of the micropipettes in extracellular solution, when filled with intracellular solution, ranged from 2 to 3 MΩ. Current transients due to capacitive (stray, pipette and membrane) components were cancelled through the amplifier compensation circuits, whereas leakage currents were subtracted using a P/4 protocol. The voltage clamp protocol consisted of a depolarizing test pulse of +100 mV amplitude from a −90 mV holding potential for 200 ms, thus obtaining, within the pulse duration, a full $K_v1.3$ activation (Grissmer et al. [1994]; Marom and Levitan [1994]). Depolarizing pulses were applied, with a few exceptions as detailed in the text, at time intervals > 30 s to avoid cumulative inactivation of the channel (Cook and Fadool [2002]; Grissmer et al. [1994]; Marom and Levitan [1994]). The steady-state potassium conductance for activation, g_K, was computed from potassium currents and estimating the potassium reversal potential from intra- and extracellular recording solutions using the Nernst equation. During exposure, a 20 Hz modulation artefact was seen in the electrophysiological trace (see Figure A.2B, exposure trace). Thus, as the artefact was masking the peak potassium current, g_K was estimated from the potassium current averaged across the last full sinusoidal period (50 ms duration) during the test pulse. Similarly, in the absence of the field, currents were averaged across the last 50 ms of the pulse. As such, the measures represented approximations to the $K_v1.3$ steady-state conductance after full channel activation while neglecting an error introduced by slow inactivation (Grissmer et al. [1994]; Marom and Levitan [1994]). Statistical analysis was performed using GraphPad Prism (GraphPad Software Inc., Version 5.01) as detailed in the text.

A. 4 Results and discussion

The effect of ELF-EMF on $K_v1.3$ was investigated by exposing CHO-K1 cells expressing $K_v1.3$ to a field and monitoring changes of the steady-state potassium current by patch-clamp in whole-cell voltage-clamp configuration. Potassium currents were activated throughout the experiment by applying depolarizing test pulses of 200 ms duration to +10 mV and then computing the corresponding steady-state conductance, g_K, as described in section A. 3. Pulses were repeated to record currents prior, during and after cell exposure to ELF-EMF, the field being applied one minute after entering the whole cell configuration, held for 3 min and then removed. $K_v1.3$ currents recorded from one representative cell exposed to the ELF-EMF_2-type field are shown in Figure A.2. Figure A.2A shows one representative cell during the whole-cell patch-clamp procedure. In Figure A.2B three superimposed $K_v1.3$ current traces recorded under exposure of ELF-EMF_2 are reported: the first one recorded 1 min before exposure (labelled as PRE), the second one recorded during exposure, at 3 min from the onset of field application (labelled as EXPOSURE) and the third one after 1 min from the end of exposure (labelled as POST). In those traces, an increase of the $K_v1.3$ steady-state potassium current can be appreciated during the exposure phase. The increase with respect to pre-exposure conditions was nearly 50 percent, which can be recognized despite a 20 Hz sinusoidal modulation artefact obscuring the current trace. Interestingly, such enhancement of the $K_v1.3$ current lasted, in part, even beyond field application. This is exemplified in Figure A.2B, as seen in the trace recorded 1 min after field removal (the POST trace) where the current intensity is still about 10 percent higher than in the pre-exposure phase.

We performed a statistical analysis of the effect of ELF-EMF on $K_v1.3$ focusing on the evolution of the potassium current response over time and on its dependency on the field intensity. Two cell populations were analysed: one exposed to the lower intensity field, ELF-EMF_1, and one to ELF-EMF_2 (see section A. 3). Percentage conductance changes of the steady-state potassium conductance, Δg_K (%), are reported over time for four cells (two exposed to ELF-EMF_1 and two to ELF-EMF_2) in Figure A.3A. Each point in the plots represent the value of Δg_K derived from one single depolarizing test pulse. Note that the time in-

terval between subsequent pulses was chosen to be larger than 30 s in order to avoid cumulative inactivation of the channel (Cook and Fadool [2002]; Grissmer et al. [1994]; Marom and Levitan [1994]) and consequent misjudgements on the effect of the field. Only in one case the inter-pulse interval was of 10 s, that is, at the transition from the end of exposure to the post-exposure period. In fact, an appreciable conductance drop is seen at this first post-exposure checkpoint in three out of four cells (namely cells 1, 3 and 4), which can likely be ascribed to cumulative inactivation.

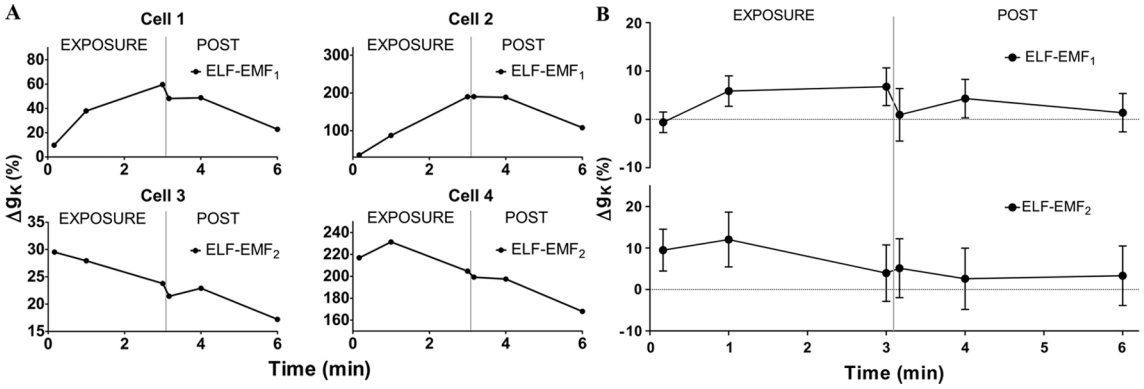

Figure A.3: Average response of $K_v1.3$ steady-state conductance to ELF-EMF_1 and ELF-EMF_2. A: Response of representative cells (cells 1 and 2 exposed to ELF-EMF_1, cells 3 and 4 exposed to ELF-EMF_2) in terms of Δg_K percentage changes with respect to pre-exposure (Δg_K). B: Average Δg_K across the population of cells exposed either to ELF-EMF_1 (N = 92) or to ELF-EMF_2 (N = 44). Data are plotted as mean ± SEM. Only slightly significant increases of conductance were observed in the two populations: at 1 and 3 min of exposure for ELF-EMF_1 ($p = 0.065$ and $p = 0.086$, respectively) and at 10 s and 1 min for ELF-EMF_2 ($p = 0.067$ and $p = 0.074$, respectively). Note the different dynamics of the response to the field in the two cell populations: ELF-EMF_1 exposed cells showed a gradual rise in conductance and then a plateau, while ELF-EMF_2 exposed cells showed an abrupt conductance increase upon field application followed by a gradual decrease after 1 min of exposure.

The plots demonstrate the large variability we encountered across cells both

in terms of dynamics of the response and of its extent. Cells 1 and 2, exposed to the low intensity field, show a gradual increase of Δg_K from the start of exposure, reaching a maximum at the end of field application (3 min from the application onset) and then smoothly decreasing across the following 3 min after field removal. Cells 3 and 4, instead, present an abrupt increase right after field application and then a progressive decrease, which continues during the post exposure period. In terms of the effect's extent, Δg_K varies between 30 to nearly 240 percent across the four cells.

In spite of these representative examples, we observed a significant number of cells that did not clearly respond to the field, and this under both exposures. Thus, when considering averaged responses over the entire cell populations, only a slight tendency to Δg_K increase emerged (Figure A.3B). Interestingly, however, the time course of Δg_K was differing between ELF-EMF$_1$ and ELF-EMF$_2$ treated cells. In the first case, cells were responding with a slow Δg_K increase reaching a steady-state after about 1 min from the exposure onset; in the second case, the conductance increased suddenly upon field application.

A clearer picture of the effect of ELF-EMF$_1$ and ELF-EMF$_2$ on K_v1.3 emerged from the analysis of the population distributions with respect to Δg_K. In particular, we considered the distributions of Δg_K^{max}, the maximum Δg_K observed irrespective of its time of occurrence within the exposure window, for three different cell populations (Figure A.4): (i) one exposed to ELF-EMF$_1$, (ii) one exposed to ELF-EMF$_2$ and one not exposed to the field (control). The control, which was assumed having a normal distribution with respect to Δg_K^{max}, was tested for normality and fitted with a Gaussian curve (least square fit, dark line in Figure A.4). By comparing ELF-EMF$_1$ and ELF-EMF$_2$ distributions with the normally distributed control, we evidenced how cell exposure resulted in a deformation of the distribution due to the higher number of cells showing a Δg_K increase under field exposure (Figure A.4). The effect appeared to be more pronounced for ELF-EMF$_2$ as compared to ELF-EMF$_1$, with the fraction of cells falling beyond 3 σ (σ = standard deviation, SD) at the right side of the control curve accounting for a 26% and 37%, respectively. The distribution of Δg_K^{max} time occurrences observed in these outliers can be summarized as follows: 21% of cells for ELF-EMF$_1$ and 13% for ELF-EMF$_2$ at 10 s from field application; 33% for ELF-EMF$_1$ and 44%

for ELF-EMF$_2$ at 1 min; 46% for ELF-EMF$_1$ and 44% for ELF-EMF$_2$ at 3 min. We also compared the medians of the distributions through a Wilcoxon Signed Rank Test (median equal to zero as null hypothesis) and found that, contrary to the control, medians of ELF-EMF$_1$-exposed and ELF-EMF$_2$-exposed populations differed significantly from zero ($p = 0.014$ and $p = 0.0001$, respectively).

Taken together these results provided a strong indication that ELF-EMF can enhance $K_v1.3$ conductance. The effect, however, is distributed unevenly across cells, which led to asymmetry in the frequency distributions reported in Figure A.4. Increasing field intensity further increases the number of responsive cells. It is noteworthy that the maximum $K_v1.3$ conductance enhancement was usually found at least 1 min from the start of exposure and the effect was lasting beyond field removal. Although it is difficult to argue about molecular mechanisms on this basis, we may infer that the activation of intracellular signalling pathways of $K_v1.3$ modulation could be involved (Cook and Fadool [2002]; Fadool et al. [2000]; Fadool and Levitan [1998]; Bowlby et al. [1997]), thus delaying the onset of the response and justifying its persistence in the absence of the field.

Whatever the mechanism is, our findings suggest that ELF-EMF may produce cellular effects through $K_v1.3$ modulation, particularly at the level of the immune and nervous systems. Starting from these observations, and before considering implications for therapy and prevention, additional studies will be required to elucidate mechanisms and assess whether the effect is found also in native $K_v1.3$-expressing cells, as neurons.

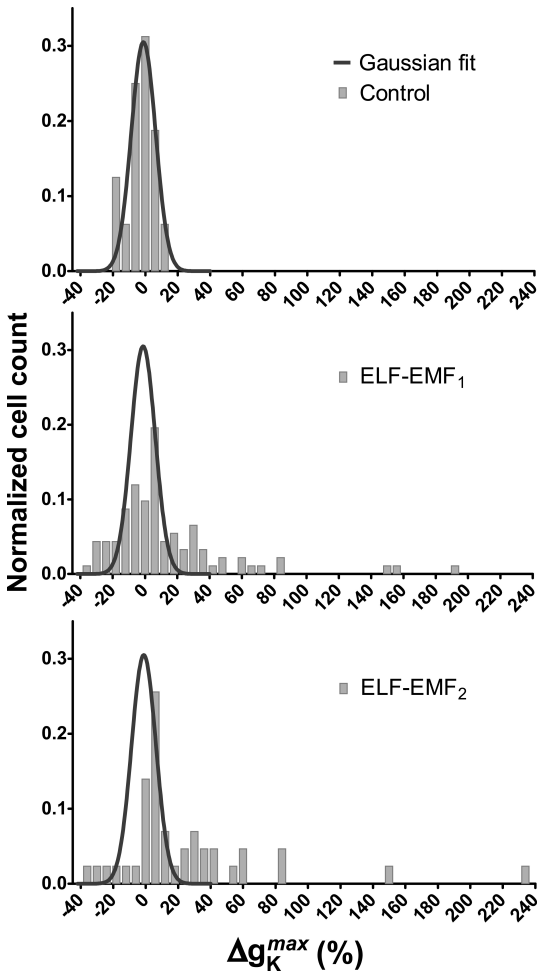

Figure A.4: Distributions of maximum percentage g_K changes. Frequency distributions of Δg_K^{max} in control, ELF-EMF$_1$-exposed and ELF-EMF$_2$-exposed cell populations built with a fixed bin equal to 6% (Control: N = 16; ELF-EMF$_1$: N = 92; ELF-EMF$_2$: N = 44. Total number of cells: N = 156). Raw control data were tested for normality using a D'Agostino & Pearson omnibus K^2 test (p = 0.89; null hypothesis: non-Gaussian distribution) and fitted with a Gaussian curve (least squares fit, R^2=0.937). The same normality test performed on raw data from ELF-EMF$_1$ and ELF-EMF$_2$ cell populations evidenced, in both cases, a significant deviation from normality ($p < 0.0001$ for both).

A. 5 References

Beeton C, Wulff H, Barbaria J, Clot-Faybesse O, Pennington M, Bernard D, Cahalan MD, Chandy KG, Béraud E. 2001. Selective blockade of T lymphocyte K+ channels ameliorates experimental autoimmune encephalomyelitis, a model for multiple sclerosis. Proc. Natl. Acad. Sci. U. S. A. 98:13942-13947.

Bielanska J, Hernández-Losa J, Pérez-Verdaguer M, Moline T, Somoza R, Ramón Y Cajal S, Condom E, Ferreres JC, Felipe A. 2009. Voltage-dependent potassium channels Kv1.3 and Kv1.5 in human cancer. Curr. Cancer Drug Targets 9:904-914.

Bielanska J, Hernández-Losa J, Moline T, Somoza R, Cajal SRY, Condom E, Ferreres JC, Felipe A. 2012a. Increased voltage-dependent K+ channel Kv1.3 and Kv1.5 expression correlates with leiomyosarcoma aggressiveness. Oncol. Lett. 4:227-230.

Bielanska J, Hernández-Losa J, Moline T, Somoza R, Ramón y Cajal S, Condom E, Ferreres JC, Felipe A. 2012b. Differential Expression of Kv1.3 and Kv1.5 Voltage-Dependent K+ Channels in Human Skeletal Muscle Sarcomas. Cancer Invest. 30:203-208.

Bielanska J, Hernández-Losa J, Moline T, Somoza R, Ramón y Cajal S, Condom E, Ferreres JC, Felipe A. 2010. Voltage-dependent Potassium Channels Kv1.3 and Kv1.5 in Human Fetus. Cell. Physiol. Biochem. 26:219-226.

Bowlby MR, Fadool DA, Holmes TC, Levitan IB. 1997. Modulation of the Kv1.3 Potassium Channel by Receptor Tyrosine Kinases. J. Gen. Physiol. 110:601-610.

Cecchetto C, Maschietto M, Boccaccio P, Vassanelli S. 2013. Effect of Low-Frequency and Low-Intensity Magnetic Fields on Potassium Membrane Conductance in CHO-K1 Cells Expressing Kv1.3 Channel. LNL Annu. Rep. 2012 Applied, General & Interdisciplinary Physics:162-163.

Cecchetto C, Maschietto M, Boccaccio P, Vassanelli S. 2014. Increased Potassium Membrane Conductance in Transfected CHO-K1 Cells After Exposure to Low-Frequency and Low-Intensity Magnetic Fields. LNL Annu. Rep. 2013 Applied, General & Interdisciplinary Physics:93-94.

Coetzee WA, Amarillo Y, Chiu J, Chow A, Lau D, McCormack T, Moreno H, Nadal MS, Ozaita A, Pountney D, Saganich M, Vega-Saenz de Miera E, Rudy B. 1999. Molecular diversity of K+ channels. Ann. N. Y. Acad. Sci. 868:233-285.

Cook KK, Fadool DA. 2002. Two Adaptor Proteins Differentially Modulate the Phosphorylation and Biophysics of Kv1.3 Ion Channel by Src Kinase. J. Biol. Chem. 277:13268-13280.

Duque A, Gazula V-R, Kaczmarek LK. 2013. Expression of Kv1.3 potassium channels regulates density of cortical interneurons. Dev. Neurobiol. 73:841-855.

Fadool DA, Tucker K, Phillips JJ, Simmen JA. 2000. Brain Insulin Receptor Causes Activity-Dependent Current Suppression in the Olfactory Bulb Through Multiple Phosphorylation of Kv1.3. J. Neurophysiol. 83:2332-2348.

Fadool DA, Levitan IB. 1998. Modulation of Olfactory Bulb Neuron Potassium Current by Tyrosine Phosphorylation. J. Neurosci. 18:6126-6137.

Funk RHW, Monsees T, Özkucur N. 2009. Electromagnetic effects - From cell biology to medicine. Prog. Histochem. Cytochem. 43:177-264.

Gartzke J, Lange K. 2002. Cellular target of weak magnetic fields: ionic conduction along actin filaments of microvilli. Am. J. Physiol. - Cell Physiol. 283:C1333-C1346.

Gavoçi E, Zironi I, Remondini D, Virelli A, Castellani G, Del Re B, Giorgi G, Aicardi G, Bersani F. 2013. ELF magnetic fields tuned to ion parametric res-

onance conditions do not affect TEA-sensitive voltage-dependent outward K+ currents in a human neural cell line. Bioelectromagnetics 34:579-588.

George Chandy K, Wulff H, Beeton C, Pennington M, Gutman GA, Cahalan MD. 2004. K+ channels as targets for specific immunomodulation. Trends Pharmacol. Sci. 25:280-289.

Gocke AR, Lebson LA, Grishkan IV, Hu L, Nguyen HM, Whartenby KA, Chandy KG, Calabresi PA. 2012. Kv1.3 deletion biases T cells toward an immunoregulatory phenotype and renders mice resistant to autoimmune encephalomyelitis. J. Immunol. Baltim. Md 1950 188:5877-5886.

Grissmer S, Nguyen AN, Aiyar J, Hanson DC, Mather RJ, Gutman GA, Karmilowicz MJ, Auperin DD, Chandy KG. 1994. Pharmacological characterization of five cloned voltage-gated K+ channels, types Kv1.1, 1.2, 1.3, 1.5, and 3.1, stably expressed in mammalian cell lines. Mol. Pharmacol. 45:1227-1234.

Grunnet M, Rasmussen HB, Hay-Schmidt A, Klaerke DA. 2003. The voltage-gated potassium channel subunit, Kv1.3, is expressed in epithelia. Biochim. Biophys. Acta BBA - Biomembr. 1616:85-94.

Gulbins E, Sassi N, Grassmé H, Zoratti M, Szabó I. 2010. Role of Kv1.3 mitochondrial potassium channel in apoptotic signalling in lymphocytes. Biochim. Biophys. Acta BBA - Bioenerg. 1797. 16th European Bioenergetics Conference 2010:1251-1259.

Gutman GA, Chandy KG, Adelman JP, Aiyar J, Bayliss DA, Clapham DE, Covarriubias M, Desir GV, Furuichi K, Ganetzky B, Garcia ML, Grissmer S, Jan LY, Karschin A, Kim D, Kuperschmidt S, Kurachi Y, Lazdunski M, Lesage F, Lester HA, McKinnon D, Nichols CG, O'Kelly I, Robbins J, Robertson GA, Rudy B, Sanguinetti M, Seino S, Stuehmer W, Tamkun MM, Vandenberg CA, Wei A, Wulff H, Wymore RS, International Union of Pharmacology. 2003. International Union of Pharmacology. XLI. Compendium of voltage-gated ion channels: potas-

sium channels. Pharmacol. Rev. 55:583-586.

Hansen LK. 2014. The role of T cell potassium channels, KV1.3 and KCa3.1, in the inflammatory cascade in ulcerative colitis. Dan. Med. J. 61:B4946.

He Y-L, Liu D-D, Fang Y-J, Zhan X-Q, Yao J-J, Mei Y-A. 2013. Exposure to extremely low-frequency electromagnetic fields modulates Na+ currents in rat cerebellar granule cells through increase of AA/PGE2 and EP receptor-mediated cAMP/PKA pathway. PloS One 8:e54376.

Kahlfuß S, Simma N, Mankiewicz J, Bose T, Lowinus T, Klein-Hessling S, Sprengel R, Schraven B, Heine M, Bommhardt U. 2014. Immunosuppression by N-methyl-D-aspartate receptor antagonists is mediated through inhibition of Kv1.3 and KCa3.1 channels in T cells. Mol. Cell. Biol. 34:820-831.

Kupper J. 1998. Functional expression of GFP-tagged Kv1.3 and Kv1.4 channels in HEK 293 cells. Eur. J. Neurosci. 10:3908-3912.

Marom S, Levitan IB. 1994. State-dependent inactivation of the Kv3 potassium channel. Biophys. J. 67:579-589.

Medlam L. 2009. Study of the effect of time-varying magnetic fields on voltage-gated ion channels in neurones. MD Thesis; London: Imperial College.

Medlam L, Maschietto M, Minelli T, Boccaccio P, Moschini G, Vassanelli S. 2008. Increased and Persistent Potassium Conductance in CHO Transfected Cells Following Exposure to Low-Frequency and Low-Intensity Magnetic Field. LNL Annu. Rep. 2008 Applied & Interdisciplinary Physics:78-79.

Pall ML. 2013. Electromagnetic fields act via activation of voltage-gated calcium channels to produce beneficial or adverse effects. J. Cell. Mol. Med. 17:958-965.

Panyi G. 2005. Biophysical and pharmacological aspects of K+ channels in T

lymphocytes. Eur. Biophys. J. 34:515-529.

Swanson R, Marshall J, Smith JS, Williams JB, Boyle MB, Folander K, Luneau CJ, Antanavage J, Oliva C, Buhrow SA, Bennet C, Stein RB, Kaczmarek LK. 1990. Cloning and expression of cDNA and genomic clones encoding three delayed rectifier potassium channels in rat brain. Neuron 4:929-939.

Szabó I, Zoratti M. 2014. Mitochondrial Channels: Ion Fluxes and More. Physiol. Rev. 94:519-608.

Szabó I, Zoratti M, Gulbins E. 2010. Contribution of voltage-gated potassium channels to the regulation of apoptosis. FEBS Lett. 584:2049-2056.

Upadhyay SK, Eckel-Mahan KL, Mirbolooki MR, Tjong I, Griffey SM, Schmunk G, Koehne A, Halbout B, Iadonato S, Pedersen B, Borrelli E, Wang PH, Mukherjee J, Sassone-Corsi P, Chandy KG. 2013. Selective Kv1.3 channel blocker as therapeutic for obesity and insulin resistance. Proc. Natl. Acad. Sci. 110:E2239-E2248.

Veh RW, Lichtinghagen R, Sewing S, Wunder F, Grumbach IM, Pongs O. 1995. Immunohistochemical Localization of Five Members of the Kv1 Channel Subunits: Contrasting Subcellular Locations and Neuron-specific Co-localizations in Rat Brain. Eur. J. Neurosci. 7:2189-2205.

Villalonga N, Martínez-Mármol R, Roura-Ferrer M, David M, Valenzuela C, Soler C, Felipe A. 2008. Cell cycle-dependent expression of Kv1.5 is involved in myoblast proliferation. Biochim. Biophys. Acta BBA - Mol. Cell Res. 1783:728-736.

Wang J, Xiang M. 2013. Targeting Potassium Channels Kv1.3 and K C a 3.1: Routes to Selective Immunomodulators in Autoimmune Disorder Treatment? Pharmacother. J. Hum. Pharmacol. Drug Ther. 33:515-528.

World Health Organization (WHO). 2015. WHO — What are electromagnetic

fields? WHO. http://www.who.int/peh-emf/about/WhatisEMF/en/.

Wulff H, Calabresi PA, Allie R, Yun S, Pennington M, Beeton C, Chandy KG. 2003. The voltage-gated Kv1.3 K+ channel in effector memory T cells as new target for MS. J. Clin. Invest. 111:1703-1713.

Wulff H, Knaus H-G, Pennington M, Chandy KG. 2004. K+ Channel Expression during B Cell Differentiation: Implications for Immunomodulation and Autoimmunity. J. Immunol. 173:776-786.

Xu J, Wang P, Li Y, Li G, Kaczmarek LK, Wu Y, Koni PA, Flavell RA, Desir GV. 2004. The voltage-gated potassium channel Kv1.3 regulates peripheral insulin sensitivity. Proc. Natl. Acad. Sci. 101:3112-3117.

References

Abeles, M. & Goldstein, M. (1977). Multispike train analysis. *Proceedings of the IEEE*, **65**, 762–773. 11

Ahissar, E. (1998). Temporal-code to rate-code conversion by neuronal phase-locked loops. *Neural Comput*, **10**, 597–650. 26

Ahissar, E., Sosnik, R., Bagdasarian, K. & Haidarliu, S. (2001). Temporal frequency of whisker movement. II. Laminar organization of cortical representations. *J. Neurophysiol.*, **86**, 354–367. 8

Ahrens, K.F. & Kleinfeld, D. (2004). Current flow in vibrissa motor cortex can phase-lock with exploratory rhythmic whisking in rat. *J. Neurophysiol.*, **92**, 1700–1707. 52

Alloway, K.D. (2008). Information processing streams in rodent barrel cortex: the differential functions of barrel and septal circuits. *Cereb. Cortex*, **18**, 979–989. 8, 18, 20

Alloway, K.D., Crist, J., Mutic, J.J. & Roy, S.A. (1999). Corticostriatal projections from rat barrel cortex have an anisotropic organization that correlates with vibrissal whisking behavior. *J. Neurosci.*, **19**, 10908–10922. 24

Andres, K.H. (1966). On the microstructure of receptors on sinus hair. *Z Zellforsch Mikrosk Anat*, **75**, 339–365. 29, 30

Arieli, A., Sterkin, A., Grinvald, A. & Aertsen, A. (1996). Dynamics of ongoing activity: explanation of the large variability in evoked cortical responses. *Science*, **273**, 1868–1871. 6, 7

Armstrong-James, M. & Callahan, C.A. (1991). Thalamo-cortical processing of vibrissal information in the rat. II. spatiotemporal convergence in the thalamic ventroposterior medial nucleus (VPm) and its relevance to generation of receptive fields of S1 cortical "barrel" neurones. *J. Comp. Neurol.*, **303**, 211–224. 36

Armstrong-James, M. & Fox, K. (1987). Spatiotemporal convergence and divergence in the rat S1 "barrel" cortex. *J. Comp. Neurol.*, **263**, 265–281. 18, 25, 26

Armstrong-James, M., Fox, K. & Das-Gupta, A. (1992). Flow of excitation within rat barrel cortex on striking a single vibrissa. *J. Neurophysiol.*, **68**, 1345–1358. 4

Arnold, P.B., Li, C.X. & Waters, R.S. (2001). Thalamocortical arbors extend beyond single cortical barrels: an in vivo intracellular tracing study in rat. *Exp Brain Res*, **136**, 152–168. 25

Astrelin, A.V., Sokolov, M.V., Behnisch, T., Reymann, K.G. & Voronin, L.L. (1998). Principal component analysis of minimal excitatory postsynaptic potentials. *J. Neurosci. Methods*, **79**, 169–186. 11

Aunon, J.I., McGillem, C.D. & Childers, D.G. (1981). Signal processing in evoked potential research: averaging and modeling. *Crit Rev Bioeng*, **5**, 323–367. 7

Başar, E., Gönder, A. & Ungan, P. (1976). Important relation between EEG and brain evoked potentials. I. Resonance phenomena in subdural structures of the cat brain. *Biol Cybern*, **25**, 27–40. 8

Başar, E., Rahn, E., Demiralp, T. & Schürmann, M. (1998). Spontaneous EEG theta activity controls frontal visual evoked potential amplitudes. *Electroencephalogr Clin Neurophysiol*, **108**, 101–109. 8

Bak, P., Tang, C. & Wiesenfeld, K. (1987). Self-organized criticality: An explanation of the $1/f$ noise. *Physical Review Letters*, **59**, 381–384. 14, 15

Barth, D.S. & Di, S. (1991). Laminar excitability cycles in neocortex. *J. Neurophysiol.*, **65**, 891–898. 3

Barth, D.S., Di, S. & Baumgartner, C. (1989). Laminar cortical interactions during epileptic spikes studied with principal component analysis and physiological modeling. *Brain Res.*, **484**, 13–35. 3, 5

Beggs, J.M. & Plenz, D. (2003). Neuronal avalanches in neocortical circuits. *Journal of Neuroscience*, **23**, 11167–11177. 15, 16

Black, J.A., Golden, G.T. & Fariello, R.G. (1980). Ketamine activation of experimental corticoreticular epilepsy. *Neurology*, **30**, 315–318. 10

Bourassa, J., Pinault, D. & Deschênes, M. (1995). Corticothalamic projections from the cortical barrel field to the somatosensory thalamus in rats: a single-fibre study using biocytin as an anterograde tracer. *Eur. J. Neurosci.*, **7**, 19–30. 24

Brandt, M.E. & Jansen, B.H. (1991). The relationship between prestimulus-alpha amplitude and visual evoked potential amplitude. *Int. J. Neurosci.*, **61**, 261–268. 8

Brecht, M. & Sakmann, B. (2002). Dynamic representation of whisker deflection by synaptic potentials in spiny stellate and pyramidal cells in the barrels and septa of layer 4 rat somatosensory cortex. *J. Physiol. (Lond.)*, **543**, 49–70. 26

Brody, C.D. (1998). Slow covariations in neuronal resting potentials can lead to artefactually fast cross-correlations in their spike trains. *J. Neurophysiol.*, **80**, 3345–3351. 8

Brown, L.L., Smith, D.M. & Goldbloom, L.M. (1998). Organizing principles of cortical integration in the rat neostriatum: corticostriate map of the body surface is an ordered lattice of curved laminae and radial points. *J. Comp. Neurol.*, **392**, 468–488. 24

Brumberg, J.C., Pinto, D.J. & Simons, D.J. (1996). Spatial gradients and inhibitory summation in the rat whisker barrel system. *J. Neurophysiol.*, **76**, 130–140. 25

Bruno, R.M. & Simons, D.J. (2002). Feedforward mechanisms of excitatory and inhibitory cortical receptive fields. *J. Neurosci.*, **22**, 10966–10975. 27

Bruno, R.M., Khatri, V., Land, P.W. & Simons, D.J. (2003). Thalamocortical angular tuning domains within individual barrels of rat somatosensory cortex. *J. Neurosci.*, **23**, 9565–9574. 27

Buzsáki, G. (1991). The thalamic clock: emergent network properties. *Neuroscience*, **41**, 351–364. 10

Castro-Alamancos, M.A. (2004). Absence of rapid sensory adaptation in neocortex during information processing states. *Neuron*, **41**, 455–464. 8

Cecchetto, C., Mahmud, M. & Vassanelli, S. (2015). Anesthesia effect on single local field potentials variability in rat barrel cortex: Preliminary results. *Conf Proc IEEE Eng Med Biol Soc*, 4721 – 4724. 52

Chakrabarti, S. & Alloway, K.D. (2006). Differential origin of projections from SI barrel cortex to the whisker representations in SII and MI. *J. Comp. Neurol.*, **498**, 624–636. 27

Chapman, R.M. & McCrary, J.W. (1995). EP component identification and measurement by principal components analysis. *Brain Cogn*, **27**, 288–310. 11

Chiaia, N.L., Rhoades, R.W., Bennett-Clarke, C.A., Fish, S.E. & Killackey, H.P. (1991). Thalamic processing of vibrissal information in the rat. I. Afferent input to the medial ventral posterior and posterior nuclei. *J. Comp. Neurol.*, **314**, 201–216. 23

Chialvo, D.R. (2004). Critical brain networks. *Physica A: Statistical Mechanics and its Applications*, **340**, 756–765. 13

Chialvo, D.R. (2010). Emergent complex neural dynamics. *Nature Physics*, **6**, 744–750. 12, 13

Chmielowska, J., Carvell, G.E. & Simons, D.J. (1989). Spatial organization of thalamocortical and corticothalamic projection systems in the rat SmI barrel cortex. *J. Comp. Neurol.*, **285**, 325–338. 20, 24

Coenen, A.M. (1995). Neuronal activities underlying the electroencephalogram and evoked potentials of sleeping and waking: implications for information processing. *Neurosci Biobehav Rev*, **19**, 447–463. 7

Coppola, R., Tabor, R. & Buchsbaum, M.S. (1978). Signal to noise ratio and response variability measurements in single trial evoked potentials. *Electroencephalogr Clin Neurophysiol*, **44**, 214–222. 7

Crandall, J.E., Korde, M. & Caviness, V.S. (1986). Somata of layer V projection neurons in the mouse barrelfield cortex are in preferential register with the sides and septa of the barrels. *Neurosci. Lett.*, **67**, 19–24. 24

Dawson, G.D. (1951). A summation technique for detecting small signals in a large irregular background. *J. Physiol. (Lond.)*, **115**, 2p–3p. 7

Dawson, G.D. (1954). A summation technique for the detection of small evoked potentials. *Electroencephalogr Clin Neurophysiol*, **6**, 65–84. 7

Dehnhardt, G., Hyvärinen, H., Palviainen, A. & Klauer, G. (1999). Structure and innervation of the vibrissal follicle-sinus complex in the Australian water rat, Hydromys chrysogaster. *J. Comp. Neurol.*, **411**, 550–562. 29

Di, S., Baumgartner, C. & Barth, D.S. (1990). Laminar analysis of extracellular field potentials in rat vibrissa/barrel cortex. *J. Neurophysiol.*, **63**, 832–840. 3, 5, 11

Diamond, M.E., Armstrong-James, M., Budway, M.J. & Ebner, F.F. (1992). Somatic sensory responses in the rostral sector of the posterior group (POm) and in the ventral posterior medial nucleus (VPM) of the rat thalamus: dependence on the barrel field cortex. *J. Comp. Neurol.*, **319**, 66–84. 25, 26

Diamond, M.E., von Heimendahl, M., Knutsen, P.M., Kleinfeld, D. & Ahissar, E. (2008). 'where' and 'what' in the whisker sensorimotor system. *Nat Rev Neurosci*, **9**, 601–612. xvii, 22, 23

Dörfl, J. (1985). The innervation of the mystacial region of the white mouse: A topographical study. *J. Anat.*, **142**, 173–184. 29

Ebara, S., Kumamoto, K. & Matsuura, T. (1992). Peptidergic innervation in the sinus hair follicles of several mammalian species. *Kaibogaku Zasshi*, **67**, 623–633. 29

Ebara, S., Kumamoto, K., Matsuura, T., Mazurkiewicz, J.E. & Rice, F.L. (2002). Similarities and differences in the innervation of mystacial vibrissal follicle-sinus complexes in the rat and cat: a confocal microscopic study. *J. Comp. Neurol.*, **449**, 103–119. xvii, 28

Eckerson, W.W. (1995). Three tier client/server architecture: achieving scalability, performance, and efficiency in client server applications. *Open Inf Syst J.*, **10**. 50

Erzurumlu, R.S. & Killackey, H.P. (1980). Diencephalic projections of the subnucleus interpolaris of the brainstem trigeminal complex in the rat. *Neuroscience*, **5**, 1891–1901. 23

Erzurumlu, R.S., Murakami, Y. & Rijli, F.M. (2010). Mapping the face in the somatosensory brainstem. *Nat Rev Neurosci*, **11**, 252–263. xvii, 23

Eversmann, B., Lambacher, A., Gerling, T., Kunze, A., Fromherz, P. & Thewes, R. (2011). A neural tissue interfacing chip for in-vitro applications with 32k recording / stimulation channels on an active area of 2.6 mm^2. 211–214, IEEE. xvii, 44

Fabri, M. & Burton, H. (1991). Ipsilateral cortical connections of primary somatic sensory cortex in rats. *J. Comp. Neurol.*, **311**, 405–424. 24

Famm, K., Litt, B., Tracey, K.J., Boyden, E.S. & Slaoui, M. (2013). Drug discovery: a jump-start for electroceuticals. *Nature*, **496**, 159–161. 81

Feldmeyer, D., Lübke, J. & Sakmann, B. (2006). Efficacy and connectivity of intracolumnar pairs of layer 2/3 pyramidal cells in the barrel cortex of juvenile rats. *J Physiol*, **575**, 583–602. 24

Fox, K. (2008). *Barrel cortex*. Cambridge University Press, Cambridge; New York. xvii, 23

Garabedian, C.E., Jones, S.R., Merzenich, M.M., Dale, A. & Moore, C.I. (2003). Band-pass response properties of rat SI neurons. *J. Neurophysiol.*, **90**, 1379–1391. 8

Gerstein, G.L. (1960). Analysis of Firing Pafferns in Single Neurons. *Science*, **131**, 1811–1812. 7

Gibson, J.M. & Welker, W.I. (1983a). Quantitative studies of stimulus coding in first-order vibrissa afferents of rats. 1. Receptive field properties and threshold distributions. *Somatosens Res*, **1**, 51–67. 30, 31

Gibson, J.M. & Welker, W.I. (1983b). Quantitative studies of stimulus coding in first-order vibrissa afferents of rats. 2. Adaptation and coding of stimulus parameters. *Somatosens Res*, **1**, 95–117. 30, 31

Gireesh, E.D. & Plenz, D. (2008). Neuronal avalanches organize as nested theta- and beta/gamma-oscillations during development of cortical layer 2/3. *Proc. Natl. Acad. Sci. U.S.A.*, **105**, 7576–7581. 16

Gottschaldt, K.M. & Vahle-Hinz, C. (1981). Merkel cell receptors: structure and transducer function. *Science*, **214**, 183–186. 30

Gottschaldt, K.M., Iggo, A. & Young, D.W. (1973). Functional characteristics of mechanoreceptors in sinus hair follicles of the cat. *J. Physiol. (Lond.)*, **235**, 287–315. 30, 31

Guillery, R.W. (1995). Anatomical evidence concerning the role of the thalamus in corticocortical communication: a brief review. *J. Anat.*, **187 (Pt 3)**, 583–592. 25

Halata, Z. & Munger, B.L. (1980). Sensory nerve endings in rhesus monkey sinus hairs. *J. Comp. Neurol.*, **192**, 645–663. 29

Hara, K. & Harris, R.A. (2002). The anesthetic mechanism of urethane: the effects on neurotransmitter-gated ion channels. *Anesth. Analg.*, **94**, 313–318. 9

Hayama, T. & Ogawa, H. (1997). Regional differences of callosal connections in the granular zones of the primary somatosensory cortex in rats. *Brain Res. Bull.*, **43**, 341–347. 25, 27

Higley, M.J. & Contreras, D. (2006). Balanced excitation and inhibition determine spike timing during frequency adaptation. *J. Neurosci.*, **26**, 448–457. 8

Hoeflinger, B.F., Bennett-Clarke, C.A., Chiaia, N.L., Killackey, H.P. & Rhoades, R.W. (1995). Patterning of local intracortical projections within the vibrissae representation of rat primary somatosensory cortex. *J. Comp. Neurol.*, **354**, 551–563. 24

Hoffer, Z.S., Arantes, H.B., Roth, R.L. & Alloway, K.D. (2005). Functional circuits mediating sensorimotor integration: quantitative comparisons of projections from rodent barrel cortex to primary motor cortex, neostriatum, superior colliculus, and the pons. *J. Comp. Neurol.*, **488**, 82–100. 24

Hoogland, P.V., Welker, E. & Van der Loos, H. (1987). Organization of the projections from barrel cortex to thalamus in mice studied with Phaseolus vulgaris-leucoagglutinin and HRP. *Exp Brain Res*, **68**, 73–87. 24

Jacquin & Rhodes (1983). Central projections of the normal and 'regenerate' infraorbital nerve in adult rats subjected to neonatal unilateral infraorbital lesions: a transganglionic horseradish peroxidase study. *Brain Research*, **269**, 137–144. 20

Jones, E.G. & Diamond, I.T. (1995). *Cerebral cortex - The barrel cortex of rodents*, vol. 11. Plenum Press, New York. 4, 18, 20

Kandel, E.R., ed. (2012). *Principles of neural science*. McGraw-Hill, New York, 5th edn. 3, 82

Keller, A. (1995). Synaptic organization of the barrel cortex. In E.G. Jones & I.T. Diamond, eds., *The Barrel Cortex of Rodents*, vol. 11 of *Cerebral Cortex*, 221–262, Springer US. 26

Khatri, V., Hartings, J.A. & Simons, D.J. (2004). Adaptation in thalamic barreloid and cortical barrel neurons to periodic whisker deflections varying in frequency and velocity. *J. Neurophysiol.*, **92**, 3244–3254. 8

Killackey, H.P. (1973). Anatomical evidence for cortical subdivisions based on vertically discrete thalamic projections from the ventral posterior nucleus to cortical barrels in the rat. *Brain Res.*, **51**, 326–331. 24

Killackey, H.P. & Fleming, K. (1985). The role of the principal sensory nucleus in central trigeminal pattern formation. *Brain Res.*, **354**, 141–145. 20

Killackey, H.P. & Leshin, S. (1975). The organization of specific thalamocortical projections to the posteromedial barrel subfield of the rat somatic sensory cortex. *Brain Res.*, **86**, 469–472. 24

Killackey, H.P. & Sherman, S.M. (2003). Corticothalamic projections from the rat primary somatosensory cortex. *J. Neurosci.*, **23**, 7381–7384. 24, 25

Kim, U. & Ebner, F.F. (1999). Barrels and septa: separate circuits in rat barrels field cortex. *J. Comp. Neurol.*, **408**, 489–505. 27

Kisley, M.A. & Gerstein, G.L. (1999). Trial-to-trial variability and state-dependent modulation of auditory-evoked responses in cortex. *J. Neurosci.*, **19**, 10451–10460. 6, 7, 10, 11, 12

Klaus, A., Yu, S. & Plenz, D. (2011). Statistical analyses support power law distributions found in neuronal avalanches. *PLoS ONE*, **6**, e19779. 15

Koralek, K.A., Jensen, K.F. & Killackey, H.P. (1988). Evidence for two complementary patterns of thalamic input to the rat somatosensory cortex. *Brain Res.*, **463**, 346–351. 24

Krupa, D.J., Matell, M.S., Brisben, A.J., Oliveira, L.M. & Nicolelis, M.A. (2001). Behavioral properties of the trigeminal somatosensory system in rats performing whisker-dependent tactile discriminations. *J. Neurosci.*, **21**, 5752–5763. 27

Kublik, E. (2004). Contextual impact on sensory processing at the barrel cortex of awake rat. *Acta neurobiologiae experimentalis*, **64**, 229–238. xvi, 4, 6, 19, 52

Kublik, E., Musiał, P. & Wróbel, A. (2001). Identification of principal components in cortical evoked potentials by brief surface cooling. *Clin Neurophysiol*, **112**, 1720–1725. 11

Kublik, E., Swiejkowski, D.A. & Wróbel, A. (2003). Cortical contribution to sensory volleys recorded at thalamic nuclei of lemniscal and paralemniscal pathways. *Acta Neurobiol Exp (Wars)*, **63**, 377–382. 25

Kwegyir-Afful, E.E., Bruno, R.M., Simons, D.J. & Keller, A. (2005). The role of thalamic inputs in surround receptive fields of barrel neurons. *J. Neurosci.*, **25**, 5926–5934. 25

Kyriazi, H.T., Carvell, G.E., Brumberg, J.C. & Simons, D.J. (1996). Quantitative effects of GABA and bicuculline methiodide on receptive field properties of neurons in real and simulated whisker barrels. *J. Neurophysiol.*, **75**, 547–560. 25

Land, P.W. & Simons, D.J. (1985). Cytochrome oxidase staining in the rat SmI barrel cortex. *J. Comp. Neurol.*, **238**, 225–235. 18

Land, P.W., Buffer, S.A. & Yaskosky, J.D. (1995). Barreloids in adult rat thalamus: three-dimensional architecture and relationship to somatosensory cortical barrels. *J. Comp. Neurol.*, **355**, 573–588. 20, 25

Lavallée, P. & Deschênes, M. (2004). Dendroarchitecture and lateral inhibition in thalamic barreloids. *J. Neurosci.*, **24**, 6098–6105. 25

Leiser, S.C. & Moxon, K.A. (2006). Relationship between physiological response type (RA and SA) and vibrissal receptive field of neurons within the rat trigeminal ganglion. *J. Neurophysiol.*, **95**, 3129–3145. 32, 33, 34

Lindström, S. & Wróbel, A. (1990). Frequency dependent corticofugal excitation of principal cells in the cat's dorsal lateral geniculate nucleus. *Exp Brain Res*, **79**, 313–318. 25

Lombardi, F., Herrmann, H.J., Perrone-Capano, C., Plenz, D. & de Arcangelis, L. (2012). Balance between excitation and inhibition controls the temporal organization of neuronal avalanches. *Phys. Rev. Lett.*, **108**, 228703. 16

Lombardi, F., Herrmann, H.J., Plenz, D. & De Arcangelis, L. (2014). On the temporal organization of neuronal avalanches. *Front Syst Neurosci*, **8**, 204. 16

Loo, S.K. & Halata, Z. (1991). Innervation of hairs in the facial skin of marsupial mammals. *J. Anat.*, **174**, 207–219. 29

Lu, S.M. & Lin, R.C. (1993). Thalamic afferents of the rat barrel cortex: a light- and electron-microscopic study using Phaseolus vulgaris leucoagglutinin as an anterograde tracer. *Somatosens Mot Res*, **10**, 1–16. 24, 25, 27

Ma, P.M. (1991). The barrelettes–architectonic vibrissal representations in the brainstem trigeminal complex of the mouse. i. normal structural organization. *J. Comp. Neurol.*, **309**, 161–199. 20

Ma, P.M. & Woolsey, T.A. (1984). Cytoarchitectonic correlates of the vibrissae in the medullary trigeminal complex of the mouse. *Brain Res.*, **306**, 374–379. 20

Mahmud, M., Girardi, S., Maschietto, M., Rahman, M.M., Bertoldo, A. & Vassanelli, S. (2010). Slow stimulus artifact removal through peak-valley detection of neuronal signals recorded from somatosensory cortex by high resolution brain-chip interface. *World Congress on Medical Physics and Biomedical Engineering, September 7-12, 2009, Munich, Germany*, 2062–2065. 54

Mahmud, M., Pasqualotto, E., Bertoldo, A., Girardi, S., Maschietto, M. & Vassanelli, S. (2011). An automated method for detection of layer activation order in information processing pathway of rat barrel cortex under mechanical whisker stimulation. *J. Neurosci. Methods*, **196**, 141–150. 49, 54

Mahmud, M., Bertoldo, A., Girardi, S., Maschietto, M. & Vassanelli, S. (2012a). SigMate: A matlab-based automated tool for extracellular neuronal signal processing and analysis. *J Neurosci Methods*, **207**, 97 – 112. 50

Mahmud, M., Girardi, S., Maschietto, M. & Vassanelli, S. (2012b). An automated method to remove artifacts induced by microstimulation in local field potentials recorded from rat somatosensory cortex. In *Biosignals and Biorobotics Conference (BRC), 2012 ISSNIP*, 1–4, IEEE. 50

Mahmud, M., Travalin, D., Bertoldo, A., Girardi, S., Maschietto, M. & Vassanelli, S. (2012c). An automated classification method for single sweep local field potentials recorded from rat barrel cortex under mechanical whisker stimulation. *J Med Biol Eng*, **32**, 397–404. 52

Mahmud, M., Cecchetto, C. & Vassanelli, S. (2016). An automated method for characterization of evoked single trial local field potentials recorded from rat barrel cortex under mechanical whisker stimulation. *Cogn Comput*, in–press. 54

Mangun, G.R. & Hillyard, S.A. (1991). Modulations of sensory-evoked brain potentials indicate changes in perceptual processing during visual-spatial priming. *J Exp Psychol Hum Percept Perform*, **17**, 1057–1074. 8

Marotte, L.R., Rice, F.L. & Waite, P.M. (1992). The morphology and innervation of facial vibrissae in the tammar wallaby, Macropus eugenii. *J. Anat.*, **180 (Pt 3)**, 401–417. 29

Massobrio, P., Pasquale, V. & Martinoia, S. (2015). Self-organized criticality in cortical assemblies occurs in concurrent scale-free and small-world networks. *Sci Rep*, **5**, 10578. 15

McCormick, D.A. & Bal, T. (1997). Sleep and arousal: thalamocortical mechanisms. *Annu. Rev. Neurosci.*, **20**, 185–215. 10

Melzer, P., Champney, G.C., Maguire, M.J. & Ebner, F.F. (2006). Rate code and temporal code for frequency of whisker stimulation in rat primary and secondary somatic sensory cortex. *Exp Brain Res*, **172**, 370–386. 26

Mercier, B.E., Legg, C.R. & Glickstein, M. (1990). Basal ganglia and cerebellum receive different somatosensory information in rats. *Proc. Natl. Acad. Sci. U.S.A.*, **87**, 4388–4392. 24

Mihailoff, G.A., Lee, H., Watt, C.B. & Yates, R. (1985). Projections to the basilar pontine nuclei from face sensory and motor regions of the cerebral cortex in the rat. *J. Comp. Neurol.*, **237**, 251–263. 24

Miller, K.D., Pinto, D.J. & Simons, D.J. (2001). Processing in layer 4 of the neocortical circuit: new insights from visual and somatosensory cortex. *Curr. Opin. Neurobiol.*, **11**, 488–497. 25

Millman, D., Mihalas, S., Kirkwood, A. & Niebur, E. (2010). Self-organized criticality occurs in non-conservative neuronal networks during Up states. *Nat Phys*, **6**, 801–805. 14

Mitzdorf, U. (1985). Current source-density method and application in cat cerebral cortex: investigation of evoked potentials and EEG phenomena. *Physiol. Rev.*, **65**, 37–100. 5

Möcks, J., Gasser, T., Pham, D.T. & Köhler, W. (1987). Trial-to-trial variability of single potentials: methodological concepts and results. *Int. J. Neurosci.*, **33**, 25–32. 7

Moore, C.I. (2004). Frequency-dependent processing in the vibrissa sensory system. *J. Neurophysiol.*, **91**, 2390–2399. 28

Mosconi, T.M., Rice, F.L. & Song, M.J. (1993). Sensory innervation in the inner conical body of the vibrissal follicle-sinus complex of the rat. *J. Comp. Neurol.*, **328**, 232–251. 29, 30

Mountcastle, V.B. (1997). The columnar organization of the neocortex. *Brain*, **120 (Pt 4)**, 701–722. 25

Musiał, P., Kublik, E. & Wróbel, A. (1998). Spontaneous variability reveals principal components in cortical evoked potentials. *Neuroreport*, **9**, 2627–2631. 6, 11

Olavarria, J., Van Sluyters, R.C. & Killackey, H.P. (1984). Evidence for the complementary organization of callosal and thalamic connections within rat somatosensory cortex. *Brain Res.*, **291**, 364–368. 25

Pasternak, J.R. & Woolsey, T.A. (1975). The number, size and spatial distribution of neurons in lamina IV of the mouse SmI neocortex. *J. Comp. Neurol.*, **160**, 291–306. 20

Peschanski, M. (1984). Trigeminal afferents to the diencephalon in the rat. *Neuroscience*, **12**, 465–487. 23

Petersen, C.C.H., Grinvald, A. & Sakmann, B. (2003). Spatiotemporal dynamics of sensory responses in layer 2/3 of rat barrel cortex measured in vivo by voltage-sensitive dye imaging combined with whole-cell voltage recordings and neuron reconstructions. *J. Neurosci.*, **23**, 1298–1309. 24

Pierret, T., Lavallée, P. & Deschênes, M. (2000). Parallel streams for the relay of vibrissal information through thalamic barreloids. *J. Neurosci.*, **20**, 7455–7462. 23, 24

Pinto, D.J., Brumberg, J.C. & Simons, D.J. (2000). Circuit dynamics and coding strategies in rodent somatosensory cortex. *J. Neurophysiol.*, **83**, 1158–1166. 36

Pinto, D.J., Hartings, J.A., Brumberg, J.C. & Simons, D.J. (2003). Cortical damping: analysis of thalamocortical response transformations in rodent barrel cortex. *Cereb. Cortex*, **13**, 33–44. 25

Plenz, D. & Thiagarajan, T.C. (2007). The organizing principles of neuronal avalanches: cell assemblies in the cortex? *Trends Neurosci.*, **30**, 101–110. 15

Rhoades, R.W., Belford, G.R. & Killackey, H.P. (1987). Receptive-field properties of rat ventral posterior medial neurons before and after selective kainic acid lesions of the trigeminal brain stem complex. *J. Neurophysiol.*, **57**, 1577–1600. 23

Rice, F.L., Mance, A. & Munger, B.L. (1986). A comparative light microscopic analysis of the sensory innervation of the mystacial pad. I. Innervation of vibrissal follicle-sinus complexes. *J. Comp. Neurol.*, **252**, 154–174. 29, 30, 31

Rieke, F., ed. (1999). *Spikes: exploring the neural code*. Computational neuroscience series, MIT Press, Cambridge, Mass., 1st edn. 35

Rubega, M., Cecchetto, C., Vassanelli, S. & Sparacino, G. (2015). Automated analysis of local field potentials evoked by mechanical whisker stimulation in rat barrel cortex. *Conf Proc IEEE Eng Med Biol Soc*, 1520–1523. 50

Sachdev, R.N.S., Ebner, F.F. & Wilson, C.J. (2004). Effect of subthreshold up and down states on the whisker-evoked response in somatosensory cortex. *J. Neurophysiol.*, **92**, 3511–3521. 6

Schröder, S., Cecchetto, C., Keil, S., Mahmud, M., Brose, E., Dogan, O., Bertotti, G., Wolanski, D., Tillack, B., Schneidewind, J., Gargouri, H., Arens, M., Bruns, J., Szyszka, B., Vassanelli, S. & Thewes, R. (2015). CMOS-compatible purely capacitive interfaces for high-density in-vivo recording from neural tissue. In *Proceedings Biomedical circuits and systems conference (BioCAS2015)*, 1–4, Atlanta, Georgia, USA. xvii, 44

Schubert, D., Kötter, R., Luhmann, H.J. & Staiger, J.F. (2006). Morphology, electrophysiology and functional input connectivity of pyramidal neurons characterizes a genuine layer va in the primary somatosensory cortex. *Cereb. Cortex*, **16**, 223–236. 22

Shepherd, G.M.G. & Svoboda, K. (2005). Laminar and columnar organization of ascending excitatory projections to layer 2/3 pyramidal neurons in rat barrel cortex. *J. Neurosci.*, **25**, 5670–5679. 22

Shepherd, G.M.G., Stepanyants, A., Bureau, I., Chklovskii, D. & Svoboda, K. (2005). Geometric and functional organization of cortical circuits. *Nat. Neurosci.*, **8**, 782–790. 22, 26, 27

Sherman, S.M. & Guillery, R.W. (2002). The role of the thalamus in the flow of information to the cortex. *Philos. Trans. R. Soc. Lond., B, Biol. Sci.*, **357**, 1695–1708. 25

Shimegi, S., Ichikawa, T., Akasaki, T. & Sato, H. (1999). Temporal characteristics of response integration evoked by multiple whisker stimulations in the barrel cortex of rats. *J. Neurosci.*, **19**, 10164–10175. 4

Shoykhet, M., Doherty, D. & Simons, D.J. (2000). Coding of deflection velocity and amplitude by whisker primary afferent neurons: implications for higher level processing. *Somatosens Mot Res*, **17**, 171–180. 34

Shuler, M.G., Krupa, D.J. & Nicolelis, M.A.L. (2002). Integration of bilateral whisker stimuli in rats: role of the whisker barrel cortices. *Cereb. Cortex*, **12**, 86–97. 27

Simons, D.J. (1978). Response properties of vibrissa units in rat SI somatosensory neocortex. *J. Neurophysiol.*, **41**, 798–820. 18, 20, 25

Simons, D.J. (1985). Temporal and spatial integration in the rat SI vibrissa cortex. *J. Neurophysiol.*, **54**, 615–635. 25

Simons, D.J. & Carvell, G.E. (1989). Thalamocortical response transformation in the rat vibrissa/barrel system. *J. Neurophysiol.*, **61**, 311–330. 27

Simons, D.J. & Woolsey, T.A. (1984). Morphology of Golgi-Cox-impregnated barrel neurons in rat SmI cortex. *J. Comp. Neurol.*, **230**, 119–132. 22

Staiger, J.F., Kötter, R., Zilles, K. & Luhmann, H.J. (2000). Laminar characteristics of functional connectivity in rat barrel cortex revealed by stimulation with caged-glutamate. *Neurosci. Res.*, **37**, 49–58. 20

Stephens, R.J., Beebe, I.J. & Poulter, T.C. (1973). Innervation of the vibrissae of the California sea lion, Zalophus californianus. *Anat. Rec.*, **176**, 421–441. 29

Steriade, M. (1997). Synchronized activities of coupled oscillators in the cerebral cortex and thalamus at different levels of vigilance. *Cereb. Cortex*, **7**, 583–604. 10

Steriade, M., Amzica, F., Neckelmann, D. & Timofeev, I. (1998). Spike-wave complexes and fast components of cortically generated seizures. II. Extra- and intracellular patterns. *J. Neurophysiol.*, **80**, 1456–1479. 10

Stüttgen, M.C., Rüter, J. & Schwarz, C. (2006). Two psychophysical channels of whisker deflection in rats align with two neuronal classes of primary afferents. *J. Neurosci.*, **26**, 7933–7941. 34, 35, 38

Swadlow, H.A., Beloozerova, I.N. & Sirota, M.G. (1998). Sharp, local synchrony among putative feed-forward inhibitory interneurons of rabbit somatosensory cortex. *J. Neurophysiol.*, **79**, 567–582. 25

Swanson, L.W. (2003). *Brain maps III: structure of the rat brain: an atlas with printed and electronic templates for data, models, and schematics*. Elsevier, Academic Press, Amsterdam ; Boston, 3rd edn. 38

Temereanca, S. & Simons, D.J. (2004). Functional topography of corticothalamic feedback enhances thalamic spatial response tuning in the somatosensory whisker/barrel system. *Neuron*, **41**, 639–651. 25

Tomen, N., Rotermund, D. & Ernst, U. (2014). Marginally subcritical dynamics explain enhanced stimulus discriminability under attention. *Front Syst Neurosci*, **8**, 151. 13

Truccolo, W.A., Ding, M., Knuth, K.H., Nakamura, R. & Bressler, S.L. (2002). Trial-to-trial variability of cortical evoked responses: implications for the analysis of functional connectivity. *Clin Neurophysiol*, **113**, 206–226. 6, 7

Van Horn, R.N. (1970). Vibrissae structure in the rhesus monkey. *Folia Primatol.*, **13**, 241–285. 29

Veinante, P., Lavallée, P. & Deschênes, M. (2000). Corticothalamic projections from layer 5 of the vibrissal barrel cortex in the rat. *J. Comp. Neurol.*, **424**, 197–204. 23, 24

Welker, C. (1971). Microelectrode delineation of fine grain somatotopic organization of (SmI) cerebral neocortex in albino rat. *Brain Res.*, **26**, 259–275. 18, 20, 25

Welker, C. (1976). Receptive fields of barrels in the somatosensory neocortex of the rat. *J. Comp. Neurol.*, **166**, 173–189. 20, 25

Welker, C. & Woolsey, T.A. (1974). Structure of layer IV in the somatosensory neocortex of the rat: description and comparison with the mouse. *J. Comp. Neurol.*, **158**, 437–453. 20

Welker, E., Hoogland, P.V. & Van der Loos, H. (1988). Organization of feedback and feedforward projections of the barrel cortex: a PHA-L study in the mouse. *Exp Brain Res*, **73**, 411–435. 24

White, E.L. & DeAmicis, R.A. (1977). Afferent and efferent projections of the region in mouse SmL cortex which contains the posteromedial barrel subfield. *J. Comp. Neurol.*, **175**, 455–482. 24

Wilent, W.B. & Contreras, D. (2004). Synaptic responses to whisker deflections in rat barrel cortex as a function of cortical layer and stimulus intensity. *J. Neurosci.*, **24**, 3985–3998. 4

Williams, M.N., Zahm, D.S. & Jacquin, M.F. (1994). Differential foci and synaptic organization of the principal and spinal trigeminal projections to the thalamus in the rat. *Eur. J. Neurosci.*, **6**, 429–453. 23

Wong-Riley, M. (1979). Changes in the visual system of monocularly sutured or enucleated cats demonstrable with cytochrome oxidase histochemistry. *Brain Res*, **171**, 11–28. 58

Woolsey, T.A. & Van der Loos, H. (1970). The structural organization of layer IV in the somatosensory region (SI) of mouse cerebral cortex. The description of a cortical field composed of discrete cytoarchitectonic units. *Brain Res.*, **17**, 205–242. 18, 20

Woolsey, T.A., Welker, C. & Schwartz, R.H. (1975). Comparative anatomical studies of the SmL face cortex with special reference to the occurrence of "barrels" in layer IV. *J. Comp. Neurol.*, **164**, 79–94. 28

Wróbel, A. (1997). Collective electrical activitry of the brain. *Kosmos*, **46**, 317–326. 5

Wróbel, A., Kublik, E. & Musiał, P. (1998). Gating of the sensory activity within barrel cortex of the awake rat. *Exp Brain Res*, **123**, 117–123. 25

Yohro, T. (1977). Structure of the sinus hair follicle in the big-clawed shrew, Sorex unguiculatus. *J. Morphol.*, **153**, 333–353. 29

Yu, S., Yang, H., Shriki, O. & Plenz, D. (2013). Universal organization of resting brain activity at the thermodynamic critical point. *Frontiers in Systems Neuroscience*, **7**. 12

Yuan, B., Morrow, T.J. & Casey, K.L. (1985). Responsiveness of ventrobasal thalamic neurons after suppression of S1 cortex in the anesthetized rat. *J. Neurosci.*, **5**, 2971–2978. 25

Yuan, B., Morrow, T.J. & Casey, K.L. (1986). Corticofugal influences of S1 cortex on ventrobasal thalamic neurons in the awake rat. *J. Neurosci.*, **6**, 3611–3617. 25

Zucker, E. & Welker, W.I. (1969). Coding of somatic sensory input by vibrissae neurons in the rat's trigeminal ganglion. *Brain Res.*, **12**, 138–156. 30